Università degli Studi di Napoli
“Federico II”

Dottorato di ricerca in
Fisica Fondamentale ed Applicata

XXI Ciclo

Measurement of the $K^{\pm} \rightarrow \pi^0 \pi^0 e^{\pm} \nu_e (\overline{\nu_e})$ Branching Ratio with the KLOE detector

Sabino Meola

Coordinator

prof. Lorenzo Marrucci

Supervisors

prof. Marco Napolitano
dott. Fabio Ambrosino

Anno accademico 2007 - 2008

Contents

Introduction **5**

1 The $K^{\pm}$ semileptonic decays **7**
- 1.1 The $K^{\pm} \rightarrow \pi^0\pi^0e^{\pm}\nu_e(\overline{\nu}_e)$ ($K^{00}e4$) decay 11
  - 1.1.1 The K_{l4} decays kinematic 11
  - 1.1.2 $K^{00}e4$ branching ratio: experimental picture 15
  - 1.1.3 $K^{00}e4$ at KLOE 18

2 The experimental apparatus **19**
- 2.1 The collider DAΦNE 19
  - 2.1.1 The DA**Φ**NE luminosity at KLOE 21
- 2.2 The KLOE detector 23
  - 2.2.1 The beam-pipe 23
  - 2.2.2 The drift chamber 26
  - 2.2.3 The electromagnetic calorimeter 32
  - 2.2.4 The quadrupole calorimeters (QCAL) 38
  - 2.2.5 The trigger system 40

3 The Events Classification Procedure **49**
- 3.1 KLOE data taking 49
- 3.2 Data reconstruction 51
  - 3.2.1 Clustering 51
  - 3.2.2 Tracking 52
  - 3.2.3 Vertexing 54
- 3.3 Description of the Event Classification Algorithms 57
  - 3.3.1 The KPM stream selection algorithms 59
- 3.4 Retracking, merging and absolute timing 66

4 The signal selection **73**
- 4.1 $K^{\pm}$ decay vertex reconstruction 74
- 4.2 The 4γ neutral vertex method 75
- 4.3 $\gamma\gamma \rightarrow \pi^0$ association 81
- 4.4 Kinematic fit 83
- 4.5 Track to cluster association 87

4.6 Background rejection 89
4.6.1 Working of the Likelihood Ratio Algorithm 96

5 Branching Ratio measurement **103**
5.1 Introduction 103
5.2 Data sample 104
5.3 The measurement method 104
5.3.1 The choice of the normalization sample 112
5.4 Systematic checks 113
5.5 Efficiency evaluation 117
5.6 Form factor estimation 126

Conclusions **127**

Appendix A **129**

Appendix B **133**

Appendix C **135**

Bibliography **137**

Introduction

This Ph.D. thesis has been done in the framework of the KLOE experiment, which was in operation at DAΦNE, the e^+e^- ϕ-factory of the Laboratori Nazionali di Frascati of the Istituto Nazionale di Fisica Nucleare.
The KLOE experiment has been designed to study neutral and charged kaon decays. Actually, since the ϕ mesons decays 49.2% of the time into a K^+K^- pair, DAΦNE is a very rich source of charged kaons.
Subject of the present work is the measurement of the K_{e4}^{00} ($K^\pm \to \pi^0\pi^0 e^\pm \nu_e(\overline{\nu_e})$) branching ratio, whose most recent measurement dates back to 1988.
The K_{e4}^{00} decay allows to obtain informations on the $\pi - \pi$ scattering at low energies and its branching ratio permits to estimate the form factor value. An accurate measurement of the form factors and of the branching ratios for the $K^{00}e4$ decay can help in checking the validity of the $\Delta I = \frac{1}{2}$ rule and in testing the prediction of different theoretical models. Furthermore it turns out that a very simple relation holds for the decay rate, which is related just to the form factor F and V_{us} , giving a way to test the theorectical prediction on F.
All the previously performed measuremet collected very low statistics of observed signal events and this is reflected in the large relative error on the branching ratio quoted at the present moment, so a new measurement on a high statistics would clarify the experimental scenario and help in testing several theoretical predictions.
We present a new measurement of the K_{e4}^{00} branching ratio normalized to $K_{\pi 3}^{00}$ ($K^\pm \to \pi^\pm\pi^0\pi^0$), given by the partial width ratio

$$\Gamma(K^\pm \to \pi^0\pi^0 e^\pm \nu_e(\overline{\nu}_e))/\Gamma(K^\pm \to \pi^\pm\pi^0\pi^0) \tag{1}$$

The choice of measure a normalized branching ratio allows to keep under control several systematic effects that in the ratio cancel out.

The present thesis has the following structure:

The first chapter is dedicated to a widening of the theoretical motivations to study the semileptonic decays. We intend to outline the general theoretical scheme for the strangeness changing current as well as the important role of the semileptonic decays in describing low energy adron physics.

The KLOE detector and its performance are briefly described in the second chapter.

Chapter three is devoted to the description of the event classification procedures.

The selection of the charged kaons events with two neutral pions in the final state together with the background rejection strategy are described in the fourth chapter.

Finally the method used for the measurement of the K_{e4}^{00} branching ratio is discussed in last chapter.

Chapter 1

The $K^{\pm}$ semileptonic decays

Let us consider the following charged Kaons decays with leptons in the final states:

$$\begin{array}{ll} K^{\pm} \to l^{\pm}\nu_l(\overline{\nu}_l) & (Kl2) \\ K^{\pm} \to \pi^0 l^{\pm}\nu_l(\overline{\nu}_l) & (Kl3) \\ K^{\pm} \to \pi^+\pi^- l^{\pm}\nu_l(\overline{\nu}_l) & (Kl4) \\ K^{\pm} \to \pi^0\pi^0 l^{\pm}\nu_l(\overline{\nu}_l) & (K^{00}l4) \end{array} \tag{1.1}$$

where $l = (e, \mu)$ stands for the charged leptons.
The interaction that gives rise to these decays is the coupling of the us current to the leptonic current $l\nu$.
The us current changes strangness by unity, therefore all the semileptonic Kaon decays listed in (1.1) must be subject to the selection rule $|\Delta S| = 1$.
Decays violating this rule, as the following, have never been observed:

$$\Xi^- \to n l^- \overline{\nu}_l, \quad \Xi^0 \to p l^- \overline{\nu}_l, \quad \Omega^- \to \Lambda^0 l^- \overline{\nu}_l,$$

$$\Omega^- \to \Sigma^0 l^- \overline{\nu}_l, \quad \Omega^- \to n l^- \overline{\nu}_l \qquad (1.2)$$

The theory predicts a further selection rule, $|\Delta S| = |\Delta Q|$. Infact in the $s \to u$ transition the electric charge and strangness of adrons both increase by unity. Again, decays violating this rule, as the following, have never been observed:

$$K^0 \to l^- \overline{\nu}_l \pi^+, \quad \bar{K}^0 \to l^+ \overline{\nu}_l \pi^-, \quad K^+ \to l^- \overline{\nu}_l \pi^+ \pi^+,$$

$$\Sigma^+ \to n l^+ \nu_l \qquad (1.3)$$

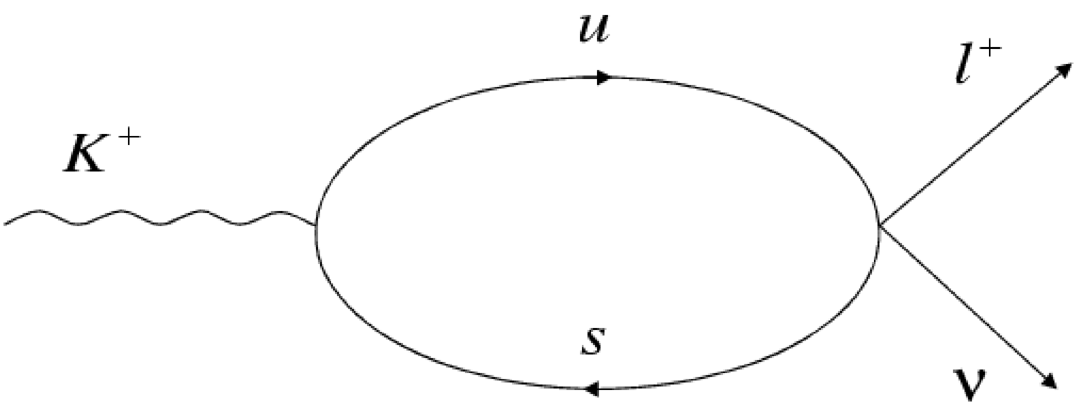

Figure 1.1: Kl2 Feynman diagram.

It has to be underlined, though, that the decays listed in (1.2) and (1.3), with $|\Delta S| > 1$, are forbidden theoretically to an extent much higher than the achieved experimentally accuracy. Indeed, the selection rules are violated only in second and higher order of perturbation theory, so that the anticipated accuracy must be of the order of 10^{14}.

The decay indicated by K_{l2} has a decay amplitude gived by:

$$M = \sqrt{1/2} G f_K p^{\alpha} \bar{u}_{\nu} \gamma_{\alpha} (1 + \gamma_5) u_l V_{us}$$

where p is the Kaon 4-momentum, G is the Fermi costant, $|V_{us}| \sim \sin\theta$ with $\sin\theta$ the Cabibbo angle and f_K the Kaon form factor.
In the approximation of exact SU(3) symmetry, we get:

$$\begin{aligned} m_u = m_d &= m_s \\ m_K &= m_{\pi} \end{aligned}$$

so from the decay width expression:

$$\Gamma(K \rightarrow l\nu) = \frac{G^2}{8\pi} f_K^2 m_K m_l^2 (1 - \frac{m_l^2}{m_K^2}) |V_{us}|^2$$

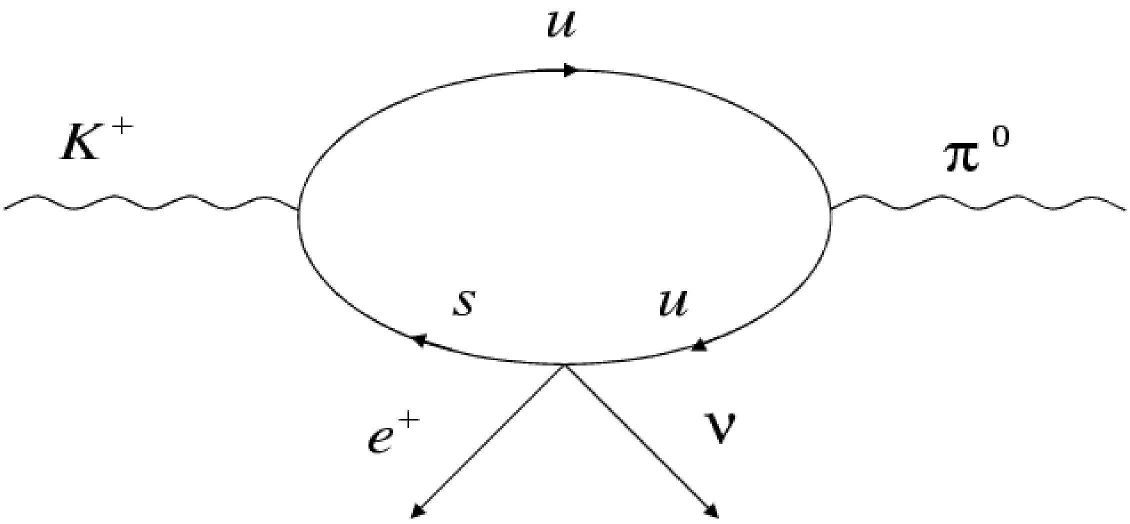

Figure 1.2: K^+e3 Feynman diagram.

Taking into account data on $\Gamma(K^+ \to \mu^+\nu)$ and using $|V_{us}| = 0.21$, we obtain
$f_K/f_\pi = 1.27$.
The exact SU(3) symmetry approximation predicts $f_K = f_\pi$ and the obtained result is in agreement, especially considerig that SU(3) is violated much more strongly in the masses of the Kaon and π meson.

Let us consider the decay:

$$K^+(p_K) \to \pi^0(p_{\pi^0})l^+(p_l)\nu_{l(p_\nu)} \qquad (K^+l3)$$

the S matrix element for such a decay is:

$$S = \frac{G}{\sqrt{2}}V^*_{us}[f_+(q^2)p^\alpha + f_-(q^2)q^\alpha]\ \bar{u}(p_\nu)\gamma_\alpha(1-\gamma_5)v(p_l)$$

where $q = p_K - p_{\pi^0}$, $p = p_K + p_{\pi^0}$ is the 4-momentum carried by leptons and G is the Fermi costant.
The terms $f_-(q^2)$ and $f_+(q^2)$ are the form factors, which are functions of the transferred 4-momentum square. We assume a linear dependence between the form factors and q^2 [2]:

$$f_{\pm}(q^2) = f_{\pm}(0)\ [1 + \lambda_{\pm} \frac{q^2}{m^2_{\pi^0}}] \tag{1.4}$$

where $m^2_{\pi^0}$ is the neutral pion mass square and $\lambda^{\pm}$ a proportionality factor.
The decay width $\Gamma(K^+e3)$ is given by[2]:

$$\Gamma(K^+e3) = \frac{G^2 m_K^5}{384\pi^3} |V_{us}|^2 |f_+(q^2)|^2$$

taking into account that the branching ratio for a given decay channel $A \rightarrow B_1 ... B_n$ is equal to the ratio:

$$BR(A \rightarrow B_1 ... B_n) = \frac{\Gamma(A \rightarrow B_1 ... B_n)}{\Gamma_{Tot}}$$

with $\Gamma_{Tot} = \frac{1}{\tau}$ total decay width, we obtain:

$$|V_{us}|^2 = \frac{BR((K^+e3)}{\tau(K^+)} \frac{384\pi^3}{G^2 m_K^5 |f_+(q^2)|^2} \tag{1.5}$$

The K_{l4} decays allow to study the $\pi - \pi$ scattering at low energies.
The decay width for such a processes is:

$$M = \sqrt{1/2}\ G(V_\alpha + A_\alpha) L^\alpha \sin\theta$$

where

$$A = f_1(p_1 + p_2)_\alpha + f_2(p_1 - p_2)_\alpha + f_3(p - p_1 - p_2)_\alpha$$

$$\mathrm{V}_\alpha = f_4 m_K^{-2}\ \epsilon_{\alpha\mu\nu\rho}\ p_\mu p_{1\nu} p_{2\rho}$$

with p_1, p_1 and p representing the π^-, π^+ and K mesons momenta respectively. The f_1, f_2, f_3, f_4 form factors are functions of three scalar variables, pp_1, pp_2, p_1p_2.

The f_3 term contribution is negligible because of the smallness of the electron mass. The contribution of the f_4 term is also small owing to high powers of momentum.
An estimante that can be obtained for the form factors f_1 e f_2 is [2]:

$$f_1 \approx f_2 \approx 1/f_\pi$$

1.1 The $K^{\pm} \to \pi^0\pi^0 e^{\pm}\nu_e(\overline{\nu}_e)$ ($K^{00}e4$) decay

The main theoretical interest in the study of K meson decays into two pions and a lepton pair is given by the possibility to extract information on the low-energy $\pi\pi$ interaction.

One relevant advantage shown by $K^{00}e4$ decay is that only couplings to an external left-handed vector leptonic current are involved. Moreover, since the two pions can only be emitted in $l = 0, 1$ relative angular momentum states, and assuming the validity of the semileptonic $\Delta I = \frac{1}{2}$ rule, the only possible quantum states allowed for the dipion system are $l = 0$, $I = 0$ e $l = 1$, $I = 1$ [3].
This implies that the $K^{00}e4$ decays can be used to extract the $\pi\pi$ scattering phase-shift difference $(\delta_0^0 - \delta_1^1)$ as a function of the dipion invariant mass.

Furthermore, an accurate measurement of the form factors and of the branching ratios for the $K^{00}e4$ decay can help in checking the validity of the $\Delta I = \frac{1}{2}$ rule and in testing the prediction of different theoretical models.

1.1.1 The K_{l4} decays kinematic

To completely describe the kinematics of the decay under study, it is necessary to define five kinematical independent variables [4].
Let us consider three reference frame: the K rest frame (Σ_K), the two π center of mass frame ($\Sigma_{\pi\pi}$) and the leptonic couple center of mass frame (Σ_l), see figure (1.3).

We refer to p_K as the Kaon 4-momentum, to p_1 and p_2 as two pion 4-momenta and to p_l and p_ν as the electron and neutrino 4-momentum respectively. Now let us define the following variables (see figure (1.3)):

- $s_\pi = (p_1 + p_2)^2$; dipion invariant mass square.
- $s_l = (p_l + p_\nu)^2$; dilepton invariant mass square.
- θ_π; angle of the "first" pion in $\Sigma_{\pi\pi}$ with respect to the direction of flight of the dipion system in Σ_K.
- θ_l; angle of the charged lepton in $\Sigma_{l\nu}$ with respect to the direction of flight of the dilepton system in Σ_K.
- ϕ; angle between the planes formed by the dipion and the dilepton system in Σ_K.

In other terms, the kinematic approach of these decays analyzes the products as if they came out from two "resonances", the dipion and the dilepton having mass $\sqrt{s_\pi}$ and $\sqrt{s_l}$ respectively.
Let us introduce the following 4-momenta:

$$P \equiv p_1 + p_2 \;, L \equiv p_l + p_\nu \;, Q \equiv p_1 - p_2$$

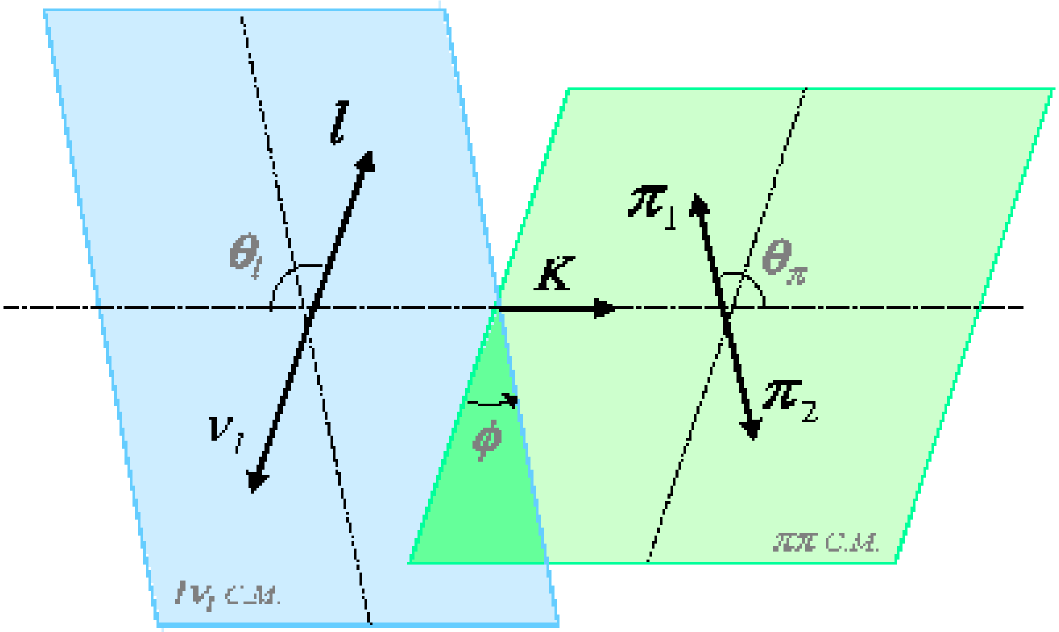

Figure 1.3: The $K^{00}e4$ decay kinematic. The angles ϕ, θ_π and θ_l are evaluated in the Σ_K, $\Sigma_{\pi\pi}$ and $\Sigma_{l\nu}$ reference frame respectively.

and express the matrix elements of the adronic axial-vector and vector currents in the general form:

$$\langle\pi\pi|J^A_\lambda|K\rangle = \frac{F}{m_K}P_\lambda + \frac{G}{m_K}Q_\lambda + \frac{R}{m_K}L_\lambda$$
$$\langle\pi\pi|J^V_\lambda|K\rangle = \frac{iH}{m_K^3}\epsilon_{\lambda\mu\nu\sigma}L^\mu P^\nu Q^\sigma$$

where the form factors F, G, H and R are dimensionless real analytic functions of p_1p_2, p_Kp_1 and p_Kp_2 or, equivalently, of s_π, s_l and θ_π.
Since the Kaon's and the pion's states have the opposite relative intrinsic parities, the matrix element of the axial-vector current transforms as an ordinary vector, while $\langle\pi\pi|J^V_\lambda|K\rangle$ transforms as an axial vector.
After the integration over all the variables on which the form factors don't depend, the partial decay rate for the $Kl4$ can be written as:

$$d\Gamma = G_F^2|V_{us}|^2N(s_\pi,s_l)J_5(s_\pi,s_l,\theta_\pi,\theta_l,\phi)ds_\pi ds_l d(\cos\theta_\pi)d(\cos\theta_l)d\phi \qquad (1.6)$$

where J_5 is expressed in terms of simple functions of θ_l and ϕ multiplying nine functions $I_i(s_\pi,s_l,\theta_\pi,F,G,H,R)$ [5], and the kinematic factor$N(s_\pi,s_l)$ is defined as

$$N(s_\pi, s_l) = \frac{1 - m_l^2/s_l}{2^{14}\pi^6 m_K^5}\sqrt{(1 - 4\frac{m_\pi^2}{s_\pi})[(m_K^2 - s_\pi - s_l)^2 - 4s_\pi s_l]}$$

By integrating over θ_π and θ_l, the partial decay rate (1.6) becomes:

$$d\Gamma = G_F^2|V_{us}|^2 N(s_\pi, s_l) J_3(s_\pi, s_l, \theta_\pi) ds_\pi ds_l d(\cos\theta_\pi)$$

J_3 being defined as

$$J_3(s_\pi, s_l, \theta_\pi) = \tfrac{4\pi}{3}(1-z)\{(2+z)[|F_1|^2 + (|F_2|^2 + |F_3|^2)\sin^2\theta_\pi] + 3z|F_4|^2\}$$

with

$\mathrm{z} = \mathrm{m}_l^2/s_l$
$\mathrm{F}_1 = \sqrt{(P\cdot L)^2 - s_\pi s_l}\cdot F - \sqrt{1 - 4m_\pi^2/s_\pi}(P\cdot L)\cos\theta_\pi \cdot G$
$\mathrm{F}_2 = \sqrt{s_l(s_\pi - 4m_\pi^2)}$
$\mathrm{F}_3 = \sqrt{s_l(s_\pi - 4m_\pi^2)[(P\cdot L)^2 - s_\pi s_l]}\cdot H/m_K^2$
$\mathrm{F}_4 = (P\cdot L)F - \sqrt{(1 - 4m_\pi^2/s_\pi)[(P\cdot L)^2 - s_\pi s_l]}\cos\theta_\pi \cdot G - s_l R$

By exploiting the isospin symmetry connecting the current matrix elements after the decomposition of symmetric and antisymmetric parts under the exchange $p_1 \leftrightarrow p_2$ for all the $Kl4$ channels, the following isospin relation can be obtained for the decay rates:

$$\Gamma(K^{\pm}l4) = 2\Gamma(K^{00}l4) + \frac{1}{2}\Gamma(K^0 l4) \tag{1.7}$$

where the $\Delta I = 1/2$ rule has been assumed.

Another result from the $\Delta I = 1/2$ rule, predicts that the form factor F has to be equal for $K^{\pm}l4$ and $K^{00}l4$ decays.
The form factors F, G, H and R can be expressed as partial wave expansions in the variable θ_π, with amplitudes (f_l, g_l, h_l e r_l) which are real functions of s_π and s_l and phases which are assumed to be the phase shifts δ_l^I involved in the elastic $\pi\pi$ scattering (Even if the phase shifts depend on the dipion invariant mass s_π, δ_l^I are considered as constant, *i.e.* as if they were averaged over all the s_π spectrum).

An important test regards the validity of the assumption of locality of the lepton pairs coupling to hadrons, which implies that the dependence of the spectrum on the single quantities θ_l and θ_π follows the expression (after that the integration over the other four variables has been performed):

$$\frac{d\Gamma}{d\cos\theta_l} = a + b\cos\theta_l + c\cos 2\theta_l$$

$$\frac{d\Gamma}{d\phi} = \alpha + \beta\cos\phi + \gamma\sin\phi + \delta\cos 2\phi + \epsilon\sin 2\phi$$

If is this the case, then the intensity distribution functions $\langle I_i \rangle$ can be used as free parameters to fit the event distribution in the (θ_l,ϕ) plane and to extract the phase shift difference $(\delta_0^0 - \delta_1^1)$ for each s_π bin from the relations:

$$tan(\delta_0^0 - \delta_1^1) = \frac{1}{2}\frac{\langle I_7 \rangle}{\langle I_4 \rangle}$$

$$tan(\delta_0^0 - \delta_1^1) = 2\frac{\langle I_8 \rangle}{\langle I_5 \rangle}$$

Another test concerns the hypothesis that the pions pairs are produced uniquely in $l = 0$ and $l = 1$, which is more reasonalble for low values of s_π. Then the form factors G and H are seen to be independent from θ_π, while both F and R are at most linear in $\cos\theta_\pi$. Therefore the intensity spectrum in the variable θ_π, integrating over all the other four variables, behave according to the expression:

$$\frac{d\Gamma}{d\cos\theta_\pi} = A + B\cos\theta_\pi + C\cos 2\theta_\pi$$

Finally, the isoscalar S-wave scattering length a_0^0 can be extracted by making use of a model based solutions to the Roy equations [6], which has to be compared with the χPT prediction $a_0^0 = 0.20 \pm 0.01$ [7].

It is important to point out that what has been discussed so far applies to both K_{e4} and $K\mu4$ decays.

In the case of K_{e4} decays, the mass of the charged lepton can be neglected and z can be set to 0. This approximation makes useless any study on polarization effects since the electron is supposed to be polarized longitudinally only, a simpler shape for the integrated intensity J_3 is obtained, and the form factor R can be put to 0.

In the K_{l4}^{00} channel, one can assume that the form factors do not depend on θ_π, this implies that G and H vanish by Bose statistics (as the two pions in the final state are identical). For this reason only F and R play a role in the decay rate $\Gamma(K^{00}l4)$, which can be simply expressed as:

$$2\Gamma(K^{00}l4) = |V_{us}|^2 \cdot (C_F|F|^2 + C_R|R|^2 + C_{FR})|F||R|) \tag{1.8}$$

where the coefficients C_F, C_R and C_{FR} are calculated theoretically[12].
It turns out that, due to small mass of the electron, in the $K^{\pm} \to \pi^0\pi^0 e^{\pm}\nu_e(\overline{\nu}_e)$ decay F is the only relevant form factor, describing the strong interactions for the axial-vector current and that a very simple relation holds for the decay rate:

$$\boxed{\Gamma((K^{00}l4)) = 0.8 \cdot |V_{us}|^2|F|^2 \cdot 10^3 sec^{-1}} \tag{1.9}$$

where the value $C_F = 1.59 \cdot 10^3\ s^{-1}$ for the K_{e4} decay has been used [12].

1.1.2 $K^{00}e4$ branching ratio: experimental picture

In table (1.1) the K_{l4} branching ratio measurements as reported by the Particle Data Group (2006) are listed.
The $K^{00}e4$ branching ratio shown is obtained by fitting three independent experimental results. The large relative error ($\sim 20\%$) associated to $\Gamma_{K^{00}e4}/\Gamma_{Total}$ is due to the low statistics reached so far by experiments in this channel. The isospin relation (1.7) connecting the first three decay modes listed in table is verified within the errors.

The first experimental analysis on the $K^{00}e4$ decay dates back to 1971. F. Romano and coll. [8] used a large amount of semileptonic decays from the X2 experiment at CERN to measure the relative branching ratio $\Gamma(K^+ \to \pi^0 e^+\nu_e\gamma)/\Gamma(K^+ \to \pi^0 e^+\nu_e)$. As no evidence of events compatible with the $K^{00}e4$ kinematics was found, an upper limit at the 90 % confidence level was estabilished for the absolute branching ratio: $BR(K^{00+}e4) < 1.8 \cdot 10^{-4}$.

In 1973 D. Ljung and D. Cline [9] studied $K^+ \to \pi^0\pi^0 e^+\nu_e$ among some rare K^+ decays modes. The analyzed data set was collected over a period of three years at Argonne National Laboratory, using K^+ mesons of $\sim 500\, MeV/c$ at the Zero Gradient Synchroton (ZGS) entering a bubble chamber filled with heavy freon in a $46\, kG$

Decay channel (i)	$\frac{\Gamma_i}{\Gamma_{Total}}(\cdot 10^{-5})$
$K^+ \to \pi^+\pi^- e^+\nu_e$	3.91 ± 0.17
$K^+ \to \pi^0\pi^0 e^+\nu_e$	2.1 ± 0.4
$K^0_L \to \pi^0\pi^{\pm} e^{\mp}\overline{\nu}_e(\nu_e)$	5.18 ± 0.29
$K^+ \to \pi^+\pi^- \mu^+\nu_\mu$	1.4 ± 0.9

Table 1.1: K_{l4} BR experimental measurements, as quoted by PDG (2006).

magnetic field. The scanning of 674200 stopped K^+ decays produced the selection of 148 candidates for the $K^{00}e4$ mode, in which an electron track and 4 converted γ's pointing at the decay vertex were observed.

Then, by applying a cut on the χ^2 probability of a three-constraint fit and on the event topology to reject background, the sample was reduced to 9 events. In the last step only 2 decays were selected, as a low χ^2 fit was obtained in the $K^+ \to \pi^0\pi^0\pi^+$ hypothesis for the other seven decays.

The final result $BR = (1.8^{+2.4}_{0.6})\dot{1}0^{-5}$ was obtained from the ratio with 22952 K^+_{e3} decays found in the same initial sample, which yielded $\Gamma(K^+ \to \pi^0 e^+ \nu_e \gamma)/\Gamma(K^+ \to \pi^0 e^+ \nu_e) = 3.8 \cdot 10^{-4}$.

The work of Bolotov e coll. [10] studied two rare K^- radiative decay modes: K^-_{e3} and $K^{00-}e4$. The experimental measurement was held with the ISTRA apparatus on $25\,GeV$ energy beam of π and K mesons from the IHEP accelerator. Both these two analyses were performed after calibration process based on the identification of about 170000 K^-_{e3} decays.
The selection of $K^{00}e4$ events was carried out through two stages.

As a first requirement, 5 or 6 showers had to be found in the spectometer and the distances between their centers had to be at least 10 cm.

Subsequently, a 99% C. L. cut was applied on a six-costraint χ^2 fit under the $K^{\pm} \to \pi^0\pi^0\pi^{\pm}$ ($K^{00}\pi3$) hypothesis, which had to reject the main contribution to backgroud: $K^{00-}\pi3$ decays in which the π^- emits a δ electron, or decays into $e^-\overline{\nu_e}$, or follows the chain $\pi \to \mu\nu$ $\mu \to \nu\overline{\nu}$. Also charge exchange and other processes were considered as sources of contamination.

The surviving candidates were then analyzed by a four-constraint fit under the $K \to \pi^0\pi^0 e\nu$ ($K^{00}e4$) hypothesis and a 99% C. L. cut was designed to definetively select $K^{00-}e4$ decays. The estimate amount of background was made by measuring the different counting efficiencies for pions and electrons. From 25 events resulting after the background subtraction it was possible to produce the final result $BR(K^{00-}e4) = (2.0^{+0.5}_{-0.4}) \cdot 10^{-5}$ from the $\Gamma(K^- \to \pi^0\pi^0 e^-\overline{\nu_e})/\Gamma(K^- \to \pi^0 e^-\overline{\nu_e})$ ratio.

Two years later, Barmin and coll. [11] performed an absolute branching ratio measurement on a small amount of positive $K^{00}e4$ decays. The work was done with photographs obtained in a xenon bubble chamber exposed to a $\sim 0.85GeV/c$ K^+ meson beam extracted from the proton synchroton of ITEP. The total statistics included $\sim 6 \cdot 10^9$ K^+ observed in the acceptance region of the chamber. Both K^+ decays in flight and at rest were used, defining two separate groups of events, which were called primary and secondary, respectively.

The topology for $K^{00}e4$ events consisted in a track connected to the K^+ and accompanied by an electromagnetic shower and other four showers pointing to the supposed kaon vertex. The main background source came from the $K^+ \to \pi^0\pi^0\pi^+$ decay with the π^+ misidentified as a e^+. A Monte Carlo method was used to improve the purity of the sample and the total depth of the positron shower was the most powerful feature for rejecting the $K^{00}\pi3$ background.

A ∼ 20% background was estimated in the secondary decays, among which 4.9 ± 2.7 events were counted as signal, while the 5 events observed in the primary decays were considered as uncontaminated and affected by poissonian uncertainty only. After the correction due to the variuos efficiencies (scannig, checking, final identification, etc.) the combinations of the results from the two sets of data samples gave the final measurement: $BR(K^{00+}e4) = (2.54\pm0.89)\cdot10^{-5}$, in agreement with the previous experimental results.

Form factors estimation

The relation (1.9) allows to estimate the form factor modulus F in a simple way using $K^{00}e4$ decay measured parameters.
Despite the very low statistics collected, it is possible to estimate F for all the experiment described so far.
Some published papers on $K^{00}e4$ decay express F in a different notation by means of the parameter f_1, this can be transcribed according to the convention on the form factor used in this work: $F \equiv f_1/V_{us}$.

In table (1.2) BR($K^{00}e4$) measurement and correspondig form factor F estimation are reported. Both the theoretically and experimentally uncertainties on $|V_{us}|$ are negligible with respect to the precision reached [13], so that the value $|V_{us}| \approx 0.22$ has been used.

	$\|F\|$	$\Gamma_i/\Gamma_{Total}(\cdot10^{-5})$	Normalization	Events
Romano [8] (1971)	-	< 18	K^+e3	0
Ljung [9] (1973)	$4.4^{+2.2}_{-0.9}$	$1.8^{+2.4}_{-0.6}$	K^+e3	2
Bolotov [10] (1986)	$6.4^{+0.8}_{-0.6}$	$2.0^{+0.5}_{-0.4}$	K^-e3	25
Barmin [11] (1988)	7.3 ± 1.3	2.54 ± 0.89	$K^+ \to all$	10

Table 1.2: In table are reported the measured value for BR($K^{00}e4$), as the form factor modulus F, the normalization and the number of collected events. For the form factor F estimation, the value $|V_{us}| \approx 0.22$ is considered, both the theoretically and experimentally uncertainties on $|V_{us}|$ are negligible with respect to the precision reached for F.

A possible parametrization for the form factor F in the $K^{00}e4$ channel is the following:

$$F = F_0(1+\lambda q^2)e^{i\delta_0^0} \tag{1.10}$$

with $q^2 = (s_\pi - 4m_\pi^2)$ and $\lambda = 0.08$ [16].
The resulting value of the amplitude, $F_0 = 5.72^{+0.57}_{-0.49}$ [17], agrees very well with the

analogous measurement performed by Rosselet and coll. [14] at the Geneva-Saclay experiment on a sizieable sample of 30000 $K^{+}e4$ decays ($F_0 = 5.59 \pm 0.14$), so confirming the isospin prediction on the equality of F in $K^{+}e4$ and $K^{'}l4$.

Another measurement has been performed in 2003 by E865 [15] at the Brookhaven Alternate Gradient Synchroton (AGS) on a large statistics of 400000 K^{+}_{e4} events: according to the parametrization (1.10) the values $F_0 = 5.83 \pm 0.08$ and $\lambda = 0.079 \pm 0.015$ have been measured.

It has to be underlined that a new measurement on higher statistics would allows to improve the form factor knowledge.

1.1.3 $K^{00}e4$ at KLOE

In virtue of the ~ 2 fb^{-1} integrated luminosity collected, KLOE represents a very good opportunity for a new $K^{00}e4$ BR measurement.
Infact from the ϕ cross section ($\sim 3.2 \cdot 10^{6}$ pb), $\phi \to K^{+}K^{-}$ ($\sim$ 49 %) BR and $K^{00}e4$ BR ($\sim$ $2.41 \cdot 10^{-5}$), it is possible to extract the signal number of events expected on the whole statistics:

$$N_{K' e4} = 2000 \cdot (3.2 \cdot 10^{6} \cdot 0.49 \cdot 2 \cdot 2.41 \cdot 10^{-5}) \sim 154200$$

obtaining $N_{K^{00}e4} \sim$ 154200.
Taking into account that about 40 % of the charged Kaons do not reach the drift chamber, we get $\sim$ 92500 events.
As shown in the previous section, all the $K^{00}e4$ BR measurement has been performed, until now, on very low statistics producing a big final error ($\sim 20\%$).
Furthermore, the K_{l4} decays analysis represent an excellent tool to investigate the S-wave $\pi\pi$ scattering, allowing to get information on the form factor F and then verify theoretical prediction on the $K^{+}e4$ and $K^{00}e4$ form factors.

Chapter 2

The experimental apparatus

2.1 The collider DAΦNE

The collider DAΦNE (**D**ouble **A**nnular Φ-factory for **N**ice **E**xperiments) has been designed for the study of the CP violation in the neutral kaon system. It is an electron-positron collider tuned to work with a center of mass energy around the ϕ mass, $M_\phi = 1019.456 \pm 0.020\ MeV$ [57]. The ϕ production cross section reaches a peak value of $\sigma_{e^+e^- \to \phi} \sim 3.2\ \mu b$, with a width of $\Gamma_\phi = 4.26 \pm 0.05\ MeV$ [57]. The branching ratios of the main decays of the ϕ are reported in table 2.1.
The collider consists of a LINAC, an accumulation ring and two collision rings (see figure 2.1). Electron and positron beams, each having energy of about 510 $MeV \simeq M_\phi/2$, circulate in two different rings, shifted in the horizontal plane, in order to reduce inter-beam interactions. There are two interaction regions, one of those is occupied by the KLOE detector. The beams collide at the Interaction Point (IP) with a crossing angle $\theta_x \simeq 25\ mrad$, then the ϕ is produced with a momentum along the z axis of about 13 MeV. The beams collide with a frequency up to 370 MHz, corresponding to a bunch crossing period of $T_{bunch} = 2.7\ ns$ and a maximum number of bunches circulating of 120. Some of the DAΦNE project's parameter are reported in table 2.2. In table 2.3 some parameters of the 2002 data taking are reported.

Decay channels	BR
K^+K^-	$(49.2 \pm 0.7) \times 10^{-2}$
$K^0_L K^0_S$	$(33.8 \pm 0.6) \times 10^{-2}$
$\rho\pi + \pi^+\pi^-\pi^0$	$(15.5 \pm 0.6) \times 10^{-2}$
$\eta\gamma$	$(1.297 \pm 0.033) \times 10^{-2}$
$\pi^0\gamma$	$(1.26 \pm 0.10) \times 10^{-3}$
e^+e^-	$(2.91 \pm 0.07) \times 10^{-4}$
$\mu^+\mu^-$	$(3.7 \pm 0.5) \times 10^{-4}$

Table 2.1: ϕ decays [57].

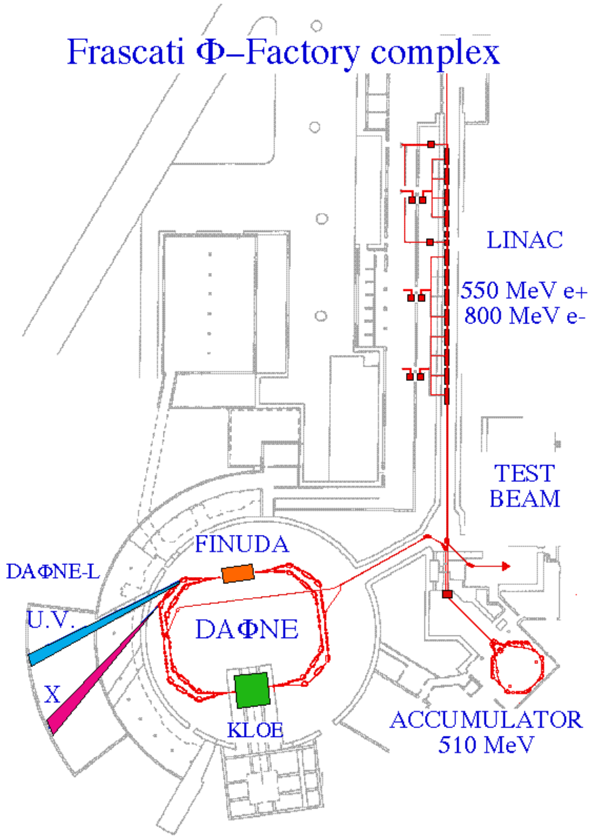

Figure 2.1: Map of the Φ-factory complex.

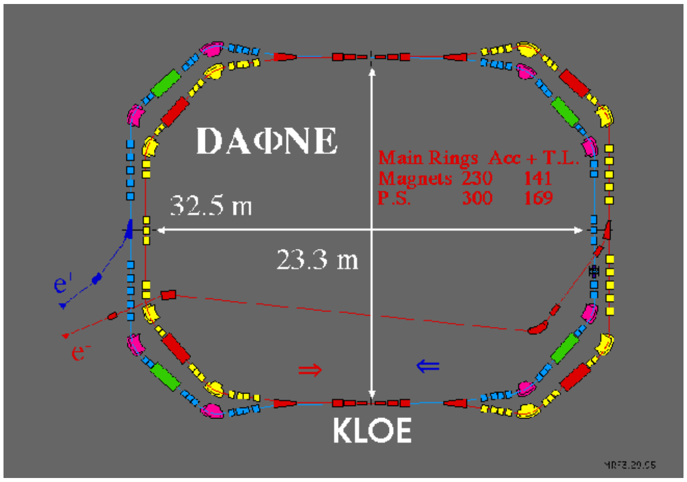

Figure 2.2: Scheme of the two rings of DAΦNE . The KLOE interaction region is shown.

Beam energy	$510\ MeV$
Number of bunches	up to 120
Number of particles per bunch	8.9×10^{10}
Collision frequency	$< 370\ MHz$
Maximum current per ring	$5.2\ A$
Bunch dimensions	$\sigma_x = 2.0\ mm$ $\sigma_y = 20\ \mu m$ $\sigma_z = 3\ cm$
Crossing angle	$25\ mrad$
Luminosity	$5.3 \times 10^{32}\ cm^{-2}s^{-1}$

Table 2.2: DAΦNE design parameters.

Luminosity	$8 \times 10^{31} cm^{-2}s^{-1}$
Bunches per ring	48
Average beams lifetime	$\sim 40'$
Integrated luminosity per day	$\sim 2\ pb^{-1}$

Table 2.3: 2002 data taking parameters.

2.1.1 The DAΦNE luminosity at KLOE

First collisions in the KLOE interaction region after the KLOE installation were detected on April 14, 1999. During the first data taking ($1999 \div 2000$), a total integrated luminosity of $\simeq$ 2.4 pb^{-1} has been collected, with istantaneous luminosity peak between 3 and $5 \cdot 10^{30}$ cm^{-2} s^{-1}. This value lower than the one expected ($5 \cdot 10^{32}$ cm^{-2} s^{-1}) has been improved with some changes:

- the magnetic field of KLOE has been reduced from 6 to 5.6 kGauss,
- the KLOE interaction region has been modified in the optics and supports,
- colliding current has been increased due to the vacuum conditioning and the continuous improvements of the feedback system.

In the $2004 \div 2006$ KLOE run, DAΦNE has delivered an integrated luminosity in excess of 2 fb^{-1} on energy 1019.4 MeV see Figure 3.1 and, in the last part of the run > 0.25 fb^{-1} off peak 1000 MeV.
A high statistics scan of the ϕ resonance has been also performed collecting more than 10 pb^{-1} per point at 4 different energies ($1010, 1018, 1023$, and 1030 MeV).
As shown in Figure 2.4 the machine performance have been continuosly improving during the on-energy run. The highest peak and daily integrated luminosities measured by KLOE have been $L_{peak} = 1.53 \cdot 10^{32}$ cm^{-2} s^{-1} and $L_{day} = 10$ pb^{-1}, respectively.

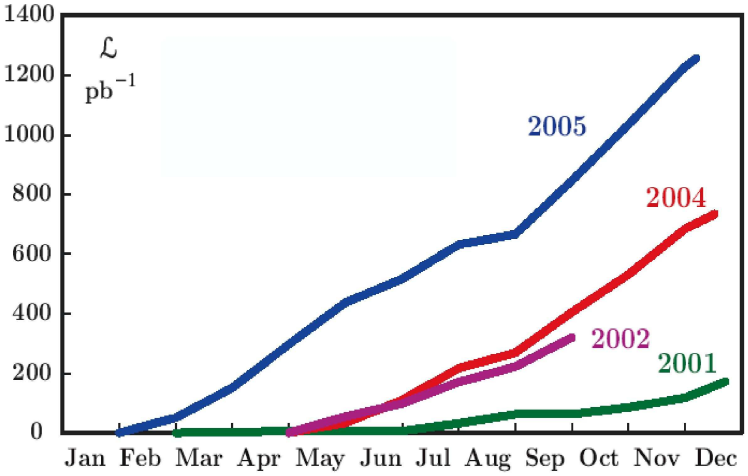

Figure 2.3: Integrated luminosity in pb^{-1} as function of the number of days of data taking for the years 2001 ÷ 2005.

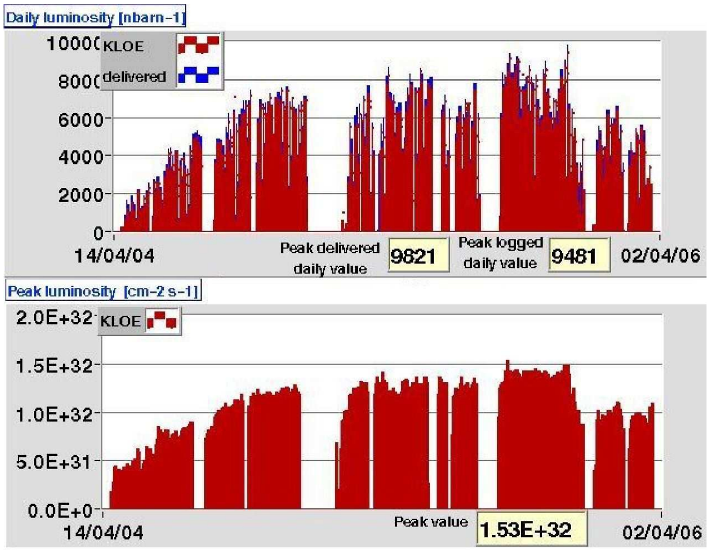

Figure 2.4: Last KLOE run peak and integrated luminosity.

2.2 The KLOE detector

The main goal of the KLOE experiment was the measurement $\Re(\epsilon'/\epsilon)$ with an accuracy of few 10^{-4}. To contain the statistical error below this threshold, the detector has been designed to collect the largest amount of the neutral kaon decays of the ϕ, then the dimensions of the apparatus must be comparable with the decay length of the K_L. Accounting for the kaon lifetimes [57] and momentum, the decay length ($\lambda = \beta\gamma c\tau$) of K_S and K_L are:

$$\lambda(K_S) \sim 0.56\ cm \qquad \text{and} \qquad \lambda(K_L) \sim 350\ cm.$$

The detectable decay products of neutral K mesons are charged and neutral pions, electrons, muons and photons, these coming mainly from neutral pion decays. The momenta are limited by the low energy of the K mesons and range between 50 and 300 MeV/c for charged particles and between 20 and 300 MeV/c for photons. To avoid mismatches in the identification of K_L decays, the detector has to be efficient for these energies with full geometrical acceptance, and has to guarantee an high resolution on the point of conversion of the photons in order to allow the reconstruction of the neutral vertex which correspond to the decay of a neutral pion often produced in kaon decays. The experimental design adopted to fulfill the above requirements consists of a hermetic detector with a cylindrical structure (6 m diameter and 6 m length) surrounding the beam pipe. The main components are:

- a large drift chamber, filled with an helium-based gas mixture;
- a sampling calorimeter made of lead/scintillating fibers, surrounding the chamber.

These parts are inserted inside a superconducting coil which produces a solenoidal magnetic field parallel to the beam axis. An high magnetic field improve the capability to reject the $K_{\mu 3}$ background events respect to the signal $K_L \to \pi^+\pi^-$, thanks to a better vertex reconstruction. Simultaneously it increases the curvature of the tracks and this involves a worst reconstruction of the tracks in the drift chamber. As a compromise between this two effects, a value of 0.52 T has been chosen for the magnetic field. In the following we will refer to an axes system where the z-axis lies along the beams and the x and y-axes are the standard ones, x horizontal and y vertical. In table 2.4 can be found the ranges of momenta of the particle involved in some kaon decays. A schematic transverse section of the detector is shown in figure 2.2 and a 3D view is shown in figure 2.2.

2.2.1 The beam-pipe

The interaction region consists of a sphere (see figure 2.6) of 10 cm radius, corresponding to ~ 17 K_S decay length in order to avoid regeneration. The wall of the beam-pipe is made of AlBeMet, an alloy of beryl-aluminum 60%-40% with thickness 0.5 mm. A

Decay channels	Momenta (Mev/c)
$K_{S,L} \to \pi^+\pi^-$ $\pi \to \mu\nu$	$155 \le p_\pi \le 256$ $p_\mu \le 280$
$K_L \to \pi e\nu$	$p_\pi \le 300$ $p_e \le 260$
$K_L \to \pi\mu\nu$	$p_\pi \le 260$ $p_\mu \le 260$
$K_L \to \pi^0\pi^0$ $\pi^0 \to \gamma\gamma$	$160 \le p_{\pi^0} \le 270$ $20 \le p_\gamma \le 280$
$K_L \to \pi^+\pi^-\pi^0$	$p_\pi \le 170$
$\phi \to K^+K^-$	$120 \le p_K \le 135$
$K^\pm \to \mu^\pm\nu$	$300 \le p_\mu \le 320$
$K^\pm \to \pi^\pm\pi^0$ $\pi^0 \to \gamma\gamma$	$270 \le p_\pi \le 280$ $20 \le p_\gamma \le 180$
$K^\pm \to \pi^0 e^\pm\nu$ $\pi^0 \to \gamma\gamma$	$p_e \le 300$ $20 \le p_\gamma \le 325$
$K^\pm \to \pi^0\mu^\pm\nu$ $\pi^0 \to \gamma\gamma$	$p_\mu \le 290$ $20 \le p_\gamma \le 310$
$K^\pm \to \pi^\pm\pi^+\pi^-$	$p_\pi \le 190$
$K^\pm \to \pi^\pm\pi^0\pi^0$ $\pi^0 \to \gamma\gamma$	$p_\pi \le 180$ $20 \le p_\gamma \le 135$

Table 2.4: Momenta of the particles involved in some of the K_L and $K^\pm$ decays.

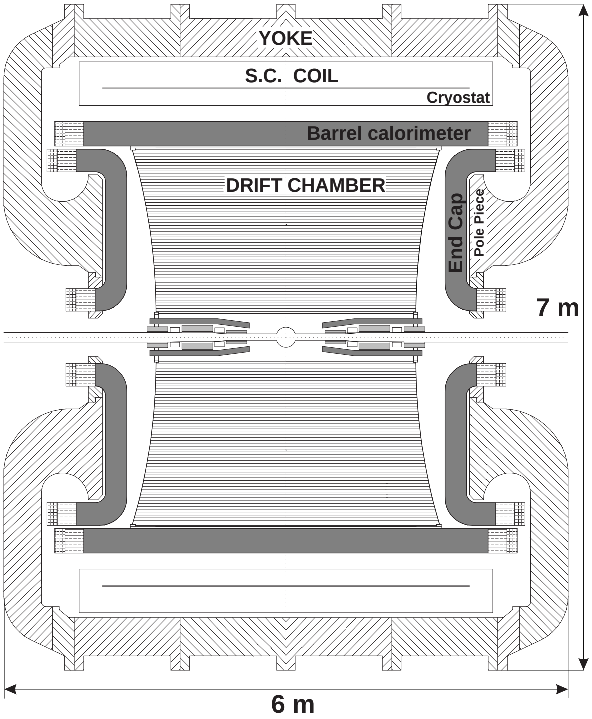

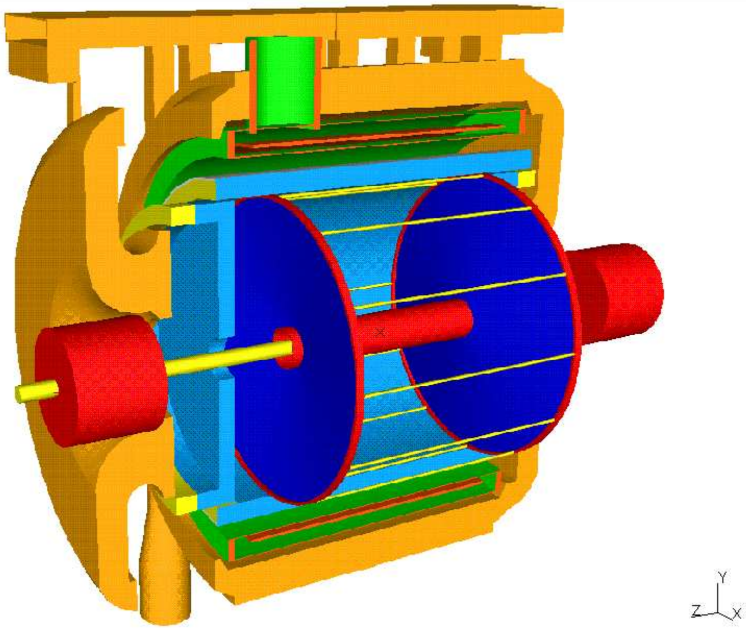

Figure 2.5: Above: vertical transverse section of the KLOE detector. Below: 3D view of the KLOE detector.

small layer of beryllium, thick 0.05 mm guarantees continuity to the pipe inside the sphere. Beryllium has been choosen because of its low atomic number in order to reduce multiple scattering, regeneration, energy loss of particles and photon conversion.

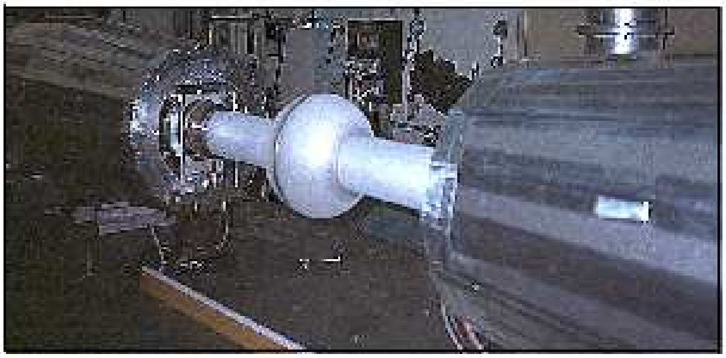

Figure 2.6: Picture of the interaction region; are also visible the quadrupoles.

2.2.2 The drift chamber

The design of the KLOE drift chamber was driven by the event topology of the K_L decays: K_L's have a mean free path of 343 cm, and vertexes that are mostly distributed at large polar angles (proportional to $sin^2\theta$, with respect to the beam axis). Then the drift chamber has to fulfill five main requirements:

- it must have an high and uniform reconstruction efficiency over a large volume, in order to cope with the long decay path of the K_L and the isotropic distribution of its decay products;

- it must have a good momentum resolution ($\Delta p_\perp / p_\perp$) for low momentum tracks ($50 < p < 300\ MeV$), in order to successfully reject the $K_{\mu 3}$ background. In this energy range the dominant contribution to the momentum resolution is multiple scattering:

$$\frac{\Delta p_\perp}{p_\perp} = \frac{0.053}{|B|L\beta}\sqrt{\frac{L}{X_0}}$$

  where $p_\perp$ is the transverse momentum in GeV, β is the velocity of the particle, L is the total track length in m, B is the magnetic field in T and X_0 is the radiation length;

- it must be transparent to low energy photons (down to 20 MeV). The K_L into K_S regeneration on the internal walls must be minimized also;

- it must allow the determination of the K_S flight direction in $\pi^+\pi^-$ decay in order to perform a precise reconstruction of the K_L direction. The goal is to have a track resolution in the transverse plane $\sigma_{R\phi} \simeq 200\ \mu m$ and a vertex resolution $\sigma_{vtx} \simeq 1\ mm$;
- it must provide a trigger signal able to improve the trigger efficiency for the charged decays.

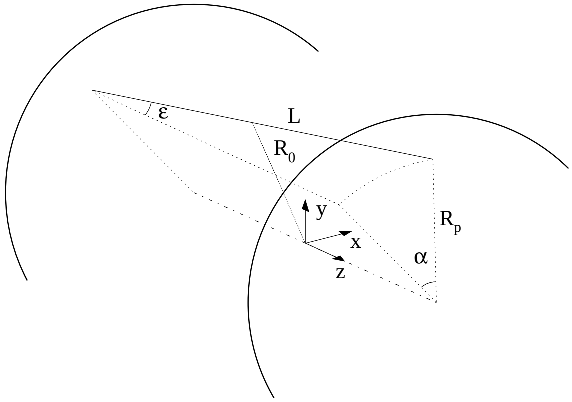

Figure 2.7: Scheme of the stereo angle of the cells.

Figure 2.8: Picture of the drift chamber.

The chosen geometrical solution is a uniform cell structure on a large cylindrical volume, whose length is variable and goes from 2.8 m near the beam-pipe to 3.3 m where the radius is maximum; the outer radius around the interaction point is 2 m,

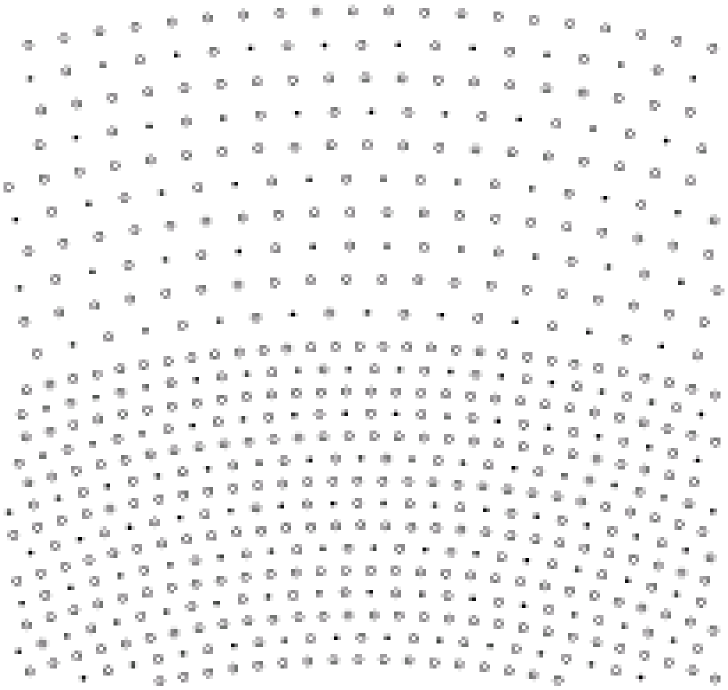

Figure 2.9: Drift cells configuration at $z = 0$; a portion of chamber at the boundary between small cells (inner layers) and big cells (outer layers) is shown. Full dots indicate sense wires, circles indicate field wires.

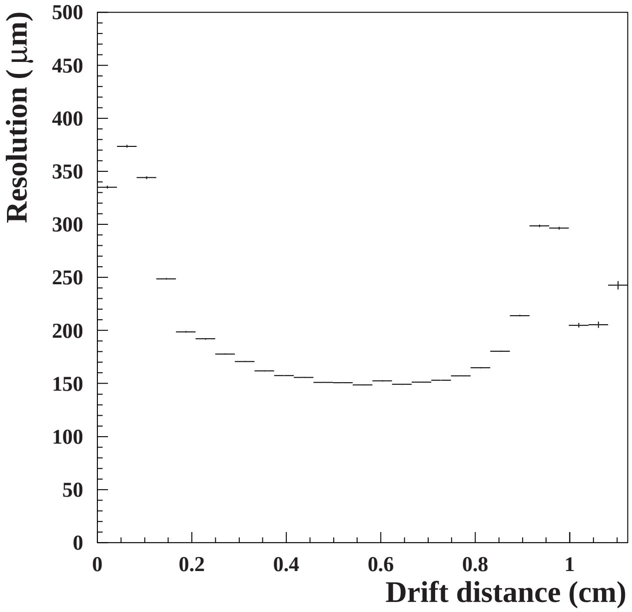

Figure 2.10: Spatial resolution as a function of the drift distance, for 2×2 cm^2 cells of the innermost layer.

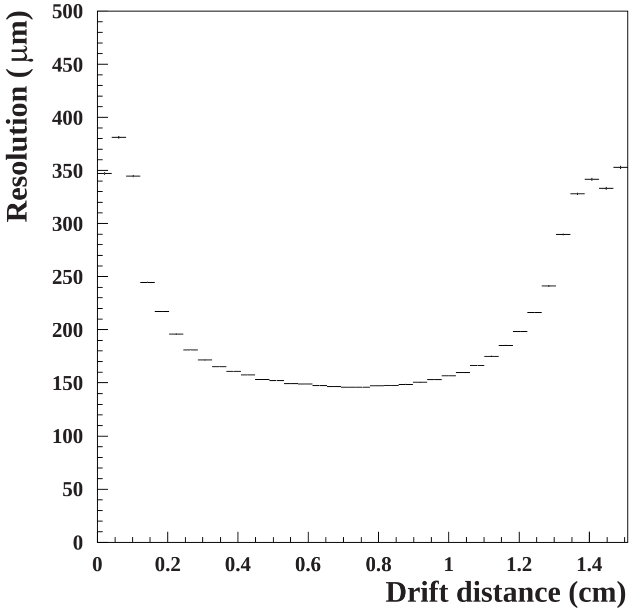

Figure 2.11: Spatial resolution as a function of the drift distance, for 3×3 cm^2 cells of the outermost layer.

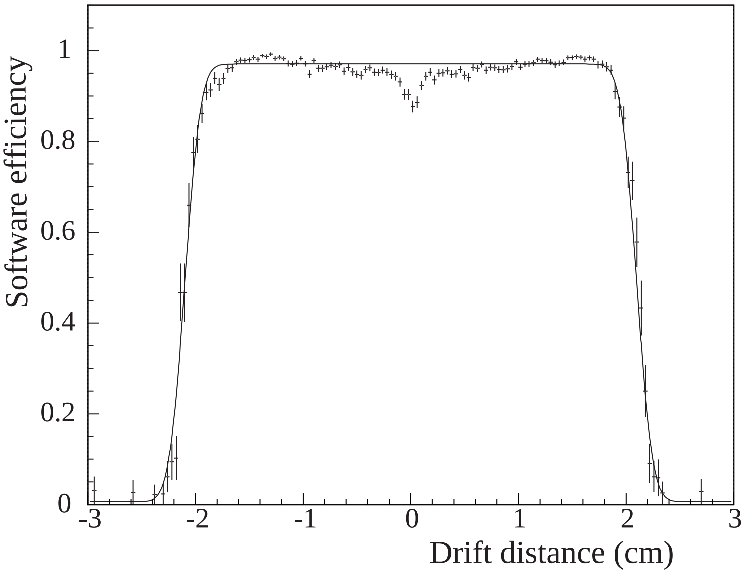

Figure 2.12: Software efficiencies as function of the drift distance.

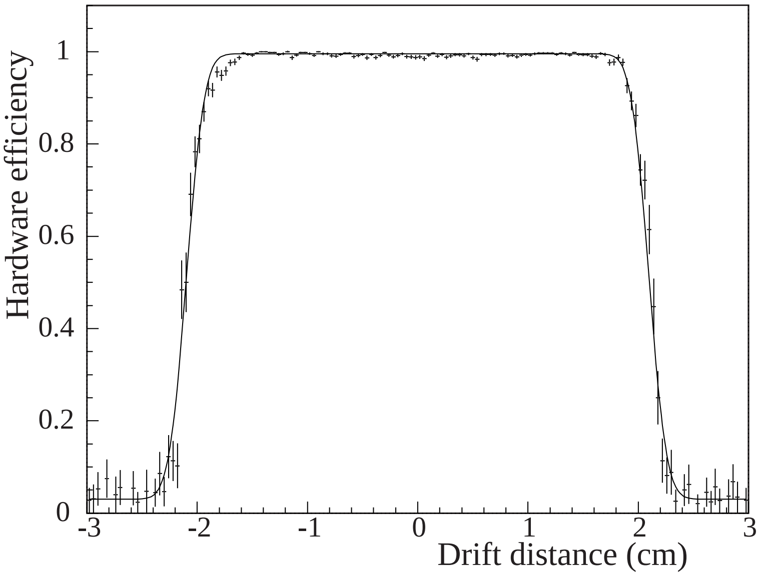

Figure 2.13: Hardware efficiencies as function of the drift distance.

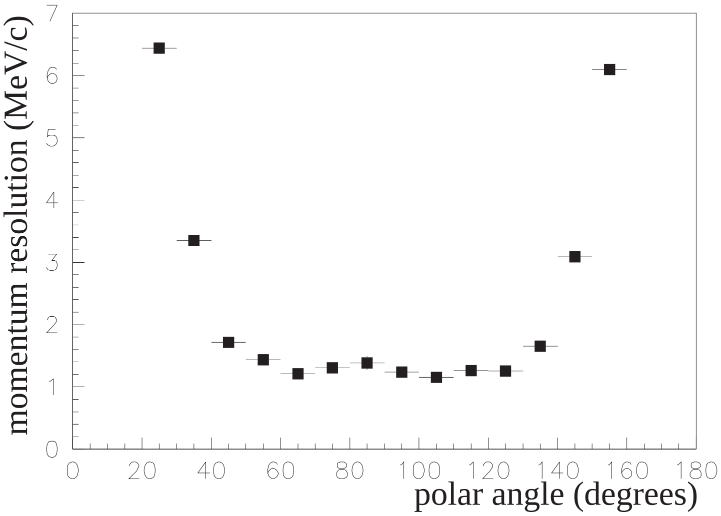

Figure 2.14: The momentum resolution for 510 MeV $e^{\pm}$ from Bhabha scattering events as function of the polar angle of emission.

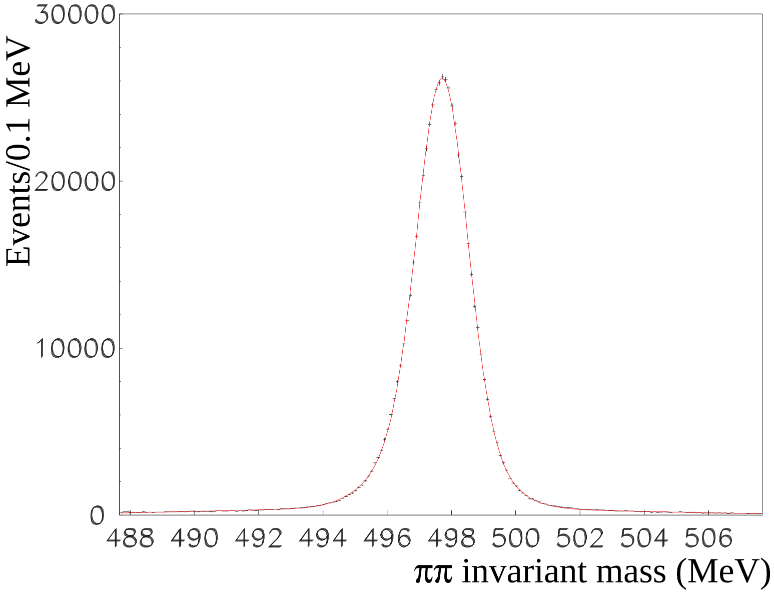

Figure 2.15: $\pi^+\pi^-$ invariant mass distribution as calculated from oppositely charged tracks from the interaction point. The distribution peaks at the correct value for the mass with a r.m.s. width of 0.9 MeV/c^2.

the inner radius is 25 *cm* . In the DC about 30% of the K_L decay. The uniform filling of the chamber has been achieved through a structure of drift cells "almost" square shaped, arranged in coaxial layers with alternating stereo angles which increases in magnitude with radius from ± 60 to ± 150 *mrad*. The stereo angle is defined as the angle between the wire and a line parallel to the z-axis passing through the point on the plate of the DC, where the wire is connected (figure 2.7). The ratio of field to sense wires (3:1) is a satisfactory compromise in maximizing the track sampling frequency, while maintaining the electrostatic stability of the drift cell. The sense wires are made of gold-plated tungsten and their diameter is 25 μm. The field wires are made of silver-plated aluminum and their diameter is 80 μm; to the field wires are applied $\sim$ 1900 V. There are 12 inner and 46 outer layers, the corresponding cell areas are 2×2 and 3×3 cm^2, respectively, for a total of 12582 single-sense-wire cells and 52140 wires.
Materials were chosen in order to minimize the density along the path of neutral kaons, charged particles and photons. A carbon fiber composite ($\leq 0.1X_0$) has been chosen for the chamber shell. The gas used is a 90% helium, 10% isobutane mixture. The helium is the active component of the mixture and thanks to its low atomic mass reduces the effect of multiple scattering and regeneration. The isobutane acts like quencher, it absorbs UV photons produced in recombination processes in order to avoid the production of discharges in the DC, it can't be more than 10% due to its flammability. The mixture has a radiation length $X_0 \simeq 1300$ m, while taking into account also the presence of the wires, the average radiation length in the whole chamber volume is about $X_0 \sim 900$ m.
The cell efficiency is determined using cosmic ray tracks with more than 96 hits. The "hardware efficiency" is defined as the ratio of the number of hits found in a cell to the number of tracks crossing the cell. This efficiency is $\sim$ 99.6% both for small and big cells and it is constant over the whole drift chamber volume (see figure 2.13). The "software efficiency" is defined requiring the hit found in the cell to be used by the track fit and it is $\sim$ 97%. As can be seen in figure 2.12, the software efficiency is lower for small drift distances, this is due to the worse resolution close to the wires due to non-linearity of space to time (s-t) relations.
Using samples of Bhabha-scattering events, the momentum resolution for 510 MeV $e^{\pm}$ has been evaluated. It can be seen in figure 2.14 that for $50^\circ < \theta < 130^\circ$ (θ being the angle between the z axis and the direction of the particle, polar angle of emission) the momentum resolution are $\sigma_p \simeq 1.3$ MeV and $\sigma_p/p = 2.5 \times 10^{-3}$.

2.2.3 The electromagnetic calorimeter

The calorimeter has to perform 4 main tasks:

- it must have a good time resolution ($\simeq$ 100 ps) and a good determination ($\simeq$ 1 cm) of the photon conversion point, in order to allow the K^0 neutral decay vertex determination with an accuracy of few mm;

- it must have an high discriminating power between $K_L \to 2\pi^0$ and $K_L \to 3\pi^0$; therefore the calorimeter has to be hermetic (98% of the solid angle), with good energy resolution ($5\%/\sqrt{E[GeV]}$) and fully efficient over the range $20 \div 300\ MeV$;
- it must have some particle identification power, to help with the rejection of $K_L \to \pi l \nu_l$ background from the $K_L \to \pi^+\pi^-$ $\mathcal{CP}$ violating signal;
- it must provide a fast first level trigger.

A lead-scintillating fiber sampling calorimeter has been designed to fulfill these requirements. Scintillating fibers offer several advantages, in particular they provide good light transmission over the required distances, up to $\sim 4.3\ m$. Superior timing accuracy is obtained because of single mode propagation. The calorimeter shape is adapted to the geometrical requirements obtaining good hermeticity.
The cylindrical barrel consists of 24 modules $4.3\ m$ long $\times$ $23\ cm$ thick with trapezoidal cross-section, with bases of 52 and 59 cm. Each endcap consists of 32 vertical modules $0.7 \div 3.9\ m$ long and 23 cm thick. The modular scheme can be seen in figure 2.18 The barrel covers a region between 40° and 310°, the endcaps covers the angles included between 9° and 46° and between 134° and 171° respectively. The cross-section of the modules is rectangular, of variable width. Modules are bent at the upper and lower ends to allow insertion into the barrel calorimeter and also to maintain the photo-tube axes parallel to the magnetic field. Due to the large overlap of barrel and endcaps, the KLOE calorimeter has no inactive gap at the interface between those components. The central endcap modules are vertically divided into two halves to allow the passage of the beam-pipe.

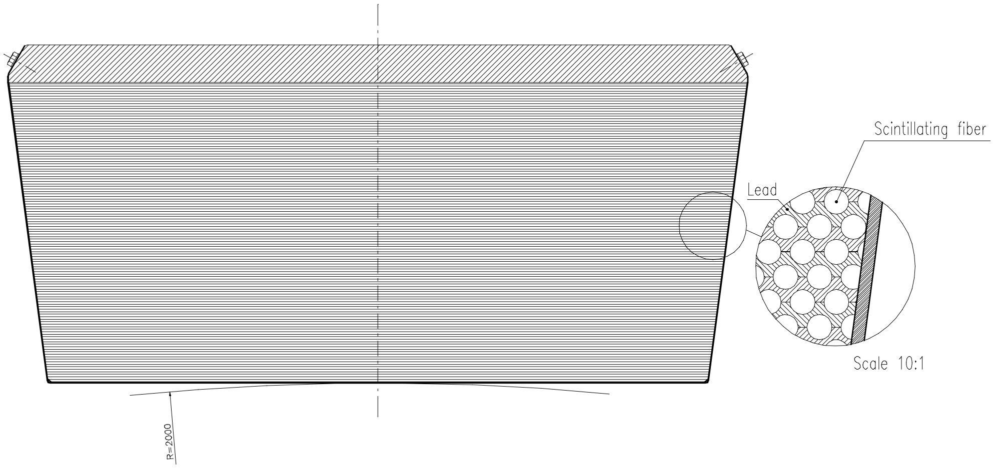

Figure 2.16: Schematic view of the fiber-lead composite of each module of the electromagnetic calorimeter.

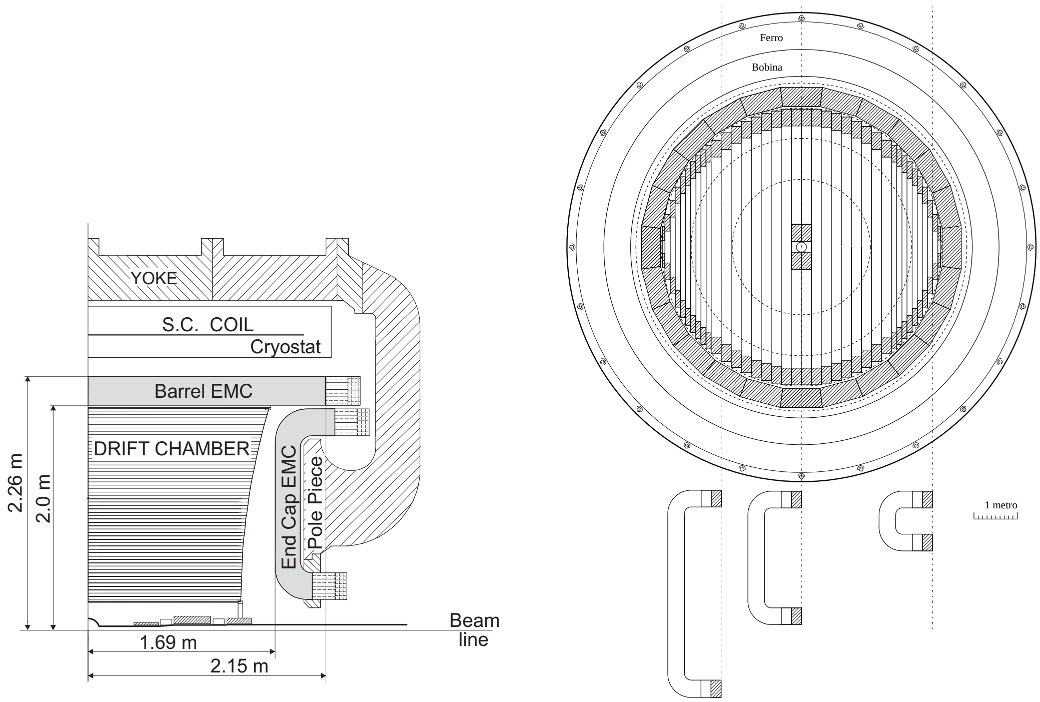

Figure 2.17: On the left: transverse cross section of the KLOE detector, it is possible to see the shapes of the endcap EMC modules. On the right: vertical cross section of the KLOE detector.

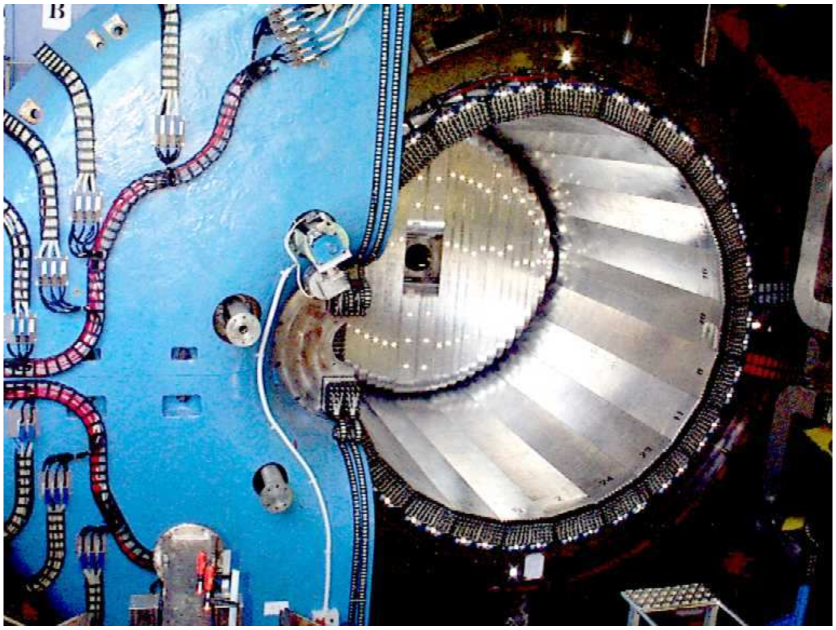

Figure 2.18: Picture of the electromagnetic calorimeter.

All modules are made of 200 grooved, 0.55 mm thick lead foils alternating with 200 layers of scintillating fibers with diameter 1 mm, glued in the grooves with a special epoxy, which is not harmful to the fiber plastic. Fibers are mostly orthogonal to the entering particles in order to avoid channeling. The ratio by volume of the different component material is: lead:fiber:epoxy=42:48:10, the high scintillator content is necessary to maximize the number of collected photons per MeV released by the impinging particle, so to optimize the energy and time resolutions. The attenuation length of the fibers is $\lambda \geq 3\ m$, while the average density is 5 g/cm^3, the radiation length is $\sim$ 1.5 cm and the overall thickness of the calorimeter is $\sim$ 15 radiation length. Light is collected on both sides of each module, via light pipes which match almost square portions of the module end faces to 4880 photo-tubes. The read-out splits the calorimeter into five planes in depth, each deep 4.4 cm with the exception of the last which is 5.2 cm deep. In the transverse direction each plane is subdivided into cells 4.4 cm wide. The set made of 5 cells lined up, one for each transverse plane is named "column". The read-out $r - \phi$ $(x - z)$ granularity for the EMC is finally $\sim 4.4 \times 4.4\ cm^2$ slightly varying in size across the modules. This allows a very good spatial resolution.

The energy deposit in each cell is obtained from the charge measured at each side of the modules by the ADC's. The cell time is derived by time intervals measured at each side of the modules by the TDC's. The difference of the signal arrival times at both ends allows to reconstruct the coordinate along the fibers. Therefore the resolution on the z longitudinal coordinate depends on the statistics of photoelectrons: $\sigma_z \sim 9\ mm/\sqrt{E[GeV]}$.

The energy resolution and the linearity of the energy response have been measured using photons from radiative Bhabha events and from $\phi \to \pi^+\pi^-\pi^0$ events. In both cases the photon energy E_γ is estimated by tracks momenta (reconstructed by the drift chamber) and it is compared with the measured cluster energy E_{CL}. The fractional resolution σ_E/E_γ and the relative deviation from linearity $(E_\gamma - E_{CL})/E_\gamma$, obtained from radiative Bhabha events are plotted in figure 2.19 as function of the photon energy. Linearity is better than 1% for $E_\gamma > 75\ MeV$, while deviations from linearity at the $4 - 5\%$ level are observed for low energies, probably due to the loss of shower fragments. The fit of the energy resolution to the function $a/\sqrt{E[GeV]} + b$ gives a negligible constant term, proving that the resolution is dominated by sampling fluctuations, and gives a stochastic term $a = 5.7\%$. Compatible results are obtained from $\phi \to \pi^+\pi^-\pi^0$.

The time resolution derived by the analysis of various radiative ϕ decays is shown in figure 2.20. Good agreement between the measurements for different channels is observed down to 100 MeV. The curve in the plot is the result of a fit:

$$\sigma_t = \frac{54\ ps}{\sqrt{E[GeV]}} \oplus 140 ps \tag{2.1}$$

where the sampling fluctuation term is in agreement with test beam data [58] and the second term is a constant to be added in quadrature. The constant term is given by the quadrature sum of two contributions: the intrinsic time spread due to the finite length

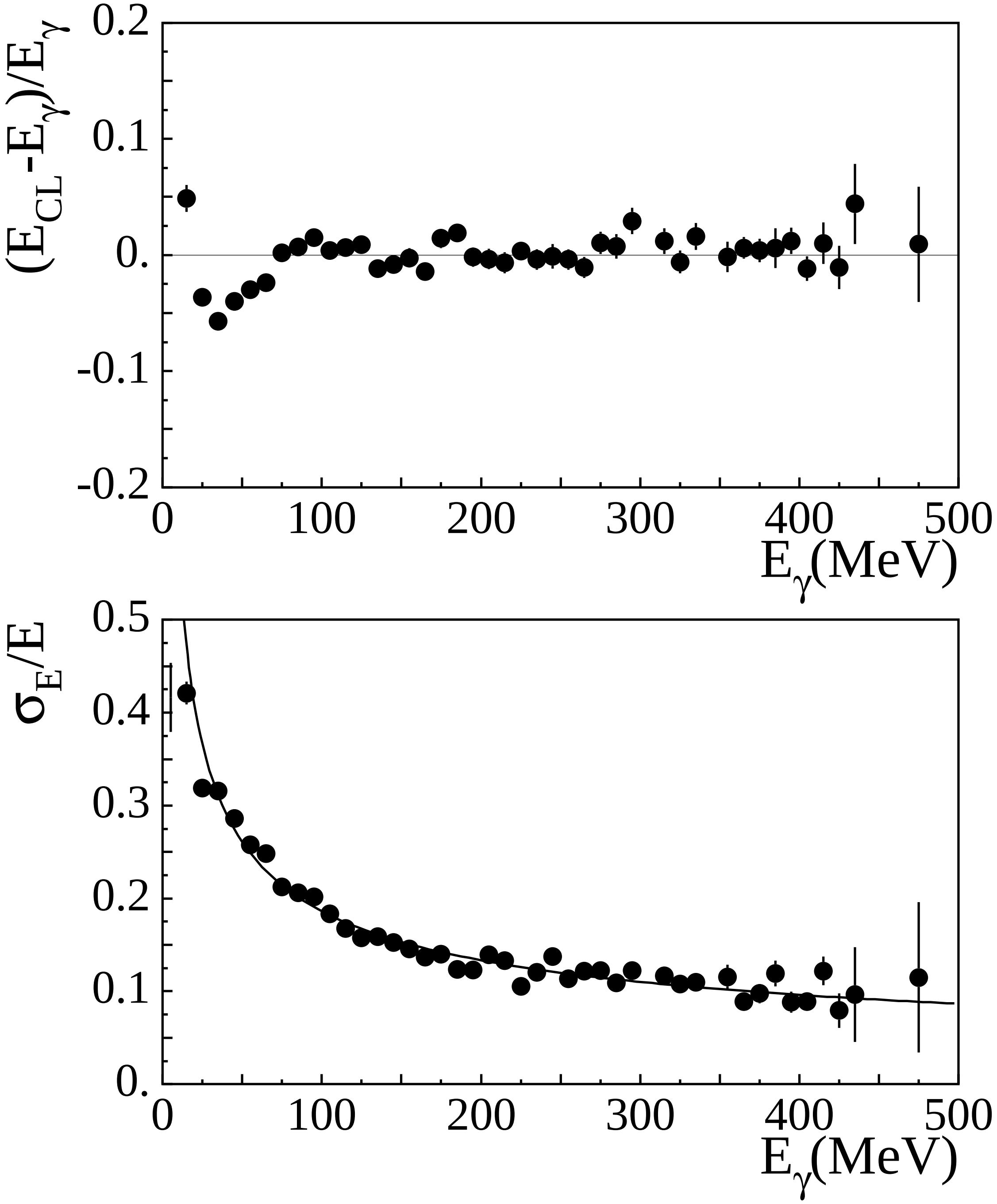

Figure 2.19: Above: linearity of the calorimeter energy response as a function of the photon energy, for radiative Bhabha events. Below: energy resolution of the calorimeter as a function of the photon energy, for radiative Bhabha events.

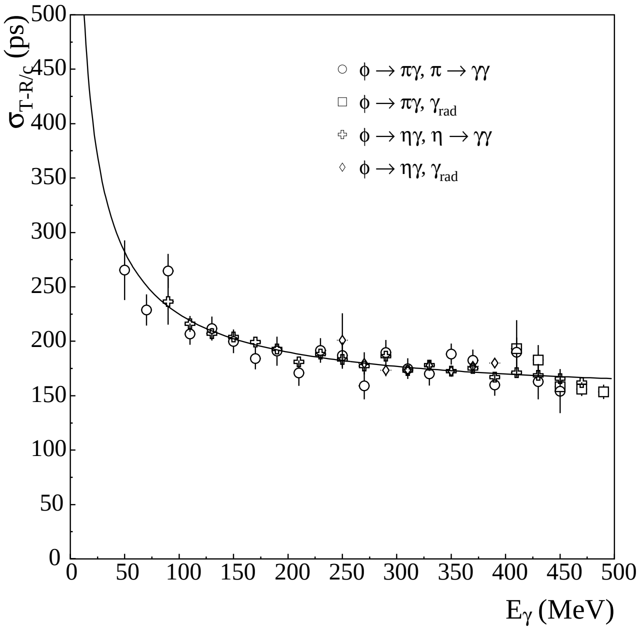

Figure 2.20: Time resolution of the calorimeter as a function of the photon energy, for radiative ϕ decays.

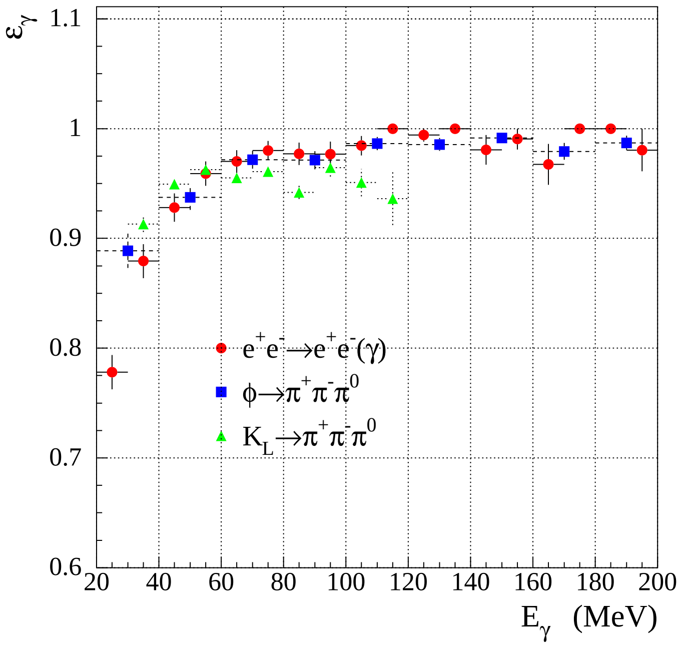

Figure 2.21: Photon detection efficiency as a function of the photon energy, as measured from radiative Bhabha, $\phi \to \pi^+\pi^-\pi^0$ and $K_L \to \pi^+\pi^-\pi^0$ samples.

of the luminous point in the beam direction, which contributes for $\sim 125\ ps$, and the resolution of the synchronization with the DAΦNE radiofrequency, which contribute for $\sim 50\ ps$. Compatible results are obtained from $\phi \to \pi^+\pi^-\pi^0$ and from radiative Bhabha decays.

The photon detection efficiency is an important quantity for various analysis. Three data samples have been used to estimate it: radiative Bhabha events and $\phi \to \pi^+\pi^-\pi^0$ decays, which provide a source of photons coming from the interaction point, and $K_L \to \pi^+\pi^-\pi^0$ decays, in which the photons originate from a K_L decay vertex in the DC volume. The detection efficiency ϵ_γ, resulting from these three analysis, are shown as a function of the photon energy in figure 2.21. A constant value of more than 98% is observed above 100 MeV, while a loss in efficiency is evident below 100 MeV.

2.2.4 The quadrupole calorimeters (QCAL)

In order to achieve the maximum possible luminosity, the last focusing quadrupoles are very close to the interaction point, inside the KLOE detector. The presence of this quadrupoles limits the geometrical acceptance for photons coming from K_L^0 decays encreasing by a factor 5 the probability to lose one single photon, then a sensitive detector covering the quadrupoles is certainly welcome.

Detector design must satisfy stringent weight and volume requirements to fit between the quadrupoles and the drift chamber inner wall. The adopted solution is a sampling calorimeter made of lead and scintillator tiles see Figure 2.22.

The calorimeter is divided in 16 radial section whose light is collected by wavelength shifting fibers. Each fiber curved and shared between two non adjacent sector allowing to place the PMs only on the side far from the interaction point and avoiding double hits on the same fiber.

Looking from the interaction point each radial sector has a conical part (50 cm long) followed by a cylindrical one (31 cm long). Each sector contains 16 lead planes (2 mm thick) and 15 scintillator layers (1 mm thick) for a total of ~ 5.5 radiation lengths. PMs are of mesh-dynode type to reduce the effect of magnetic field.[1] The signal coming out from each PMs is splitted in two: the first is shaped and sent to the ADC, the second is discriminated and sent to the TDC. Main request for the QCAL detector is the photon detection efficiency. This can be measured using cosmic rays selected by the drift chamber. The energy released by a cosmic MIP is equivalent to that of a 75 MeV photon.

The efficiency for the single sector is 98 %, but when both signal at the fiber ends are requested the efficiency drop down to 75 %. The hit coordinate along the fiber is determined by the difference in the arrival time at two ends from:

$$z = L - v\frac{t_2 - t_1}{2} \tag{2.2}$$

---

[1] Nonetheless a gain reduction of $\sim 60\%$ has been observed once the PMs have been installed inside the KLOE magnetic field.

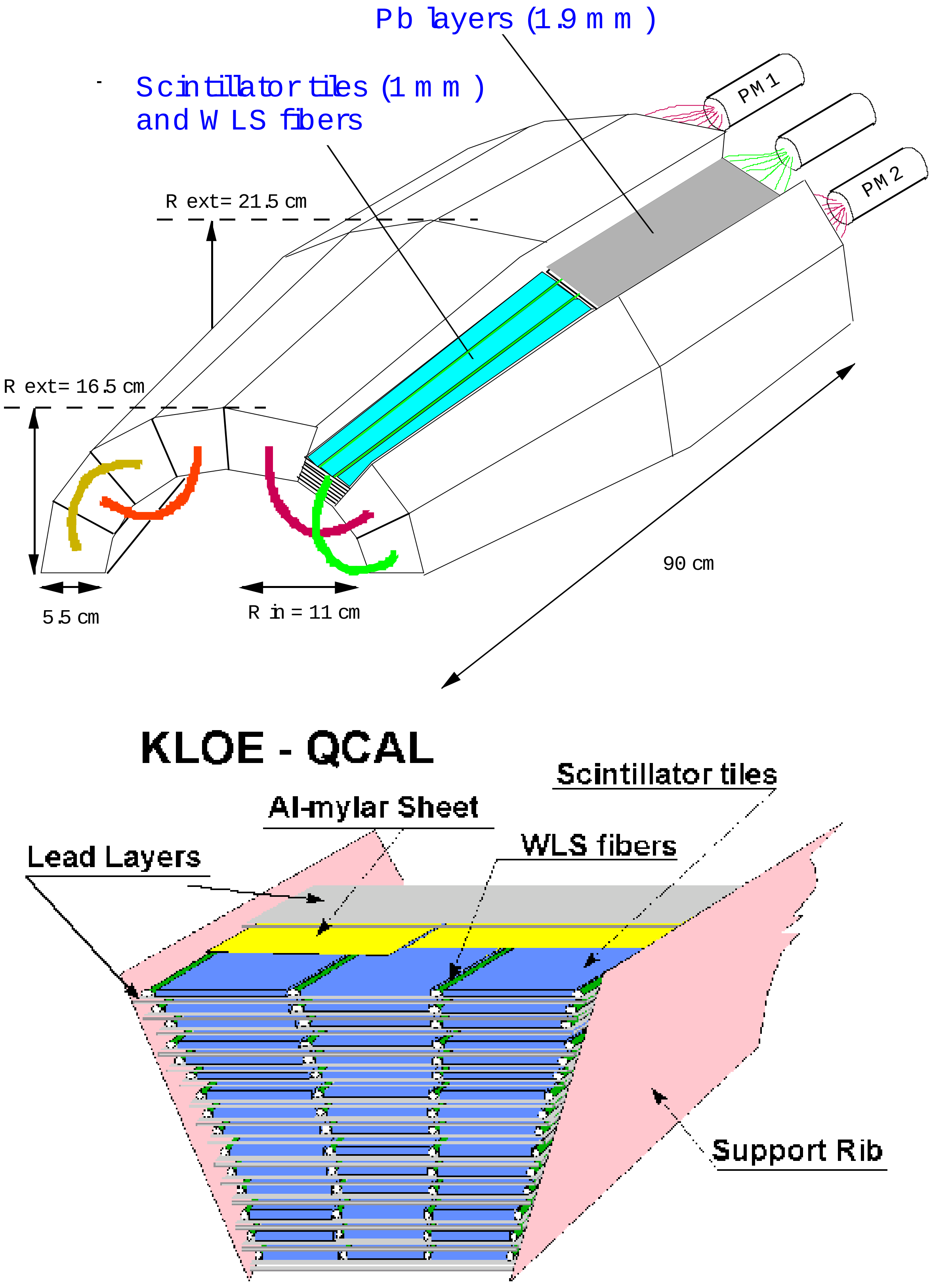

Figure 2.22: Schematic view of a quadrupole calorimeter.

where L is half of the total fiber length and v is the light speed in the fiber. Photon detection efficiency has been evaluated using $K_L^0 \to \pi^0\pi^0\pi^0$ and $K_L^0 \to \pi^+\pi^-\pi^0$ samples and looking for a photon not detected by calorimeter that intersects the QCAL region. The result for a single photon efficiency is $92 \pm 4\%$.
Time resolution obtained with cosmic rays events is:

$$\sigma(t) = 0.9 \pm 0.2 \text{ ns} \tag{2.3}$$

corresponding to:

$$\sigma(t) = \frac{240 \text{ ns}}{\sqrt{E(\text{GeV})}} \tag{2.4}$$

Energy resolution is expected to be larger than 40% and indicates that QCAL detector can be used as photon counter but not a precise calorimeter.

2.2.5 The trigger system

The main goal of the KLOE trigger system is to:

- produce a trigger signal for all ϕ events;
- recognize Bhabha and cosmic-ray events and accept a downscaled sample for calibration purposes;
- reject the machine background.

During years 2000-2001, with luminosity of $\sim 10^{31}\ cm^{-2}s^{-1}$, the average trigger rate was about 2.5 KHz. Of those only $\sim 250\ Hz$ were due to ϕ events and downscaled Bhabha (a downscaled sample of Bhabha, and also of cosmic rays, events are acquired and saved on tape for calibration purposes). About 400 Hz were due to downscaled cosmic rays, while an additional $\sim 650\ Hz$ were due to cosmic rays escaping the trigger veto. The remaining $\sim 1.2\ KHz$ came from machine background and were rejected by the event selection filters.
There are two main sources of background. One is due to Bhabha events at small angles, where electrons and positrons hit the low-β quadrupoles and produces showers inside the detector. The other source is due to particle losses from the DAΦNE beams. These off-momentum particles come from beam-gas interactions or Touschek scattering.
The DAQ system has been designed for an average throughput of 50 $Mbytes\ s^{-1}$, equivalent to a total trigger rate rate of 10 KHz. The trigger must provide good background rejection in order to not overload the DAQ, since increasing the luminosity also machine background increases and for the design luminosity its rate was evaluated of the order of hundreds of KHz.
The trigger is based on local energy deposit in calorimeter and multiplicity information from the drift chamber. It is composed by two levels (see figure 2.23) in order to both

produce an early trigger with good timing to start the FEE operations and to use as much information as possible from the drift chamber. Specifically, after the arrival of a first level trigger, additional information is collected from the drift chamber, which is used, together with the calorimetric information, to confirm the former and to start the DAQ system. The calorimeter triggers on local energy deposits larger than a programmable threshold. Two thresholds are given for each EMC signal, the first at low energy $\sim$ 50 MeV in order to trigger on low energy particles from ϕ decays entering the calorimeter (Low Energy Threshold, LET), and the second at high energy $\sim$ 350 MeV in order to identify and reject (or accept as downscaled sample) Bhabha events (BhaBha Trigger, BBT).

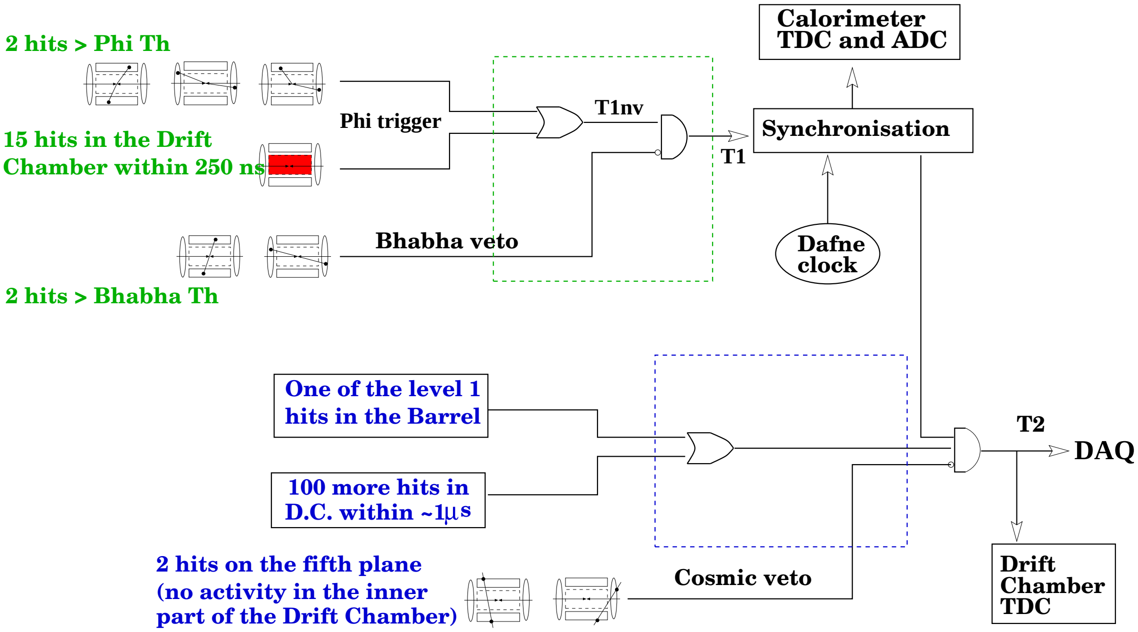

Figure 2.23: KLOE trigger logic.

The drift chamber triggers on the multiplicity of fired wires: each sense wire signal, after preamplification, is fed into the discriminator card where signals for the TDCs and the trigger are formed; for the trigger they are formed to a width of 250 ns, *i.e.* the coincidence width which optimizes both signal efficiency and background rejection, and produces a fast trigger signal.

The **first level** trigger algorithm can be summarized as follows (see figure 2.23):

- *ϕ trigger:* (2 calorimeter LET hits with Barrel-Barrel, Barrel-Endcap or Endcap-Endcap topology) OR (15 drift chamber hits within 250 ns).

- *Bhabha veto:* 2 calorimeter BBT sectors with Barrel-Barrel or Endcap-Endcap topology.

The level one trigger T1 sets a 2 μs long acknowledge signal, which vetoes other first level triggers and allows signals formation from the drift chamber cells.
Before being distributed to the calorimeter FEE, the first level trigger is synchronized with a resolution of 50 ps with the DAΦNE radiofrequency divided by 4 ($T = 10.8\ ns$). Therefore the calorimeter TDCs measure the time with respect to a bunch crossing coming n periods after the collision that originated the event, where n has to be determined by the offline reconstruction of the event. This technique allows us to preserve the resolution on time measurement at the level of picosecond, which would be otherwise spoiled by the intrinsic jitter of the trigger signal formation.
At the end of the dead time the trigger system asks for a confirmation of the level 1 decision. The signal from these dedicated channels are treated in the same way as those used to define the ϕ or Bhabha calorimetric triggers but with threshold chosen to be equal to the average energy released in a cell by a minimum ionizing particle MIP ($40 \div 50\ MeV$). Once two sectors are above threshold, the cosmic rays bit is activated and the event flagged. To avoid rejection of $\mu^+\mu^-$ events, which trigger easily the external planes of the calorimeter, a third level trigger (T3) has been developed. Each event detected as cosmic ray events by the second level trigger are flagged and not rejected, then these events pass through the T3 filter before being written on tape. The T3 filter performs a fast preliminary pattern recognition looking for tracks coming from the interaction point. If no track is coming from the IP the event is rejected. The level two trigger T2 gives the stop to chamber TDCs and starts the data acquisition. The **second level** algorithm can be summarized in this way (see figure 2.23):

- *ϕ trigger:* (at least 1 calorimeter hit in the Barrel or 3 hit in the same Endcap) OR (40 drift chamber hits integrated during 850 ns after T1).
- *Cosmic flag:* 2 hits on the external plane of the calorimeter with Barrel-Barrel or Barrel-Endcap topology.

The cosmic flag

The cosmic flag requires two energy release above threshold on the outermost plane, the fifth, of the calorimeter in the Barrel-Barrel or Barrel-Endcap configuration. The distribution of the energy collected on the fifth plane of the calorimeter barrel on a cosmic ray run is shown in figure 2.24. From the position of the peak it follows that a 30 MeV threshold allows for an efficient selection of the cosmic rays impinging on the calorimeter. It is also possible to see that the threshold is function of z coordinate along the calorimeter. With this choice of threshold the trigger rate on cosmic rays decreases from 2.6 KHz without flag, to 0.68 KHz, thus giving an efficiency in cosmic ray events identification of $\sim$ 80%. From figure 2.24 it is evident that a decrease in the energy threshold does not produce a big gain in the rejection capability, while starting to be effective on the events of physical interest.
Actually the cosmic flag inefficiency is dominated by the geometry of the apparatus. The mechanism is shown in figure 2.25: the cosmic rays which cross the calorimeter

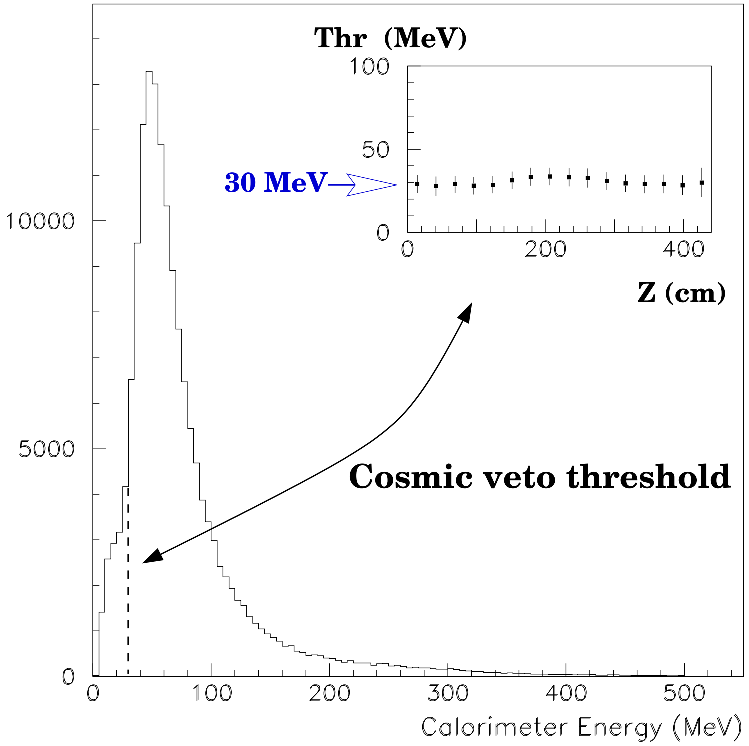

Figure 2.24: Energy released on the fifth plane of the calorimeter for cosmic events. In figure is also shown the position of the cosmic flag threshold. It is also possible to see that the threshold is function of z coordinate along the calorimeter.

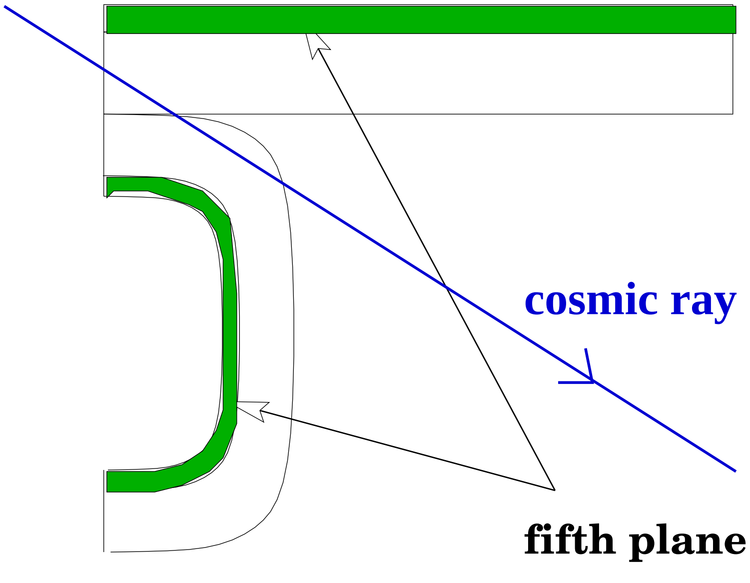

Figure 2.25: Topological explanation for cosmic flag inefficiency.

on the external ring at the edge between the barrel and the endcaps do not fire any sector on the external plane. The spatial distribution of the clusters on the calorimeter confirm the hypothesis on the topological nature of the flag inefficiency.

EMC trigger

For the trigger purposes the fine granularity of the calorimeter is not needed, therefore the signal coming from the 4880 photo-multipliers are summed, shaped and discriminated, in order to define 240 "trigger sectors". This concentration is a compromise between the goal of minimizing the number of the trigger signal and the desire of triggering on single particles.
The calorimeter barrel drives three groups of 48 trigger channels named "normal", "overlap" and "cosmic" series. Each barrel trigger sector in the "normal" and "overlap" series is made of 5 cells × 6 columns, being the columns of each series placed on top of the other by half sector width (see figure 2.26). The cosmic series is used for the cosmic flag and consists only of the cells of the fifth plane of the calorimeter. In total there are 48 × 3 sectors.
The geometry of the trigger sectors in the endcaps is more complex and, like in the case of the barrel it includes two overlapping series of sectors plus the cosmic series. Since particle multiplicity is higher in the forward region, mostly for background events, the normal and overlap series are segmented in groups of 4 calorimeter columns in the zone close to the beam axis, and 5 or 6 elsewhere. In total there are 20 sectors for the normal series, 16 for the overlap and 12 for the cosmic.
The sum of the cells to "form" a column is performed by 164 Splitter/Discriminator/Sum (SDS) boards, which split the signal into three different paths to the ADCs, the TDCs and the trigger. The sum of the six columns of a given trigger sector is performed by the so-called PIZZA board. The analog signal of each trigger sector is performed at both its sides, labeled A and B in the following (see figure 2.27), and goes from the PIZZA to the DIgitiser-SHaper DISH module (each DISH module includes six trigger sectors), here it is compared to an high and a low threshold which can be fixed during DAQ initialization. Whenever a signal crosses the threshold a logic signal T of length 35 ns. The four logical signal T_A^{low}, T_A^{high}, T_B^{low}, T_B^{high} generate the $\mathbf{T}$ signal for each sector according to the logical equation: $\mathbf{T} = (T_A^{low}\ \mathbf{AND}\ T_B^{low})\ \mathbf{AND}\ (T_A^{high}\ \mathbf{OR}\ T_B^{high})$. This two-threshold scheme is applied in order to obtain as much as possible uniform response as a function of the coordinate along the fibers of the energy deposit, so minimizing the effect of the light attenuation along the fibers. The resulting effective threshold profile is shown in figure 2.28.

The $\mathbf{T}$ signal asserted by the DISHes is 70 ns long in order to cover the spread in particle arrival times and not fire twice the same trigger sector. Two couples low-high threshold exist, the first generates a LET effective threshold and the second generates a BBT effective threshold. The PASTA (Precise Analog STAge) board performs the count of the multiplicity of the trigger sector fired. At least two trigger sectors must override the LET effective threshold, once this requirement has been verified by the

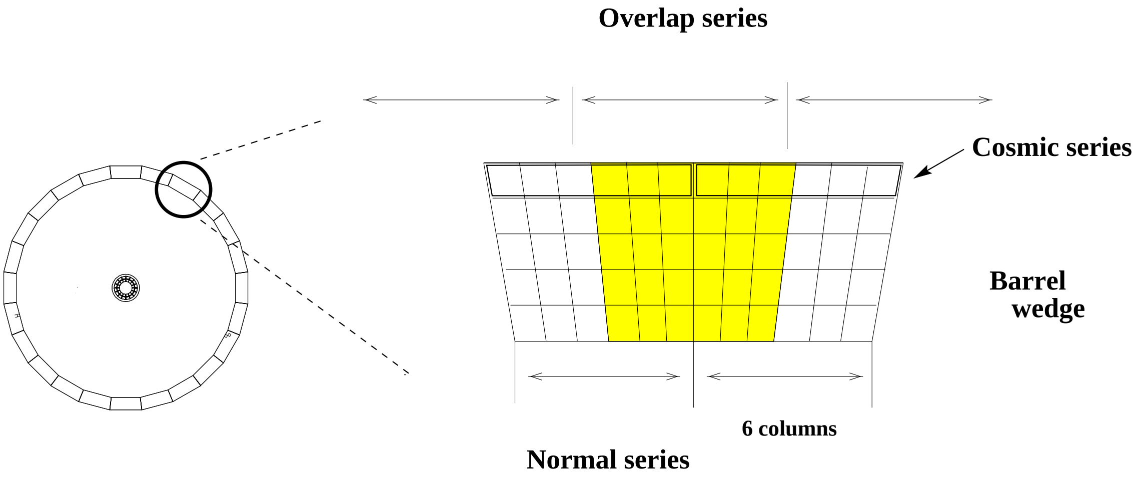

Figure 2.26: Trigger sector in the barrel. It is possible to see the two series, the normal and the overlap.

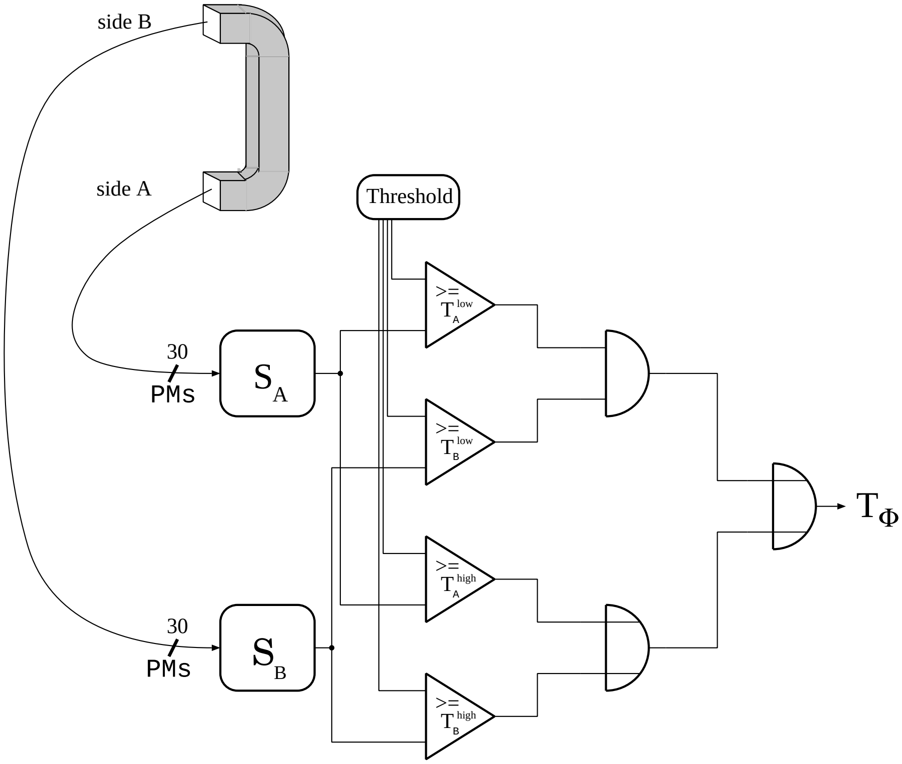

Figure 2.27: Block diagram of the calorimeter trigger.

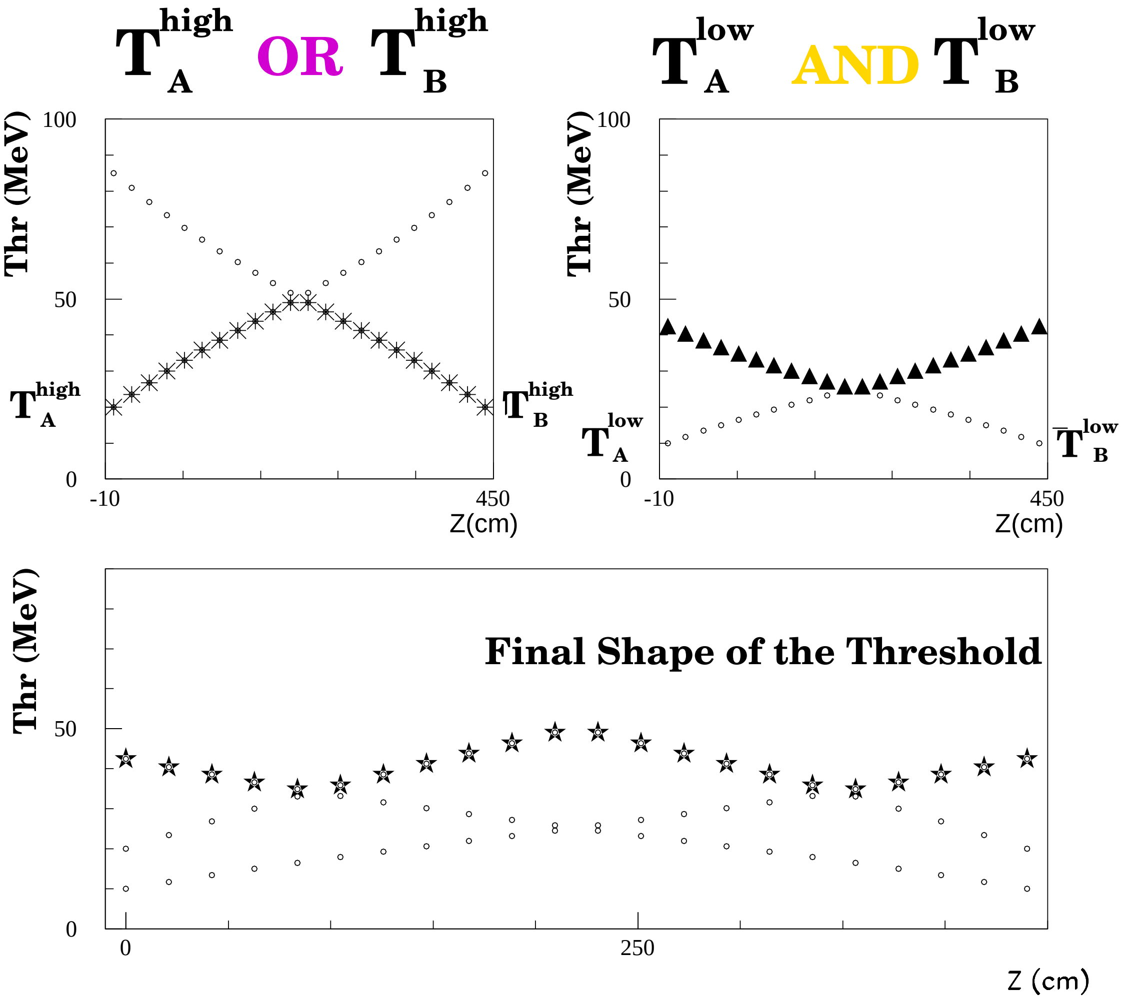

Figure 2.28: The AND of low threshold and the OR of the high threshold as function of the z of the impinging particle are shown together with their AND which is the effective threshold.

Trigger ORganiser and Timing Analyzer (TORTA) board, it asserts the EMC first level trigger T1C. If at least one of those cluster is in the barrel, the TORTA generates the second level calorimeter trigger T2C.

DC trigger

The DC trigger is based on the multiplicity of hit wires. The FEE (Front End Electronics) stage of the DC is made by 280 ADS (Amplifier/Discriminator/Shaper) boards, with 48 channels each, which provide digital signals for the TDCs and the signal for the trigger. For this purpose, the signals formed to a width of 250 ns are summed by the ADS boards in groups of 12 contiguous wires, and then sent to 20 SUPPLI (Sum Unit Providing Plane Information) boards, housed in the same FEE crates, where the counting of the field wires on half drift chamber planes is performed.
The output signals from the SUPPLI boards are sent to three Pre-CAFFE (Chamber Activity Fast FEtch) boards which join the half-plane multiplicity information and pack the drift chamber layers in groups of 5-6, producing at the output the multiplicity signal from 9 super-layers. This procedure allows to protect against triggering on low momentum particles spiraling toward the endcaps, which produce high multiplicity in a group of contiguous planes. At the end of the chain the CAFFE board sums the signals of the super-layers to produce a current signals proportional to the number of fired wires in the chamber within 150 ns. A level one drift chamber (T1D) is delivered whenever this current exceeds the value corresponding to 15 fired wires / 150 ns. For the second level the current signal is sampled at 16 MHz and stored in a 1 μs long pipeline, which allows to perform a running sum of the multiplicity integrated during this time interval. If the measured multiplicity is higher than the given threshold, 120 hits, the second level trigger (T2D) is generated.

Trigger signal generation and DAQ interface

The multiplicity signals from the calorimeter and the first and second level chamber triggers, T1D and T2D, are sent to the TORTA, that merges all the informations to deliver the final trigger decision. The TORTA generate a

$$\text{T1} \;=\; (\text{TC1 } \textbf{OR} \text{ TD1}) \textbf{ AND } (\textbf{NOT} \text{ Bhabha veto})$$

distributes it to the Trigger Distributor TD and to the Trigger Supervisor TS within $\sim$ 200 ns from the generation of the event. The TS disables the trigger for a fixed dead time $\sim$ 2.6 μs. The TD performs a 50 ps synchronization of the T1 with the machine RF and then distributes the T1 to the calorimeter FEE. The TORTA generates a second level trigger

$$\text{T2Y} \;=\; (\text{TC2 } \textbf{OR} \text{ TD2}) \textbf{ AND } \text{T1} \textbf{ AND } (\textbf{NOT} \text{ Cosmic-rays flag})$$

within 1.5 μs from the T1 signal. The TS at the end of the dead time controls if the T2Y is active, in this case it asserts a T2 exactly 2 μs after the T1 and distributes it.

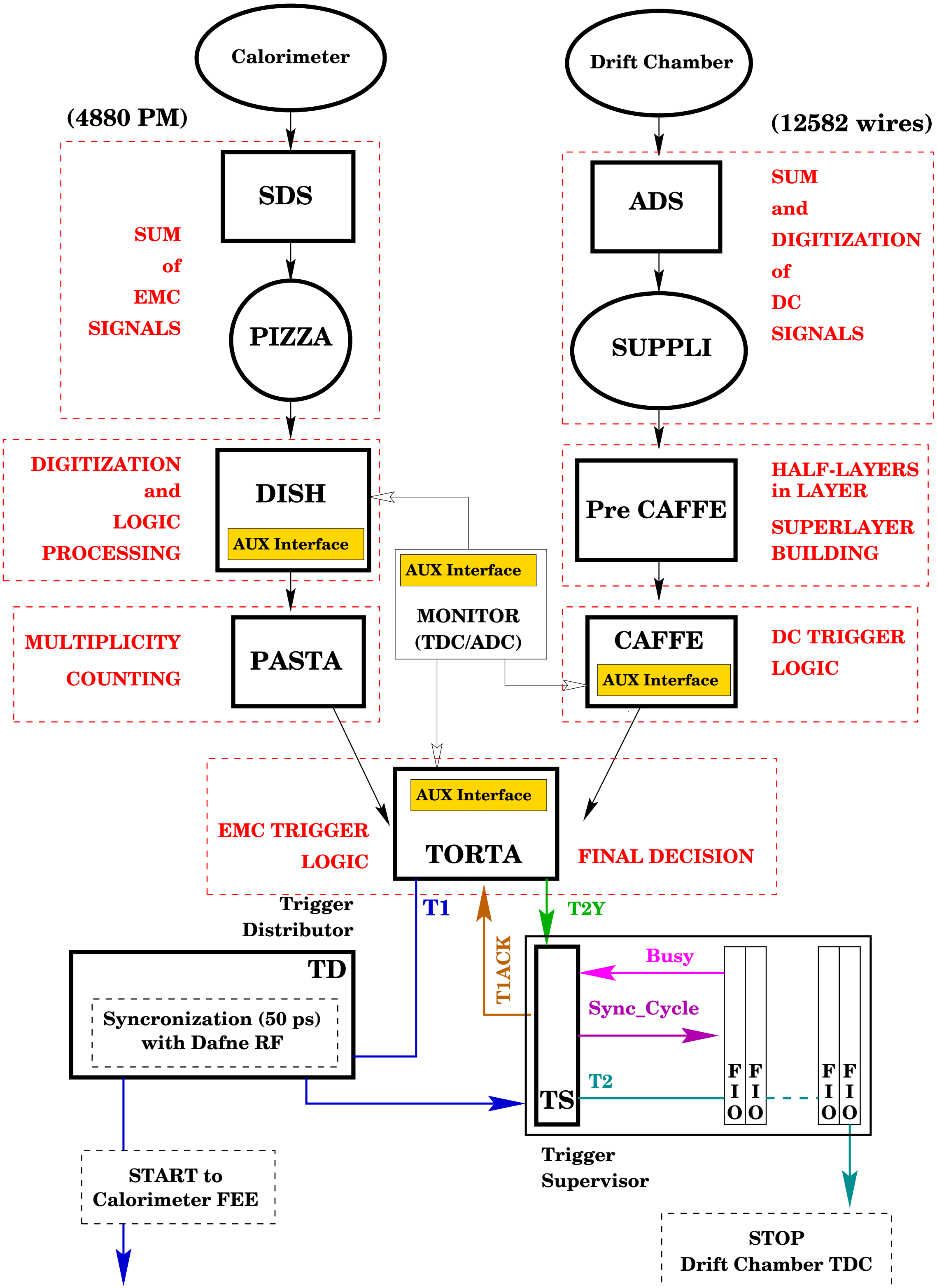

Figure 2.29: Trigger scheme.

Chapter 3

The Events Classification Procedure

3.1 KLOE data taking

In 1999 KLOE has started its data acquisition at DAΦNE . The period from 1999 to 2000 was needed to optimize the collider performance. During the following year the peak luminosity reached the values of $\sim 5 \cdot 10^{31} cm^{-2} s^{-1}$ in 2001 and $\sim 8 \cdot 10^{31} cm^{-2} s^{-1}$ in 2002. As a result, the integrated luminosity has been continuously increasing during last years, as can be seen from table 3.1, allowing to collect a total of $\sim 2500 pb^{-1}$. The plot in figure 3.1 represents the increase in integrated luminosity during the year as a function of time.
Also the background conditions have been steadily improving during 2002 (by even more than a factor 4 with respect to the end of 2001). Further improvements in the luminosity has been obtained during the 2004 and 2005 data taking and a peak luminosity of $\sim 1.4 \cdot 10^{32} cm^{-2} s^{-1}$ has been reached.

Year	Integrated Luminosity $[pb^{-1}]$
1999	4
2000	20
2001	170
2002	300
2004	800
2005	1250

Table 3.1: Integrated luminosity during years 1999-2002 of KLOE data taking.

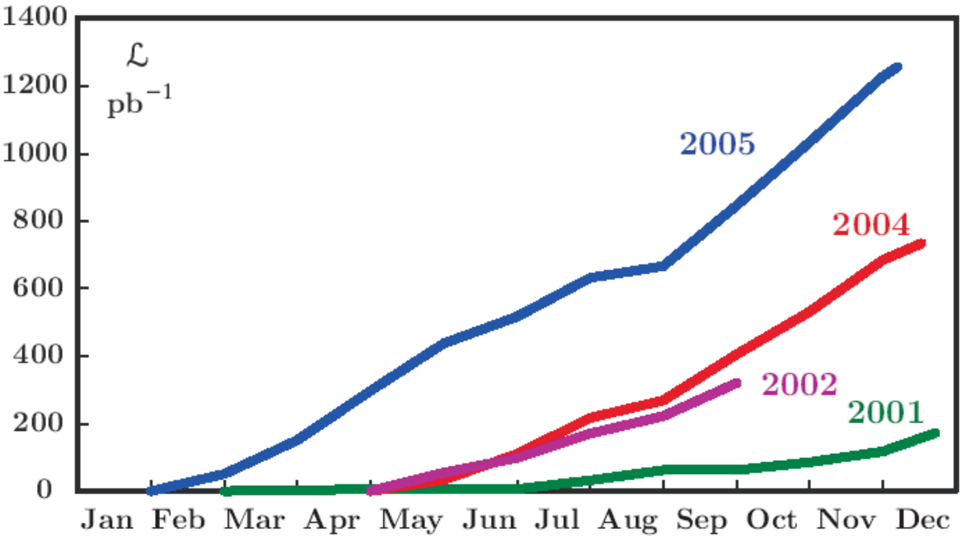

Figure 3.1: Integrated luminosity in pb^{-1} as function of the number of days of data taking from the 2000 until the 2005.

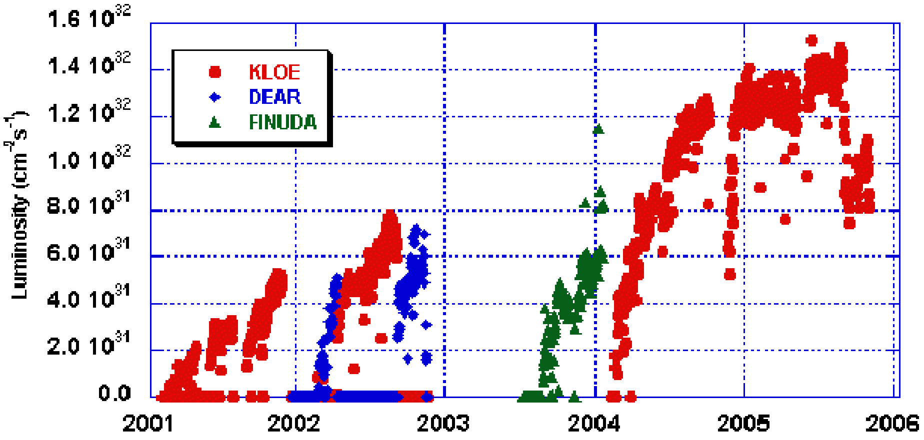

Figure 3.2: Luminosity peak in pb^{-1} as function of the number of days of data taking from the 2000 until the 2005.

3.2 Data reconstruction

The reconstruction of raw data, which are written to mass storage by the DAQ system, starts with the translation, performed through the detector maps, of electronic addresses into geographical detector addresses: time and position of the DC hits and time, position and released energy of the EMC cells. These quantities are then processed in order to reconstruct the physical quantities of the events.

3.2.1 Clustering

The reconstruction of the event begins from the calorimeter information. Groups of adjacent or close cells are merged together to build clusters by the clustering algorithm. The cells are included in the cluster search only if times and amplitudes are available from both sides of the fibers. If a cell is missing just one of time and amplitude signals, it is named "incomplete" cell. For the barrel, an "incomplete" cell is recovered on the basis of the difference $\Delta\phi$ between its azimuth and that of the closest cluster. Incomplete cells are assigned to the cluster if $|\Delta\phi| < 3^\circ$. A similar procedure is used for the end-caps using the transverse coordinate x. The cluster energy E_{cl}, is the sum of the energies of all the cells assigned to it. The cluster position $(x_{cl},\ y_{cl},\ z_{cl})$, and the cluster time t_{cl}, are computed as energy-weighted averages of the cell variables:

$$x_{cl} = \frac{\sum_{cells} E_i x_i}{\sum_{cells} E_i}, \quad y_{cl} = \frac{\sum_{cells} E_i y_i}{\sum_{cells} E_i}, \quad z_{cl} = \frac{\sum_{cells} E_i z_i}{\sum_{cells} E_i}, \quad t_{cl} = \frac{\sum_{cells} E_i t_i}{\sum_{cells} E_i}.$$

The coordinate along the direction of the fibers is computed using the times at both sides, while the two orthogonal coordinates are taken from the nominal position of the cells.

A significant systematic effect induced by the clustering is the production of spurious clusters from the splitting of a unique energy deposit in the calorimeter. This effect is strongly dependent on the energy of the particle releasing its energy and on the position of the cluster in the EMC and affects the photon multiplicity observed by the detector in a given event. For this reason it has been studied on well-define photons samples such as those produced in $e^+e^- \to e^+e^-\gamma$ events and in ϕ radiative decays. The probability of having a cluster splitting is computed as a function of cluster energy and polar angle, and is finally used to unfold the true multiplicities from the observed ones.

After cluster reconstruction, an estimate of the reference time of the event (the absolute $T0$) is given by assuming that the first cluster in time is due to a prompt photon coming from the origin; this photon must have at least 50 MeV and must lie farther than 60 cm from the collision axis. The hypothesis of the being a prompt cluster reasonably fits a large set of events (radiative ϕ decays, $K_S^0 K_L^0$ with at least a γ or a π^0 produced, $e^+e^- \to e^+e^-\gamma$), but is inadequate to describe K^+K^- events: in the charged kaon case, after event classification, a new estimation of the $T0$ must be done (see section 3.4). Once that the absolute $T0$ is determined, it is taken as reference for all the times of the event.

3.2.2 Tracking

The tracking and vertexing procedure [64, 65] are based on the algorithms developed for the ARGUS drift chamber [66], and are modified to take into account the stereo geometry of the KLOE drift chamber and to optimize the vertex-finding efficiency over all the detecting volume.
The chamber operates with a helium-based gas mixture to minimize the tracks multiple scattering. Due to the large cell dimensions the drift velocity is not saturated and the cell response is not linear. Specific sets of space to time relations (s-t relations), which allow to reconstruct the distance of closest approach of the particle to the sense wire, are computed as function of the drift time. Due to the square shape of the drift cell and to the deformations induced on it by the stereo geometry, the s-t relations depend on the spatial coordinates of the cell and on the incidence direction of the track in the cell. This dependence has been parametrized according to two variables (defined as shown in figure 3.3): the track incidence angle $\tilde{\phi}$ and the shape parameter β, which takes into account the peculiar geometry of the upper part of the cell. It has been seen [67] that 232 parameterizations accounting for cell type (small or big), track orientation, and cell shape, are a reasonable compromise which allows a good description of the s-t relations and a limited number of parameterizations. The s-t relations are parametrized in terms of a 5^{th} order Chebychev polynomial, $d(C_k, t - T_0)$, and the C_k are 6 × 232 coefficients. Several examples of these curves as functions of the shape parameter β and of the incidence angle $\tilde{\phi}$, are illustrated in figures 3.4 and 3.5.
The track reconstruction procedure starts with the **pattern recognition**. The pattern recognition gives also a first estimate of the track parameters. Owing to the stereo geometry of the drift chamber, the hits are distributed on 2 nearby curves when projected onto the $x - y$ plane. One of these curve is made up by the hits which fire wires with

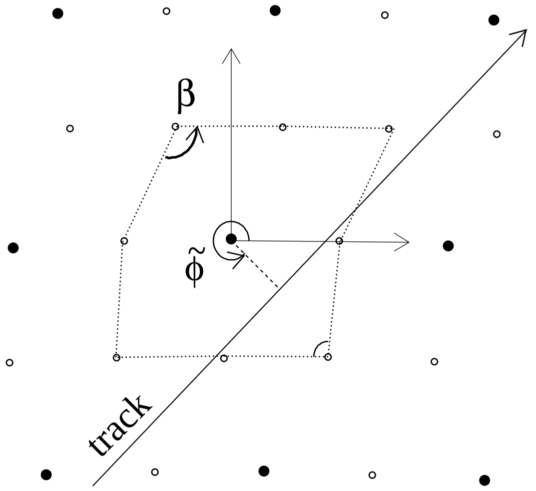

Figure 3.3: Definitions of the variables used in the s-t relations classification.

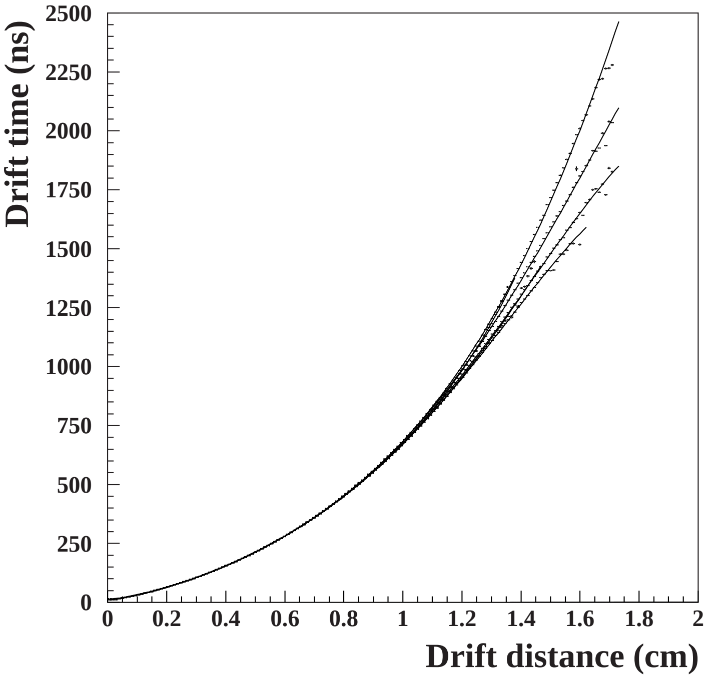

Figure 3.4: Space-time relations for different values of the shape parameter β.

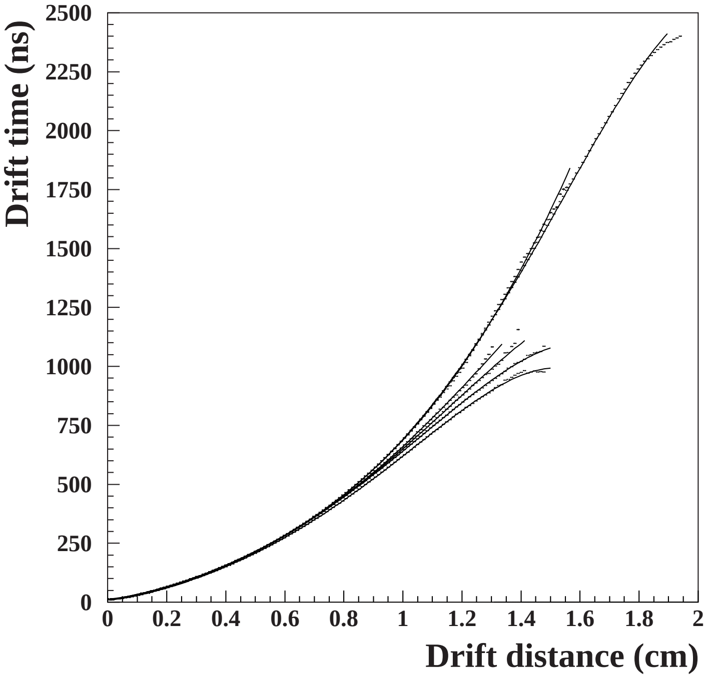

Figure 3.5: Space-time relations for different values of the incidence angle $\tilde{\phi}$.

the positive stereo angle and the other one by the hits of wires with negative angle. The pattern recognition first combines the hits on each view separately. The 2D candidates are then matched and merged to define the final track candidate. In merging the two views the z information is also extracted and an evaluation of the parameters describing the trajectory is made.

The **track fit** is a least-square fit of the track candidates whose initial parameters are taken from the pattern recognition results. The ultimate goal is to give the best estimation of the particle momenta and positions. The fit yields the parameters $\overrightarrow{q}$ which minimize the quadratic form:

$$\chi^2 = [\overrightarrow{d}_{meas} - \overrightarrow{d}_{\overrightarrow{q}}]^T W [\overrightarrow{d}_{meas} - \overrightarrow{d}_{\overrightarrow{q}}]$$

where $\overrightarrow{d}_{meas}$ are the measured drift distances, $\overrightarrow{d}_{\overrightarrow{q}}$ are the distances of the closest approach of the track to each wire and W is the inverse covariance matrix of the measured coordinates. The minimization is performed using an iterative procedure in which the track model is locally linearized.

Energy loss and multiple scattering suffered by particles in crossing the drift chamber are also taken in account. The track fit procedure also contains some additional features designed to increase the performance of the hit assignments using the parameters available at the track fit level, which are more refined than those available at pattern recognition level. These are:

- **Hit addition**: an ansatz is made to add hits that were not associated to any track candidate by the pattern recognition. Each hit is added or not on the basis of its contribution to the χ^2.
- **Hit rejection**: hits associated to tracks by the pattern recognition may be removed if their contribution to the χ^2 is too large.
- **Track joining**: tries to merge two candidate tracks which could have been produced by the same particle and split by the pattern recognition.
- **Track splitting**: it operates in the opposite way if the track joining, it tries to split single tracks corresponding to two different physical signals.

3.2.3 Vertexing

After reconstructing tracks, the vertex fit [65] aims to reconstruct the positions of the decay vertexes in the DC volume.

In order to reconstruct the ϕ decay vertex tracks are extrapolated toward the nominal interaction point, taking into account the energy losses on the DC inner walls. For the other vertexes an iterative procedure is used to obtain the point of closest approach for all tracks. Pairs of tracks are searched, whose trajectories show an acceptable crossing point, both in the $x - y$ plane and along the z coordinate. A χ^2 minimization is applied in order to obtain the best possible estimate of the vertex position, and if such

procedure converges, the vertex is kept.
Vertexes are classified according to the quality of the fit. At this level, even more than one vertex can belong to a given track. A merging procedure is performed to join 2-tracks vertexes together, so obtaining vertexes with 3 or more tracks (this is particularly relevant for the $K^{\pm} \to \pi^{\pm}\pi^{+}\pi^{-}$ decay). An hypothesis test which compares the 4-tracks verteces versus the 2-tracks verteces is done. On the bases of the χ^2 the two hypotheses are taped.

Kink identification

The pattern recognition algorithm has a very high efficiency ($\sim$ 90%) in finding candidates for a given physical track. Monte Carlo simulations, however, show that these candidates are not always composed of hits deposited by just one physical track. This problem may be parametrized by a quantity called the "*purity*" of the track, defined as the ratio:

$$\text{Purity} = \frac{\text{Number of hits of the main contributor}}{\text{Total number of hits}}$$

Track candidates which have purities less than one may be present in a widespread range of topologies. A **kink identification** procedure that allows the recovery of two main topologies, the "$\pi\mu$ kink" topology and the so-called the "eaten vertex" topology (see figure 3.7), has been developed.

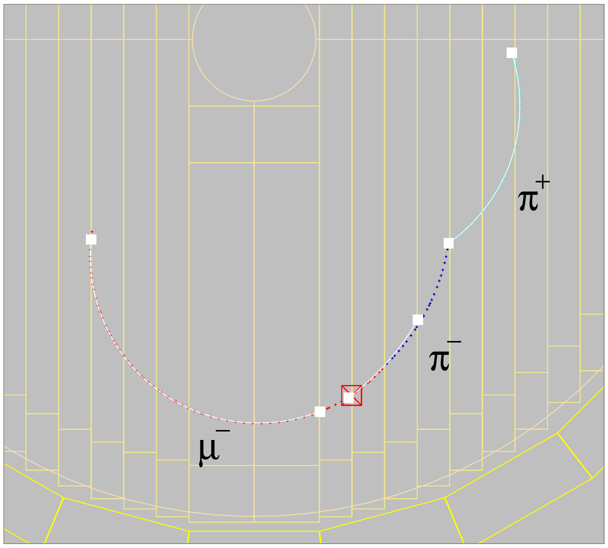

Figure 3.6: Example of "$\pi\mu$ kink" topology: a π^- (dark blue dots) coming from a $K_L \to \pi^+\pi^-$ decays in a μ^- (red dots) and antineutrino. The pattern recognition forms a candidate track with π^- and μ^-. The bad quality of the fitted track leads to miss the K_L vertex.

In the following, both of these topologies will be referred to as kinks. These two topologies correspond to very different physical situations but are very similar from

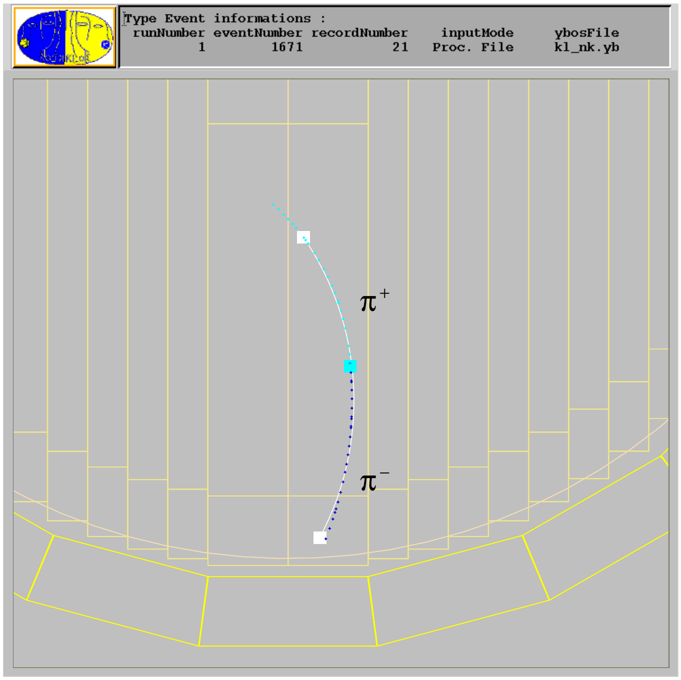

```
Type Event informations :
 runNumber eventNumber recordNumber    inputMode      ybosFile
         1        1671           21   Proc. File      kl_nk.yb
```

Figure 3.7: Example of the eaten vertex topology: only one track is made out of the π^+ and π^- coming from the K_L decay.

the point of view of the track candidate: in both cases, the candidate is made up of two main helix stumps with different curvatures joined into one single helix segment. The occurrence of the eaten vertex topology may affect the decay vertex reconstruction efficiency as well as its spatial resolution. The occurrence of the $\pi\mu$ kink topology is dangerous for K_L, K_S and $K^\pm \to \pi^\pm\pi^0$ decay vertex reconstruction, as it worsens the momentum estimate for the charged pions.
The procedure that allows the identification and recovery of the kink consists of three main steps:

1. the "kink-like" track is identified and the possible position of the kink is estimated (first level algorithm);

2. the original ("mother") track and its "daughters" are fitted;

3. finally the χ^2 of the mother and daughter tracks are compared to decide which of them should be kept and which should be dropped (second level algorithm).

The basic idea is to study the distribution of the residuals of the fit (i.e. of the quantity $d_{meas} - d_{fit}$) along the track. This distribution looks very different for mixed tracks and for pure ones, as may be observed in figure 3.8. In fact there is a sharp minimum at the kink position, while pure tracks have a nearby flat residual distribution. The goal is to identify the V shape and to split the track at the minimum creating two new

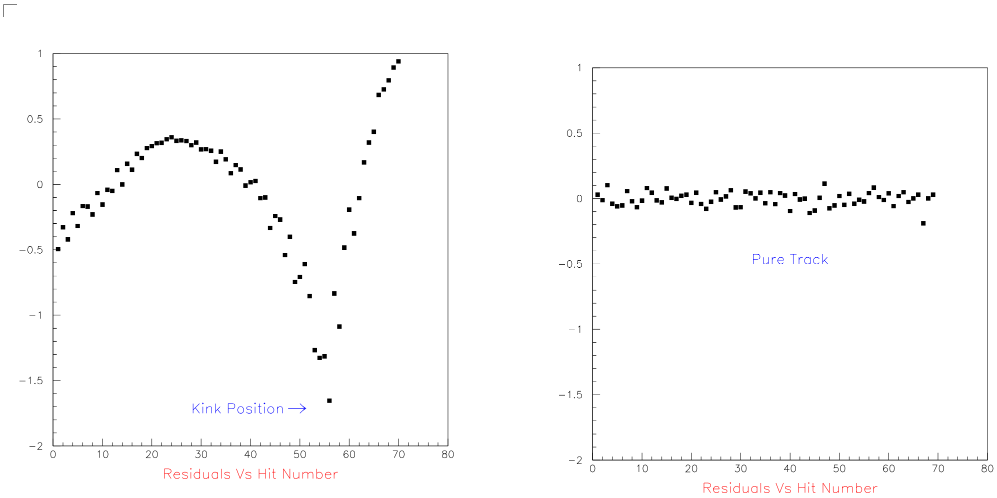

Figure 3.8: The residual proceeding as function of the hit position for a $\pi\mu$ kink (left) and a pure track (right).

track candidates (*daughters*) to fit. Great care must be taken in order not to split pure tracks, which would result in a large number of fake tracks and vertexes.

3.3 Description of the Event Classification Algorithms

The offline analysis could require a very long time which can be reduced by an automatic procedure producing the *segment* and *object* banks online. This procedure is the *reconstruction chain* (see fig.3.9).

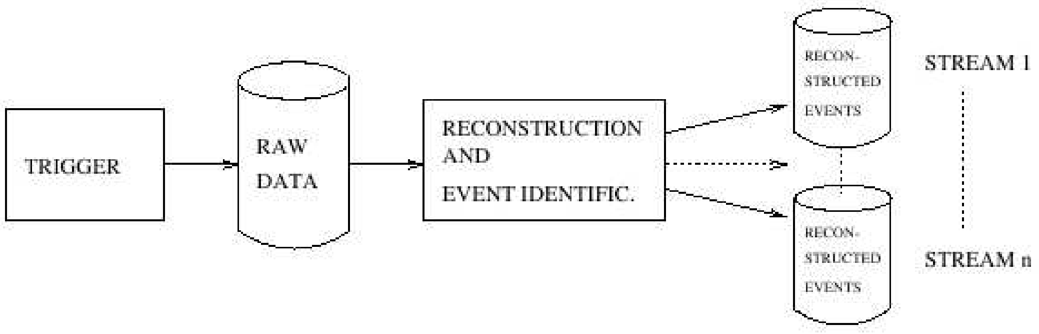

Figure 3.9: The online data taking process, comsisting of DAQ and reconstruction chain.

The Event Classificaction program has to satisfy the following requirements:

- Unbiased event classification, necessary to minimize systematics effects.
- High identification efficiency, *i.e.* small losses of good events. For example a very high identification efficiency at the $K_S \to \pi^+\pi^-$ channel is necessary to keep the statistical error on $\Re\left(\frac{\varepsilon'}{\varepsilon}\right)$ at 10^{-4} level.
- Low contamination, *i.e.* pure sample.
- Preliminary events classification into different *streams*, which is a collection of events which are all identified by one definite algorithm.

A trigger mask is used to classify these informations: a n-bits long word is associated to every processed event, each bit corresponding to a particular requirement on the event. The main streams defined in the event classification are (Fig. 3.10):

- $\phi \to K^+K^-$ (KPM);
- $\phi \to K_S^0 K_L^0$ (KLS);
- $\phi \to \rho\pi, \pi^+\pi^-\pi^0$ (RPI);
- ϕ radiative decays (RAD);
- Bhabha and cosmic events useful for detector calibration (CLB). Also $e^+e^- \to \mu^+\mu^-$ and $e^+e^- \to \pi^+\pi^-$ events are collected within this sample;
- All events not identified by any of the EvCl algorithms (UFO);
- Bhabha scattering.

The background-rejection algorithm (FILFO) is based on calorimeter clustering and DC hit counting, so that background events can be eliminated before DC reconstruction, which is the most CPU-intensive section of our reconstruction program. The main FILFO features are the downscaling of Bhabha and cosmic events, and machine background rejection.

For the identification of background events, cuts are applied on the number of clusters; the number of DC hits; the total energy in the calorimeter; the average polar angle, position, and depth of the (two) most energetic cluster(s); and the ratio between the number of hits in the innermost DC layers and the total number of DC hits. These cuts have been studied to minimize losses for physics channels. Additionally, a simple cut on anomalously large energy deposits in any calorimeter region is included to reject rare machine background topologies due to sporadic beam-loss events.

Events surviving the rejection filters and reconstructed by means of drift chamber information are finally classified into distinct categories (data streams) by the event-selection algorithms, according to the different hypotheses for the final state. Selection

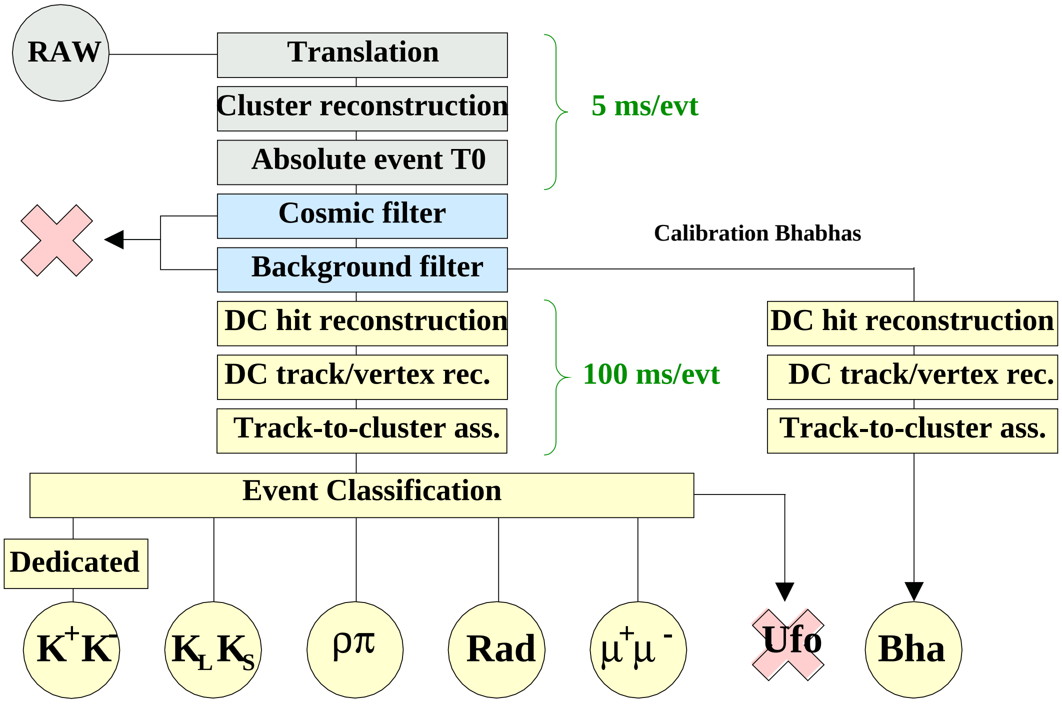

Figure 3.10: Logic scheme of the KLOE offline reconstruction.

algorithms must correctly separate the various Φ decay channels with the highest possible efficiency and minimize the contaminations from the other streams. In order to avoid correlations, the same event can be tagged by more than one algorithm and saved in different data streams. Moreover, biases are avoided by adopting rather loose and simple selection criteria. This also allows to reduce the CPU time needed for the event classification to a very small fraction with respect to the complete data reconstruction chain.

3.3.1 The KPM stream selection algorithms

$\phi \rightarrow K^+K^-$ constitutes the most frequent decay mode of the ϕ meson, since the branching ratio for this channel is 49.2% [50]. In the ϕ rest frame, the two charged kaons have opposite momenta of 127 MeV , but due to the beam crossing angle the ϕ is produced with a momentum of $\sim$ 13 MeV. Then in the laboratory frame the kaon momentum ranges between $\sim$ 120 $MeV$and 135 MeV (see table 2.4).
The average value of the radius of curvature in the KLOE magnetic field ($\sim 0.52\ T$) for charged kaons having $p_z = 0$ is 81 cm; considering also the z component of its momentum, it turns out that a charged kaon has to travel in average $\sim$ 35 cm from the interaction point before reaching the drift chamber volume. Given their velocity $\beta \simeq 0.25$ and their mean life $\tau = 1.2384 \cdot 10^{-8} s$ [50], charged kaons have decay length $\beta\gamma c\tau \simeq 95\ cm$, so that the probability for charged kaons to reach the DC volume

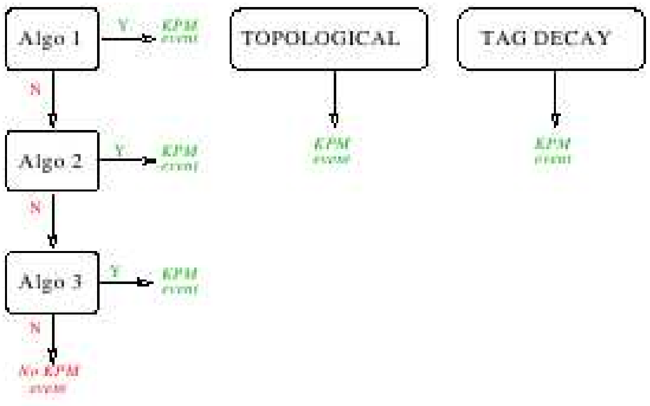

Figure 3.11: Events classification logic scheme.

and release a sufficient number of hits to determine a reconstructible track does not exceed 70%. Moreover, a particle coming from the interaction region, before entering the chamber, has to pass through the beam pipe, (see section 2.2.1) and through the drift chamber inner wall (see section 2.2.2), loosing on average 25 MeV, with a corresponding shortening of the decay length to about 75 cm.

Five selection algorithms have been developed for the identification of $\phi \to K^+K^-$ events and they constitute the official procedure of the Event Classification program for the KPM stream.
At the beginning of the data taking, during the machine tuning, till year 2000, only the first three algorithms were applied. Later two more algorithms more efficient and with higher cleaning capability have been developed.

1. *Algo1*, based on the existence of a candidate $\phi \to K^+K^-$ vertex in the interaction region.
2. *Algo2*, looking for events with both K^+ and K^- tracks reconstructed without the ϕ vertex.
3. *Algo3*, trying to identify a charged kaon by requiring specific cuts on a single fitted track.
4. *TOPO*, exploiting the typical geometrical configuration of a K^+K^- event.
5. *TAG*, founded on the kinematic reconstruction and identification of a tagging $K^\pm$ two-body decay.

The first three algorithms are applied in cascade, according to the diagram shown in 3.12. Even if they have been replaced by the two newest algorithms we report them here for completeness purposes. Each algorithm analyzes the events by means of

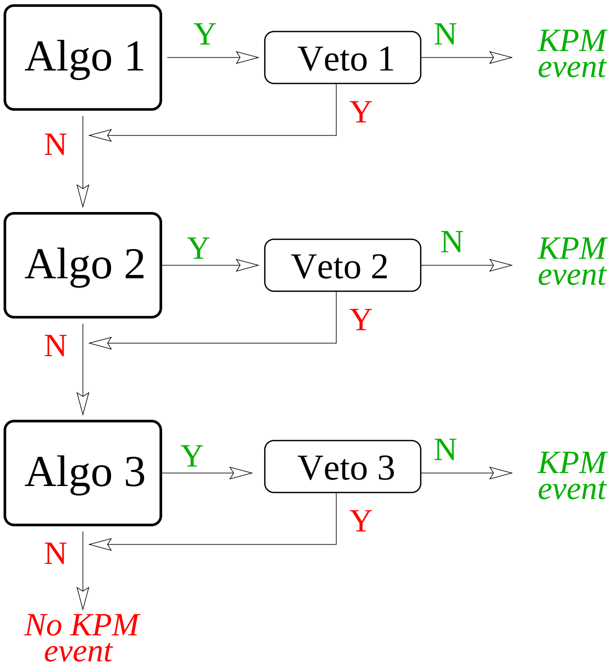

Figure 3.12: Logic scheme applied for the Algo1, Algo2 and Algo3 algorithms in the Event Classification program.

suitable selection criteria and a corresponding veto tests them against the background hypothesis: if such conditions are fulfilled, the events are definitively kept and no further requirements are imposed, otherwise the events are left to the analysis of the next algorithm(s). The definitions of the selection criteria applied in the first three algorithms are given in the following.

Algo1

In the **Algo1** procedure vertexes with 2 tracks and total zero charge are required in the fiducial volume defined by:

- $r_V = \sqrt{x_V^2 + y_V^2} < 50\ cm$;
- $|z_V| < 40\ cm$;

in addition, the two tracks momenta $\overrightarrow{p}_1$ and $\overrightarrow{p}_2$ must be such that:

- $180 < |\overrightarrow{p}_1| + |\overrightarrow{p}_2| < 235\ MeV$;
- $-20 < \overrightarrow{p}_{1x} + \overrightarrow{p}_{2x} < 40\ MeV$;
- $|\overrightarrow{p}_{1y} + \overrightarrow{p}_{2y}| < 30\ MeV$;

- $|\overrightarrow{p}_{1z} + \overrightarrow{p}_{2z}| < 20\ MeV$.

Veto1 reject events for which any of the following requirement is satisfied.
Veto logic: (**1**.and.**2**).or.**3**.or.**4**:

1. $\theta_{K^+} < 0.60\ rad$ (track produced at small polar angle);
2. $\theta_{K^-} < 0.60\ rad$ (track produced at small polar angle);
3. $|r_{1PCA} + r_{2PCA}| \geq 16\ cm$ where $r_{iPCA} = \sqrt{x^2_{iPCA} + y^2_{1PCA}}$;
4. $|z_{1PCA} + z_{2PCA}| \geq 16\ cm$;

and where x_{iPCA}, y_{iPCA}, z_{iPCA} and are coordinates of the Point of Closest Approach of the kaon track to the IP.

Algo2

The **Algo2** procedure asks for two tracks whose innermost (outermost) DC layer hit is < 20 (< 35), corresponding to 72.5 cm (117.5 cm) in the $x - y$ plane. The distance between the last hits of the two tracks has to be at least 88 cm, the distance between the centers of the two helicoidal trajectories in the $x - y$ plane has not to exceed 25 cm. Subsequently, the following cuts are required:

- $70 < |\overrightarrow{p}_1| < 170\ MeV$;
- $|z_{1PCA}| < 70\ cm$;
- $|r_{1PCA}| < 15\ cm$;
- $50 < |\overrightarrow{p}_2| < 200\ MeV$;
- $|z_{2PCA}| < 100\ cm$;
- $|r_{2PCA}| < 25\ cm$;
- $145 < |\overrightarrow{p}_1 + \overrightarrow{p}_2| < 260\ MeV$;
- $|z_{1PCA} - z_{2PCA}| < 100\ cm$;
- $|r_{1PCA} + r_{2PCA}| < 16\ cm$.

The definition of **Veto2** coincides with Veto1.

Algo3

In the **Algo3** procedure a single track is searched with innermost (outermost) DC layer hit < 10 (< 35), which corresponds to 48.5 cm (117.5 cm) in the $x - y$plane. Subsequently, the following cuts are required:

- track length < 150 cm;
- $85 < |\overrightarrow{p}| < 120\ MeV$;
- $r_{PCA} < 10\ cm$;
- $|z_{PCA}| < 20\ cm$.

In order **Veto3** to be satisfied, at least one of the logical conditions is required.
Veto logic: **1**.or.**2**.or.**3**.or.**4**:

1. $|z_{PCA}| > 5cm$;
2. $|r_{PCA}| > 5cm$;
3. $|\overrightarrow{p}| < 80\ MeV$;
4. $|\theta K| < 0.7\ rad$.

The efficiency of the Algo1-Algo2-Algo3 cascade has been evaluated on Monte Carlo and is about 26%.

A very high background rate in the KPM stream and a strong correlation in efficiency and systematic evaluation has been observed, since the starting of the KLOE data taking in 1999, when only these three algorithms were implemented in the Event Classification program. A typical background was due to pion photoproduction on the beam-pipe, see figure 3.13 and figure 3.14
Thus two more algorithms called **TOPO** and **TAG** have been developed in order to reduce the presence of background in the finally streamed data sample and to provide an estimate of the systematics induced by the first three algorithms. Their definitions are given below.

The old selection (the Algo-cascade) and the new algorithms have been "OR-ed" for 2001 and 2002 data.

The Topological algorithm

The TOPO algorithm initially requires two tracks of opposite charge in the event which satisfy the following selection cuts:

- $|z_{PCA}| < 15cm$;
- $|r_{PCA}| < 15cm$;
- $70 < |\overrightarrow{p}_{PCA}| < 130\ MeV$;
- last hit in a fiducial volume obtained by rotating around the beam axis the isosceles trapezium having parallel sides, 250 cm and 270 cm long, whose distances from the z axis are 40 cm and 150 cm respectively.

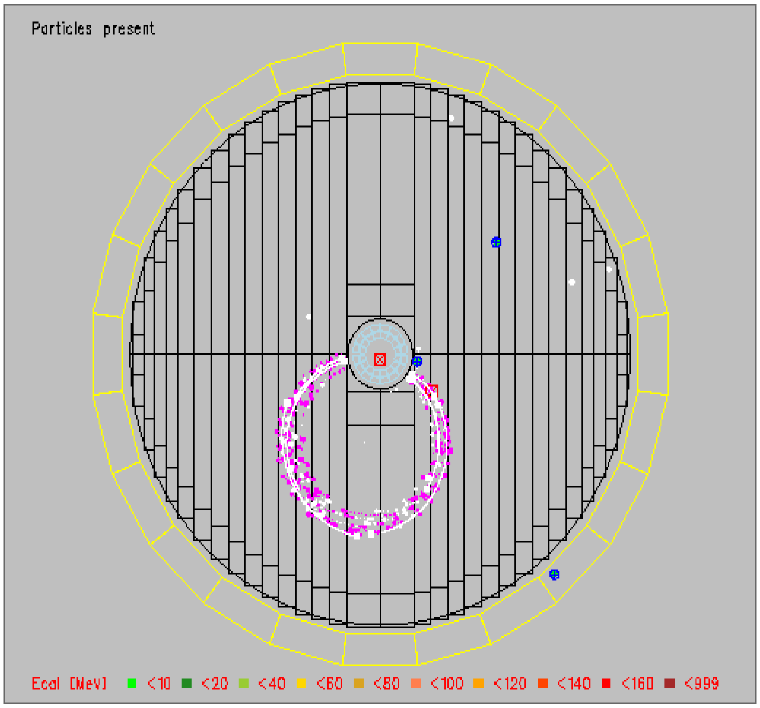

Figure 3.13: Reconstruction of a pion photoproduction event.

The angle ϕ_{em} between the emission line of the two kaons and the horizontal axis is then considered. The two momenta $\overrightarrow{p}_1$ and $\overrightarrow{p}_2$ have to satisfy these two conditions simultaneously:

- $(176 < |\overrightarrow{p}_1| + |\overrightarrow{p}_2| < 220\ MeV)$ .OR. $(||\overrightarrow{p}_1| - |\overrightarrow{p}_2|| > 8\ MeV)$;
- $||\overrightarrow{p}_1| - |\overrightarrow{p}_2|| > 25 \cdot (cos(\phi_{em}) - 0.6)$.

While the first condition exploits the correlation between the momenta of the two candidate tracks, the second condition uses the information of the boost of the ϕ meson.
The efficiency of the TOPO algorithm has been evaluated on Monte Carlo and is about 9%.

The TAG algorithm

At a $\Phi - factory$, it is possible to take advantage of the fact that the Kaons are produced in pairs, so the detection of one Kaon assure the presence of the other Kaon with well defined momentum and direction. Each one of the well spatially separeted region defined by the $K^{\pm}$ pair, is called hemisphere.
In the following we use a coordinate system with the z-axis defined as the bisectrix of the beams, the y-axis vertical and the x-axis toward the center of the collider rings.
The TAG algorithm identifies the two-body decays $K \rightarrow \mu\nu$ or $K \rightarrow \pi\pi^0$, which are

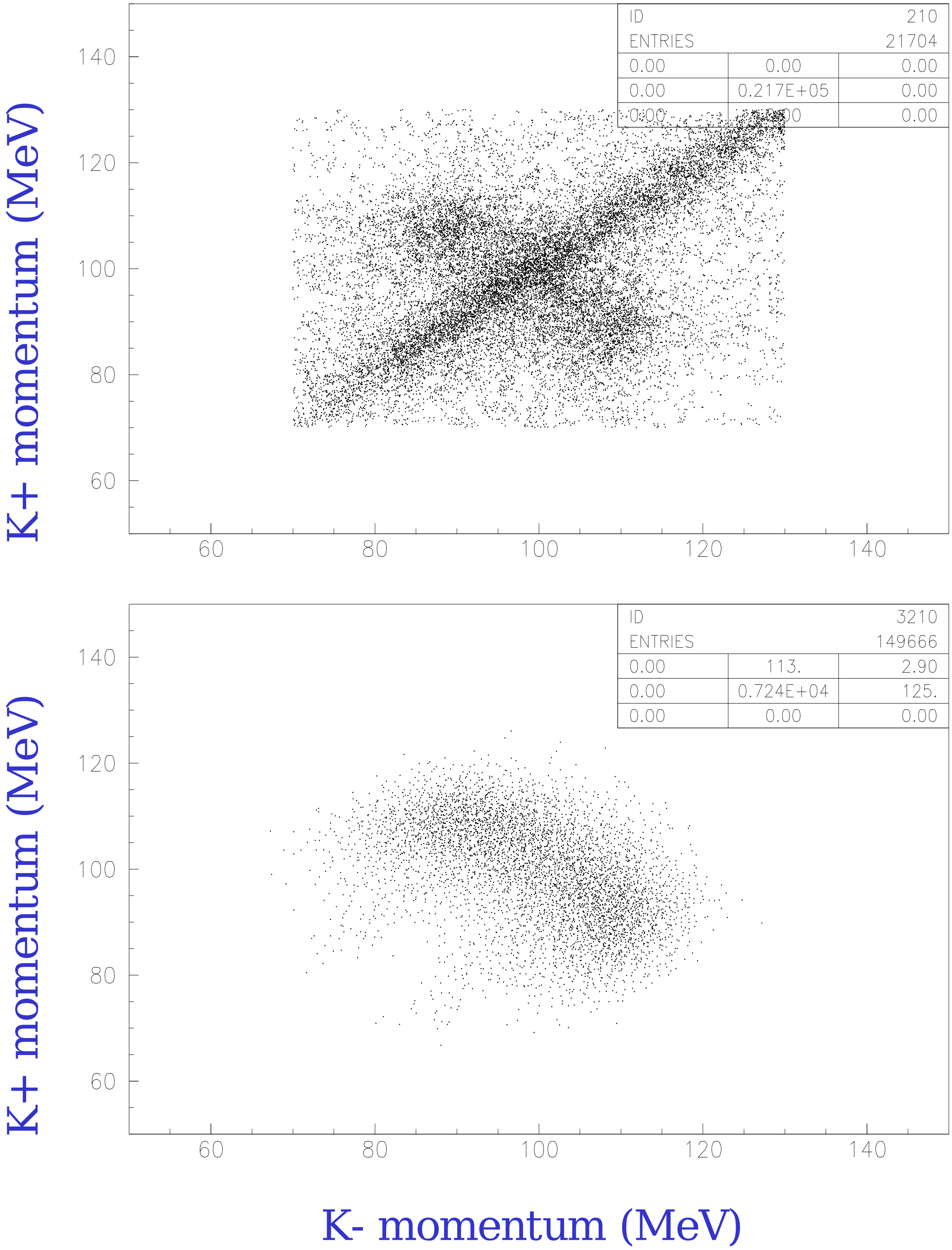

Figure 3.14: Momentum of K^+ versus the momentum of K^- for data (above) and Monte Carlo simulation (below). It possible to see a large amount of background due to pions photoproduced on the beam-pipe, which are characterized by the linear relation between the momenta of the two "kaon" candidate.

about 85% of charged Kaon decays, and it is based on the presence of a two-tracks vertex in the DC which signals the $K^{\pm}$ decay. The requirements that a track (Kaon candidate) must fulfil in order to be identified as a Kaon track are the following:

- distance of the point of closest approach to the IP, in the xy plane, $r_{xy} \leq 10\ cm$.
- distance of the point of closest approach to the IP, along z, $r_z \leq 20\ cm$.
- radial distance between the Kaon candidate decay vertex and the beam axis, $40 < R_V < 150\ cm$.
- first hit momentum, $70 \leq \overrightarrow{p} \leq 130\ MeV/c$.

Once the Kaon candidate has been identified:

- the candidate track associated to the charged decay particle (secondary) must have the same charge of the Kaon.
- the momentum difference between the Kaon and the secondary track $\Delta_p = |\overrightarrow{p}_K| - |\overrightarrow{p}_{sec}|$ must fulfil $-320 < \Delta_p < -120\ Mev/c$.
- the charged decay particle momentum in the Kaon rest frame, p^*, using the $\pi^{\pm}$ mass hypothesis, must be in the range $180 < p^* < 270\ MeV/c$.

Then the following cuts are applied to distinguish between K_μ and $K_{\pi\pi^0}$:

$$225 < p^* < 245\ Mev/c \qquad (\mathrm{tag-type\ K}_{\mu\nu}) \tag{3.1}$$

$$225 < p^* < 245\ Mev/c \qquad (\mathrm{tag-type\ K}_{\pi\pi^0}) \tag{3.2}$$

3.4 Retracking, merging and absolute timing

The KLOE reconstruction has been conceived to track neutral kaon decays. The tracking procedure is performed in the pion mass hypothesis. Therefore the reconstruction is not optimized for charged kaon tracks (see figures (3.15) and (3.16)). It was mandatory to develop a retracking and merging procedure which takes into account the right mass hypothesis and the dE/dx in the chamber walls.

The retracking is performed taking into account the energy losses crossing the various detector materials or between consecutive hits traveling through the gas in the DC

using the Bethe-Bloch formula under the correct mass hypothesis. It produces improvement of all quantities involved, as can be seen in figures (3.17), (3.18) and (3.19), where are shown respectively the improvements on the kaon momentum resolution, the improvement on the vertex resolution and the number of broken kaon tracks.
Also the reference time $T0$ must be calculated again because the standard KLOE procedure is based on photons coming from the IP (see section (3.2.1)). The correct knowledge of the kaon momentum, obtained by the retracking, allows to re-compute the absolute $T0$ of the event, and consequently to improve the quality of the reconstruction of the whole event. The $T0$ finding is based on vertex position, cluster times, momentum of kaon and charged secondary at vertex for particles involved in the tag hemisphere and is performed tracing back the particles from the calorimeter to the IP, taking into account dE/dx for kaons.
For $\pi\pi^0$ decays it is possible to check neutral versus charged reconstructed decay time. Using double tag events it is possible to extract $T0$ resolution from data ($\mathrm{T0}_+ - \mathrm{T0}_-$). The $T0$ global algorithm has an high efficiency $\sim 96\%$, good resolution $\sigma_{T0} \sim 0.7\ ns$ and it can be monitored from data with double tagged events.

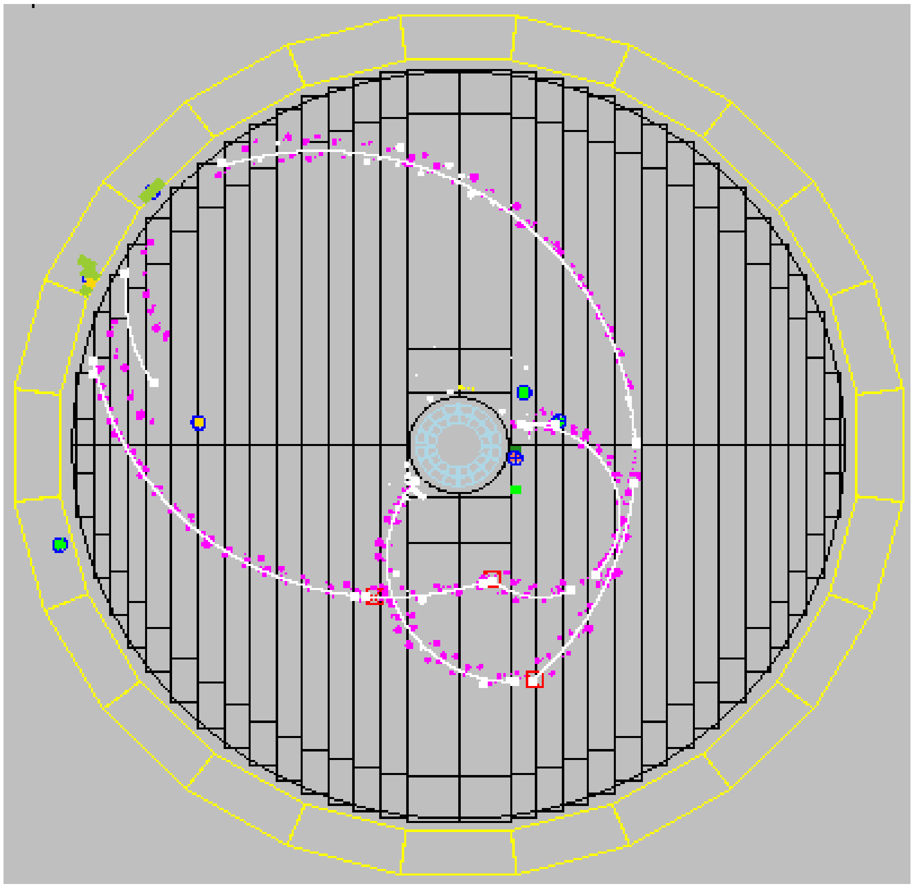

Figure 3.15: Reconstruction, without retracking of a $K^+ \rightarrow \mu^+\nu$, $K^- \rightarrow \mu^-\overline{\nu}$ event. Three fake vertexes have been reconstructed besides the two true vertexes.

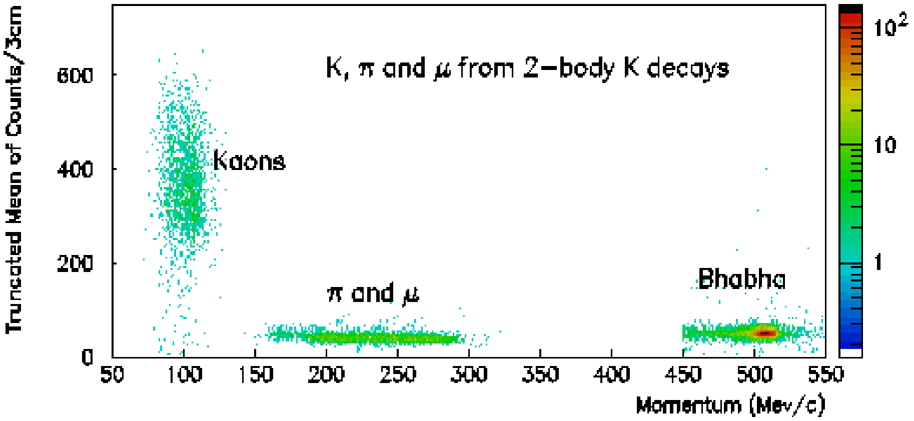

Figure 3.16: Energy released in the big cells versus the momentum of the particle, it is possible to see the big difference of energy released between kaons and their secondaries.

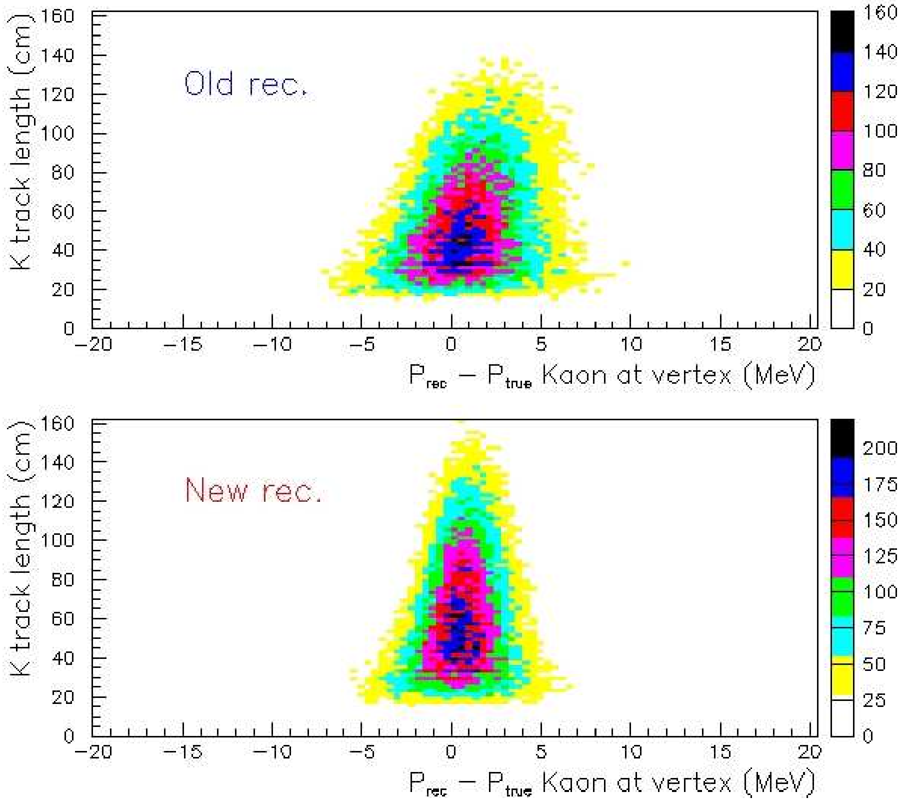

Figure 3.17: Resolution on the kaon momentum before (above) and after (below) retracking.

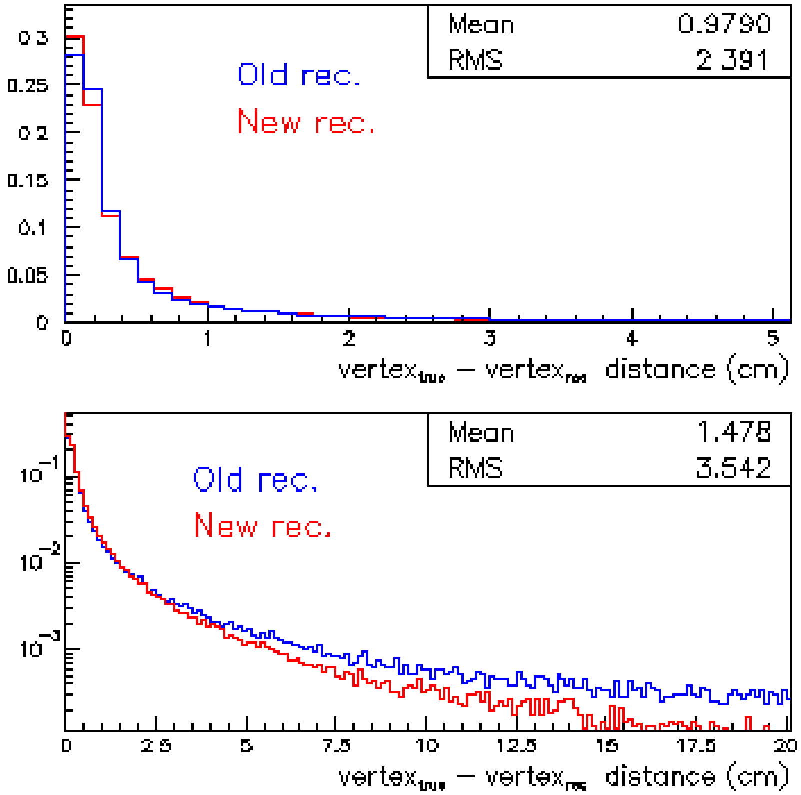

Figure 3.18: Vertex resolution before (above) and after (below) retracking.

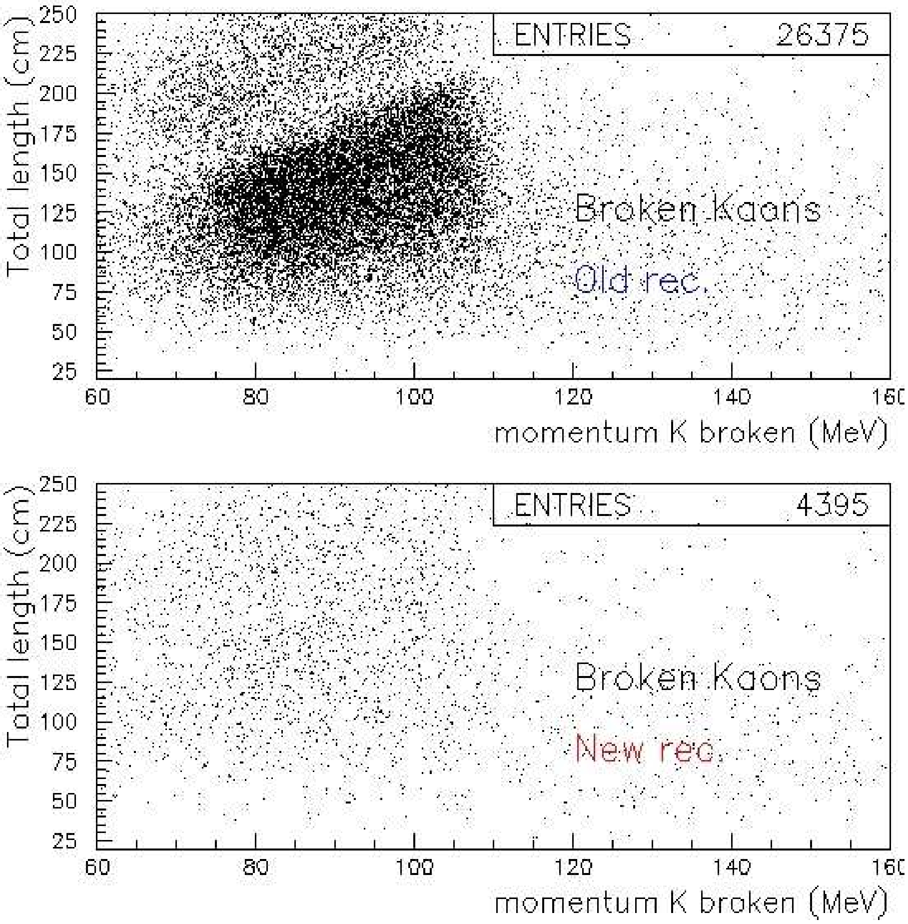

Figure 3.19: Number of broken kaon tracks before (above) and after (below) retracking.

Chapter 4

The signal selection

The aim is to measure the K_{e4}^{00} branching ratio normalized to $K^{00}\pi3$ ($K^{\pm} \rightarrow \pi^{\pm}\pi^{0}\pi^{0}$) decay, given by the partial width ratio:

$$\Gamma(K^{\pm} \rightarrow \pi^{0}\pi^{0}e^{\pm}\nu_{e}(\overline{\nu}_{e}))/\Gamma(K^{\pm} \rightarrow \pi^{\pm}\pi^{0}\pi^{0}) \tag{4.1}$$

The normalization to $K^{00}\pi3$ guarantees a cancellation of most of systematic effects due to the reconstruction (see following equation), given the similarities among the two channel (see figure [**?**]).

$$\frac{BR(K^{\pm} \rightarrow \pi^{0}\pi^{0}e^{\pm}\nu_{e}(\overline{\nu}_{e}))}{BR(K^{\pm} \rightarrow \pi^{0}\pi^{0}\pi^{\pm})} = \frac{N^{Obs}_{K^{00}e4}}{N^{Obs}_{K^{00}\pi3}} \cdot \frac{\epsilon_{K^{00}\pi3}}{\epsilon_{K^{00}e4}} \tag{4.2}$$

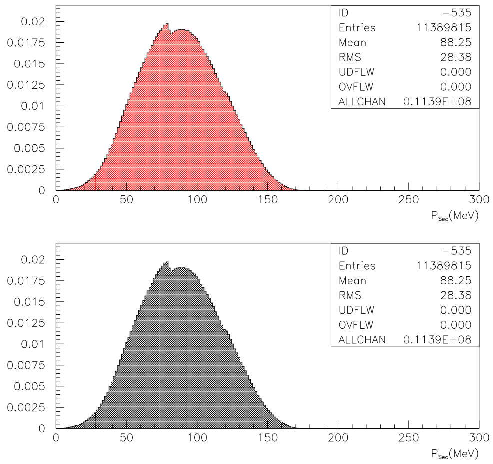

Figure 4.1: Secondary charged 3-momentum for signal (blue) and normalization (red).

The signal selection strategy can be summarized as follows:

1. Starting from the events classification algorithm informations, we require a $\phi \to K^+K^-$ identificated by KPM stream algorithm (section [**?**]).
2. Then we search for a $K^\pm$ track plus vertex in the drift chamber (section 1.1).
3. Events with two π^0 in the final state are selected using the neutral vertex tecnique (section 1.2).
4. We proceed identifying the two decaying photons belonging to the same π^0, the $\gamma\gamma \to \pi^0$ association is performed using a χ^2 technique (section 1.3).
5. We run two kinematic fit procedures, one in signal hypothesis and the second in $K^{00}\pi 3$ hypothesis (section 1.4).
6. We ask for the secondary charged track into the drift chamber to be associated to a cluster into the electromagnetic calorimeter, in order to construct a lot of kinematic variables used to reject background (section 1.5).
7. Background rejection (constitued by residual normalization plus K_{e3} events) by means of a Likelihood Ratio method (section 1.6).

4.1 $K^\pm$ decay vertex reconstruction

Even if the KPM stream algorithm identifies a $K^\pm$ track candidate into the drift chamber, it is necessary to search again for it in order to lower fake $K^\pm$ tracks contamination. Starting from the information that an event has been identified by KPM algorithm, we search into the drift chamber for the Kaon track, which is defined as the track fulfilling the following requests:

- distance of the point of closest approach to the IP, in the xy plane, $r_{xy} \leq 6\ cm$.
- distance of the point of closest approach to the IP, along z, $r_z \leq 5\ cm$.
- first hit momentum, $80 \leq \overrightarrow{p} \leq 120\ MeV/c$.

this track has to be associated with a vertex reconstructed in the chamber, so, since the signal Kaon originate from the interaction point in the $\phi \to K^+K^-$ decay, we have to avoid to consider the ϕ decay, so we define:

$$r_{Vtx} = \sqrt{x^2_{Vtx} + y^2_{Vtx}} \tag{4.3}$$

and impose

$$40 < r_{Vtx} < 150 \qquad (cm) \tag{4.4}$$

which define the fiducial volume.
A further requirement on the existence of just one track satisfying the above criteria is formulated.
In order to reject background by $K^{\pm} \rightarrow \mu^{\pm}\nu$ and $K^{\pm} \rightarrow \pi^0\pi^{\pm}$, we consire the secondary charged 3-momentum reconstructed in the chamber evaluated in the Kaon rest frame (see fig. [**?**]), requiring:

$$p^{*} \leq 180 \qquad \text{MeV} \tag{4.5}$$

We have a 97.5 % of true recognized charged Kaon track, this percentage will approach 99.6 % after $\gamma\gamma \rightarrow \pi^0$ association (see section [**?**]).

4.2 The 4γ neutral vertex method

After a Kaon has been identified by the KPM algorithm and reconstructed into the drift chamber, the neutral vertex method is used in order to select events with two π^0 in the final state. The two π^0 are identified using the $\pi^0 \rightarrow \gamma\gamma$ decay and the calorimetric information of the photon clusters.

In order to estimate the position of the Kaon decay vertex, using only calorimetric information, we look for clusters in the electromagnetic calorimeter not associated to tracks in the DC, satisfying the following requests:

- If $E_i > 50$ MeV then $30^o < \theta_i < 150^o$
- If $15 < E_i < 50$ MeV then $20^o < \theta_i < 160^o$

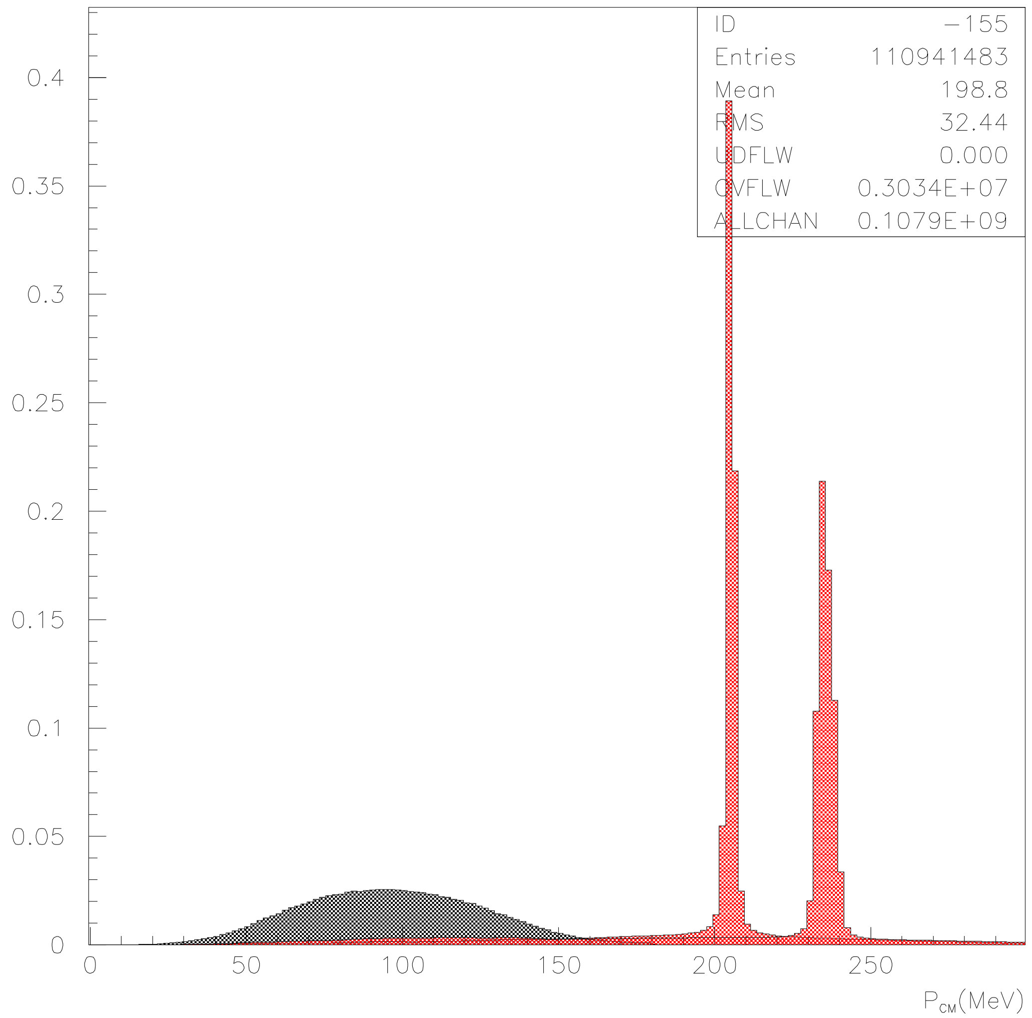

Figure 4.2: The secondary charged 3-momentumon evaluated in the charged K rest frame for signal (blue), $K^{\pm} \to \mu^{\pm}\nu$ and $K^{\pm} \to \pi^{0}\pi^{\pm}$ background (red) on MC. The first red peak correspond to $K^{\pm} \to \pi^{0}\pi^{\pm}$ events, the second to $K^{\pm} \to \mu^{\pm}\nu$.

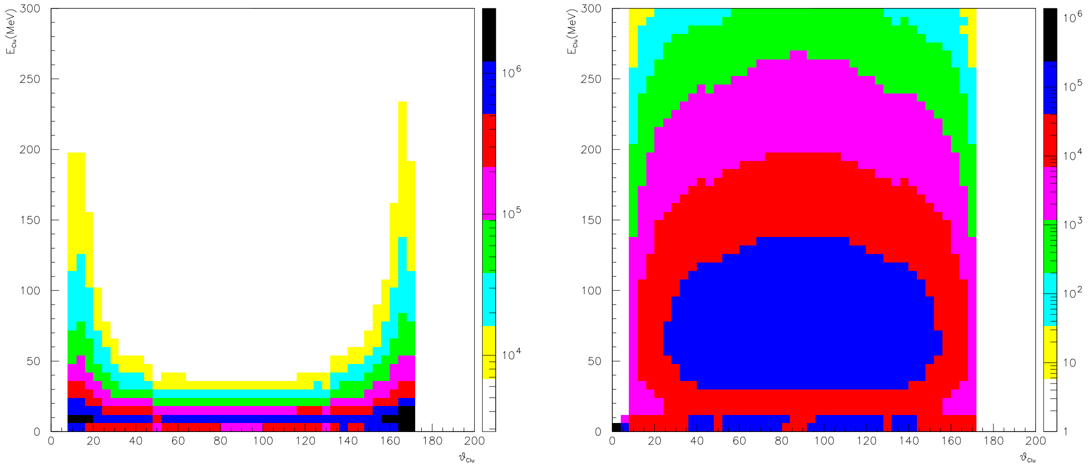

Figure 4.3: Scatter plot of the neutral clusters angle versus energy for accidental photons (left) and photons coming from a π^0 (right).

See figure [**?**] for a justification for the cuts above.

Then we require at least four clusters selected as before. Now the virtual Kaon helix is constructed, using an extrapolation procedure based on the Kaon track information reconstructed into the chamber and the best combination of four clusters on time with respect to a point on the virtual helix is searched:

$$(t - r/c)_{\gamma_1} = (t - r/c)_{\gamma_2} = (t - r/c)_{\gamma_3} = (t - r/c)_{\gamma_4} \tag{4.6}$$

moreover we impose the further request that the position of the Kaon decay vertex reconstructed into the chamber is compatible with the one obtained by the neutral vertex technique, based on the calorimetric information of the four neutral clusters

$$R_{Vtx}^{Charged} = R_{Vtx}^{Neutral} \tag{4.7}$$

The first one, $R_{Vtx}^{Charged}$, is the vertex reconstructed into the chamber; the second one, $R_{Vtx}^{Neutral}$, is obtained from the neutral vertex method.

In particular we defined

$$\mathrm{Pull}_{\delta t}^{ij} = \frac{(t_{cl}^{i} - t_{cl}^{j})}{\sigma_{tcl_{ij}}} \qquad \text{(6 relations)}$$

$$\mathrm{Pull}_{R_{Vtx}} = \frac{(R_{Vtx}^{Charged} - R_{Vtx}^{Neutral})}{\sigma_{R_{Vtx}}}$$

where t^i_{cl} is the time of the i^{th} cluster, $\sigma_{tcl_{ij}}$ represent the uncertainty on the time difference between the culster i and j, while $\sigma_{R_{Vtx}}$ is the uncertainty for the vertex position reconstructed into the chamber. The uncertainty $\sigma_{tcl_{ij}}$ is given by

$$\sigma_{tcl_{ij}} = \sqrt{\sigma^2_{tcl_i} + \sigma^2_{tcl_j}} \tag{4.8}$$

$$\tag{4.9}$$

Then, after we imposed

$$-4 < \text{Pull}^{ij}_{\delta t} < 4 \tag{4.10}$$

$$-4 < \text{Pull}_{R_{Vtx}} < 4 \tag{4.11}$$

we considered

$$\chi^2 = (\text{Pull}^{12}_{\delta t})^2 + (\text{Pull}^{13}_{\delta t})^2 + (\text{Pull}^{14}_{\delta t})^2 + (\text{Pull}^{23}_{\delta t})^2 + (\text{Pull}^{24}_{\delta t})^2 + (\text{Pull}^{34}_{\delta t})^2 + (\text{Pull}_{R_{Vtx}})^2$$

The position along the signal Kaon virtual helix that gives the minimum value of the χ^2 defines the neutral vertex position. Now, requiring $\chi^2 < 200$ it is possible to obtain a purity of ~ 90 %, at this level the background being represented by event without two π^0 in the final state.

This selection method allows to obtain resolution on the vertex position, defined as

$$Res^{Vtx}_x = x^{true}_{Vtx} - x^{Reco}_{Vtx}$$
$$Res^{Vtx}_y = y^{true}_{Vtx} - y^{Reco}_{Vtx}$$
$$Res^{Vtx}_z = z^{true}_{Vtx} - z^{Reco}_{Vtx}$$

(where the suffix *true* refers to the true value of the variable considered while *Reco* indicates the reconstructed observed value) of ~ 5 *cm* along x and y, ~ 6 *cm* along z (see table 4.1), as shown in figures (4.4) and (4.5). We obtain resolution on the signal Kaon momentum, given by

	x	y	z
Mean (cm)	0.28 ± 0.07	0.033 ± 0.006	-0.005 ± 0.008
σ (cm)	4.52 ± 0.01	4.49 ± 0.01	6.14 ± 0.01

Table 4.1: Summarizing table of the gaussian fit parameters of the Kaon vertex position resolution.

	x	y	z
Mean (MeV)	0.83 ± 0.01	0.14 ± 0.01	0.02 ± 0.01
σ (MeV)	7.54 ± 0.01	7.56 ± 0.01	7.221 ± 0.008

Table 4.2: Summarizing table of the gaussian fit parameters of the Kaon vertex momentum resolution.

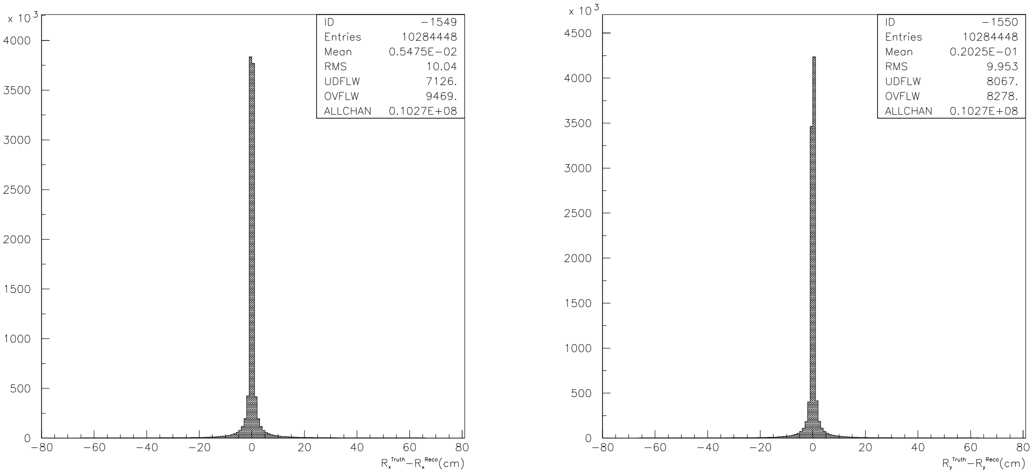

Figure 4.4: Kaon decay vertex position resolution, along x (right) and y (left).

$$
\begin{aligned}
Res_x^{p_k} &= p_{kx}^{true} - p_{kx}^{Reco} \\
Res_y^{p_k} &= p_{ky}^{true} - p_{ky}^{Reco} \\
Res_z^{p_k} &= p_{kz}^{true} - p_{kz}^{Reco}
\end{aligned}
$$

of $\sim 8\ MeV$ along x and y, $\sim 7\ MeV$ along z (see table 4.2), as shown in the figures (4.6) and (4.7).

We formulate the further request that the difference between the charged vertex and the neutral vertex is

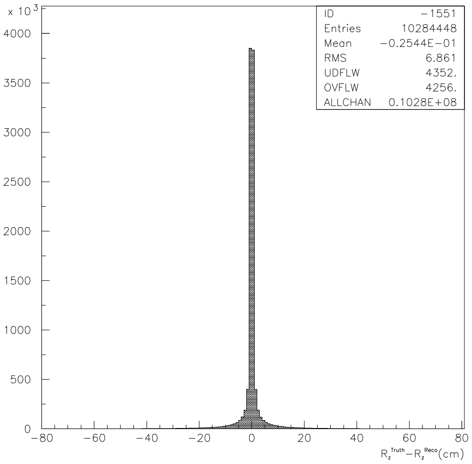

Figure 4.5: Kaon decay vertex position resolution, along z.

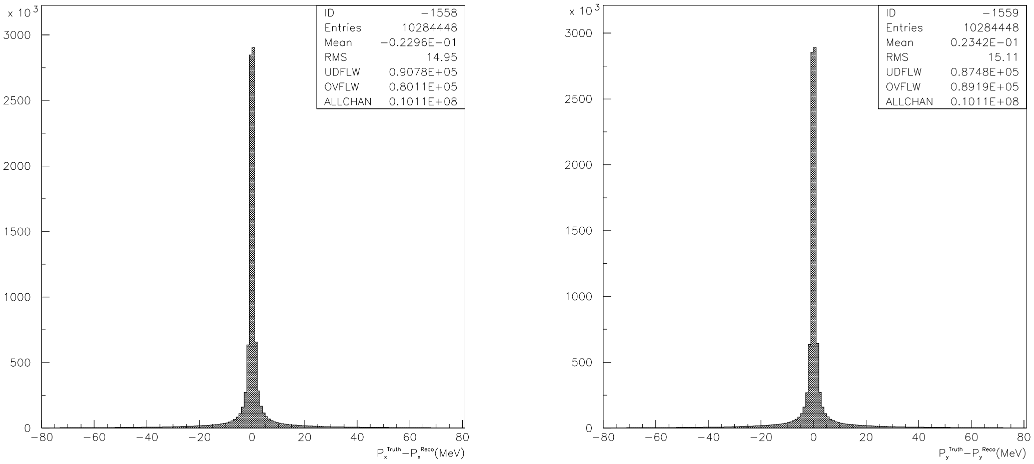

Figure 4.6: Kaon momentum at vertex resolution, along x (right) and y (left).

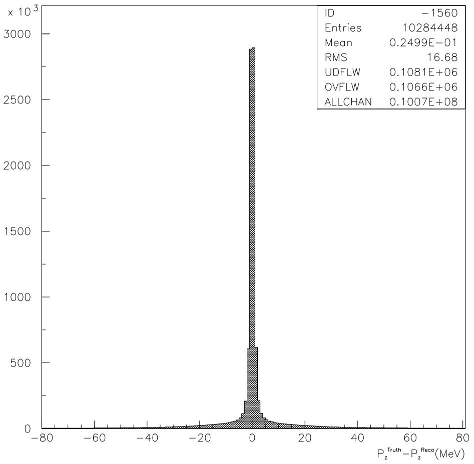

Figure 4.7: Kaon momentum at vertex resolution, along z.

$$-20\ cm < \Delta_{Vert} < 20\ cm \tag{4.12}$$

in order to reject non signal event (at this point the signal is everything with two π^0 in the final state).

4.3 $\gamma\gamma \to \pi^0$ association

The neutral vertex technique identifies events with two π^0 in the final state, but gives no information on the decaying photons belonging to the same π^0.
With the purpose of recognise the couple of photons belonging to the same π^0, we made a combinatory between the four photons found by the neutral vertex method, we defined

$$\mathrm{Pull}^{ij}_{mass} = \frac{\sqrt{2E_1E_2 \cdot (1-\cos\theta_{ij})} - M_{\pi^0}}{\sigma^{ij}_{mass}}$$

$$\sigma^{ij}_{mass} = \frac{\sigma_{Ecl_i}E_j(1-\cos\theta_{ij}) + \sigma_{Ecl_j}E_i(1-\cos\theta_{ij})}{\sqrt{2E_iE_j(1-\cos\theta_{ij})}}$$

where $\pi^0 = 134.98\ MeV$ is the π^0 mass.
We underline that, in order to tighten the resolution, for the evaluation of the cosine

between the photon cluster we used the information on the charged decay vertex (we refer to section (4.1) for detailed information).
This time we construct three χ^2, one for each possible couple among the 4 photons, the minimum one identifying the two π^0.

$$\chi^2_{ijkl} = (\mathrm{Pull}^{ij}_{mass})^2 + (\mathrm{Pull}^{kl}_{mass})^2 \tag{4.13}$$

It is possible, due to statistical reasons, that a χ^2 of the right association underfluctuates, so we consider the absolute difference between the best χ^2 and the nearest one

$$\Delta_{\chi^2} = |\chi^2_{best} - \chi^2_{near}| \tag{4.14}$$

and impose

$$\chi^2 < 7 \tag{4.15}$$
$$\Delta_{\chi^2} > 0.5 \tag{4.16}$$

Cutting this way, we obtained ~ 87 % of right associations and a percentage af events with less than two π^0 of ~ 8 %. Now the percentage of true recognized charged Kaon track is 99.6 %.

4.4 Kinematic fit

It is necessary to reduce the signal to background ratio, since until now we simply selected events with two π^0 in the final state, so the ratio between the signal and the normalization sample is essentially unchanged with respect to natural branching ratios. This can be done using a kinematic fit tecnique.
In a kinematic fit procedure the problem of serching the fitted variables is taken back to the minimization of a χ^2, making use of the Lagrange multiplier method for the minimization problem.
We made use of two kinematic fit, one in $K^{00}\pi3$ hypothesis and a second in $K^{00}e4$ hypothesis. In the following we summarize the parameters and costraints in the two cases.

$K^{00}\pi3$ hypothesis

The entry parameters to the fit are 26 and precisely:

- Energies, times and four photons position coordinates: E^i_{cl}, t^i_{cl}, x^i_{cl}, y^i_{cl}, z^i_{cl} (20 relations).

- Signal Kaon 3-momentum: p^K_x, p^K_y, p^K_z.

- Charged secondary 3-momentum: p^{sec}_x, p^{sec}_y, p^{sec}_z.

the parameter errors are the following:

- $\sigma_{E_{cl}} = \frac{0.057}{\sqrt{E_{cl}(GeV)}}$ cm.
- $\sigma_{t_{cl}} = \sqrt{\frac{54^2}{E_{cl}(GeV)} + 0.147^2}$.
- $\sigma_{x_{cl}} = \sigma_{y_{cl}} = 1.2$ cm and $\sigma_{z_{cl}} = \frac{1.2}{\sqrt{E_{cl}(GeV)}}$ cm (clusters on barrel);
  $\sigma_{x_{cl}} = \sigma_{y_{cl}} = \frac{1.2}{\sqrt{E_{cl}(GeV)}}$ cm and $\sigma_{z_{cl}} = 1.2$ cm (cluster on endcap).
- $\sigma_{p^K_i} = 0.5\%\ p^K_i$ MeV.
- $\sigma_{p^{sec}_i} = 0.5\%\ p^{sec}_i$ MeV.

We impose 12 constraints, on the 4-momentum conservation (4 relations), $\gamma\gamma \to \pi^0$ association (2 relations), six requiring 4 clusters on time, defined as:

- $E_K - E_{sec} - \sum_\gamma E_\gamma = 0$.

- $p_i^K - p_i^{sec} - \sum_\gamma p_i^\gamma = 0$ (3 relations).

- $m_{\gamma_1\gamma_2} = m_{\pi^0}$.

- $m_{\gamma_3\gamma_4} = m_{\pi^0}$.

- $\Delta t_{12} = (t_{cl_1} - \frac{r}{c}) - (t_{cl_2} - \frac{r}{c}) = 0$.
- $\Delta t_{13} = (t_{cl_1} - \frac{r}{c}) - (t_{cl_3} - \frac{r}{c}) = 0$.
- $\Delta t_{14} = (t_{cl_1} - \frac{r}{c}) - (t_{cl_4} - \frac{r}{c}) = 0$.
- $\Delta t_{23} = (t_{cl_2} - \frac{r}{c}) - (t_{cl_3} - \frac{r}{c}) = 0$.
- $\Delta t_{24} = (t_{cl_2} - \frac{r}{c}) - (t_{cl_4} - \frac{r}{c}) = 0$.
- $\Delta t_{34} = (t_{cl_3} - \frac{r}{c}) - (t_{cl_4} - \frac{r}{c}) = 0$.

$K^{00}e4$ **hypothesis**

The entry parameters to the fit are 27 in this case too, and precisely:

- Energies, times and four photons position coordinates: E_{cl}^i, t_{cl}^i, x_{cl}^i, y_{cl}^i, z_{cl}^i (20 relations).

- Signal Kaon 3-momentum:p_x^K, p_y^K, p_z^K.

- Charged secondary 3-momentum: p_x^{sec}, p_y^{sec}, p_z^{sec}.

the parameter errors are the same of the $K^{00}\pi3$ case.

This time it is not possible to ask for 4-momentum conservation due to undetected neutrino E_{miss} and p_{miss}. However we can ask for missing 4-momentum having zero mass.
We impose 9 constraints:

- $E_K - E_{sec} - \sum_\gamma E_\gamma - |p^\nu| = 0$
  where $\vec{p^\nu} = \vec{p^K} - \vec{p^{sec}} - \sum_\gamma \vec{p^\gamma}$.

- $m_{\gamma_1\gamma_2} = m_{\pi^0}$.

- $m_{\gamma_3\gamma_4} = m_{\pi^0}$.

- $\Delta t_{12} = (t_{cl_1} - \frac{r}{c}) - (t_{cl_2} - \frac{r}{c}) = 0$.
- $\Delta t_{13} = (t_{cl_1} - \frac{r}{c}) - (t_{cl_3} - \frac{r}{c}) = 0$.
- $\Delta t_{14} = (t_{cl_1} - \frac{r}{c}) - (t_{cl_4} - \frac{r}{c}) = 0$.
- $\Delta t_{23} = (t_{cl_2} - \frac{r}{c}) - (t_{cl_3} - \frac{r}{c}) = 0$.
- $\Delta t_{24} = (t_{cl_2} - \frac{r}{c}) - (t_{cl_4} - \frac{r}{c}) = 0$.
- $\Delta t_{34} = (t_{cl_3} - \frac{r}{c}) - (t_{cl_4} - \frac{r}{c}) = 0$.

Each of the previous fit gives a χ^2, in the following we will indicate by $P(\chi^2_{K^{00}_{\pi3}})$ the χ^2 probability from the fit in $K^{00}\pi3$ hypothesis and by $P(\chi^2_{K^{00}_{e4}})$ the one from the fit in signal hypothesis. In figure (4.8) it is shown the $P(\chi^2_{K^{00}_{\pi3}}) - P(\chi^2_{K^{00}_{e4}})$ distribution for signal and for the normalization.
The negative and positive value for the $P(\chi^2_{K^{00}_{\pi3}}) - P(\chi^2_{K^{00}_{e4}})$ distribution is due to events in which one of the kinematic fit procedure fails returnig a negative value for the χ^2 probabilities, we proceed ignoring such bad recondtructed events by asking for positive $P(\chi^2)$ for both fits procedures.
We point out that no cuts are imposed on such distribution, becouse the actual background rejection (section [**?**]) is performed using a Likelihood Ratio technique in which all the information used to do rejection of non-signal events are put together in order to get a maximum purity signal sample at the same time minimizing the statistical error on BR measurement.

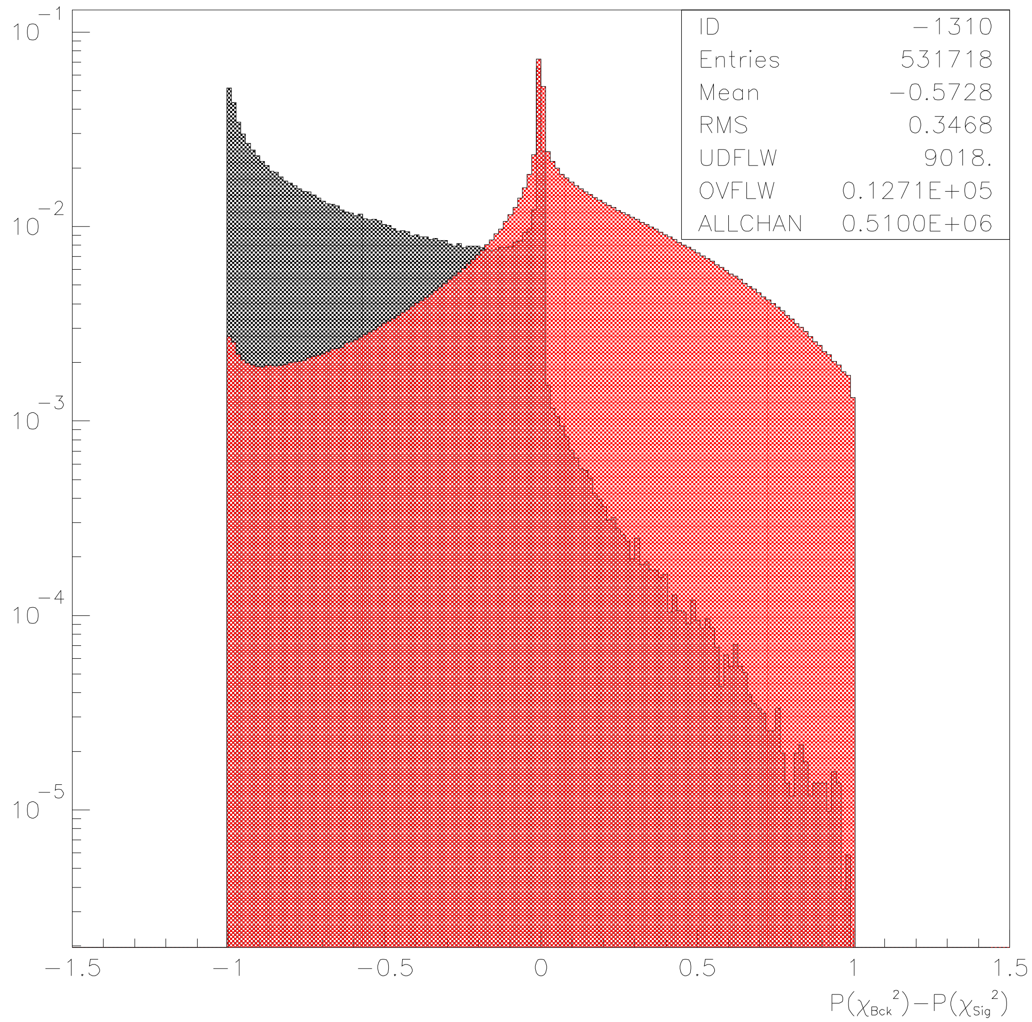

Figure 4.8: The $P(\chi^2_{K^{00}_{\pi3}}) - P(\chi^2_{K^{00}_{e4}})$ plotted for signal (black and the normalization sample (read) on MC. The overflows and underflows are due to events in which one of the kinematic fit procedure fails returnig a negative value for the χ^2 probabilities, we proceed ignoring such bad recondtructed events by asking for positive $P(\chi^2)$ for both fits procedures.

4.5 Track to cluster association

In the present section we describe how we construct the kinematic variables used to reduce background contamination, the way we reject the backgrounds and its nature will be discussed in the next section.
At this point of the analysis we need to know the calorimetric information on the secondary charged particles, in order to do background rejection .
The track-to-cluster association tecnique allows to identify the cluster in the EMC belonging to the charged secondary track. If the secondary charged particle has been traced in the drift chamber and the charged vertex reconstructed, we extrapolate the secondary track on the EMC and consider the cone with the last hit as top vertex, height equal to the extrapolation length and raduis of 30 cm. The cluster in the cone nearest to the extrapolation point is associated to the secondary track.

When all the information on the associated charged track are known, it is possible to estimate the secondary squared mass by the following formula:

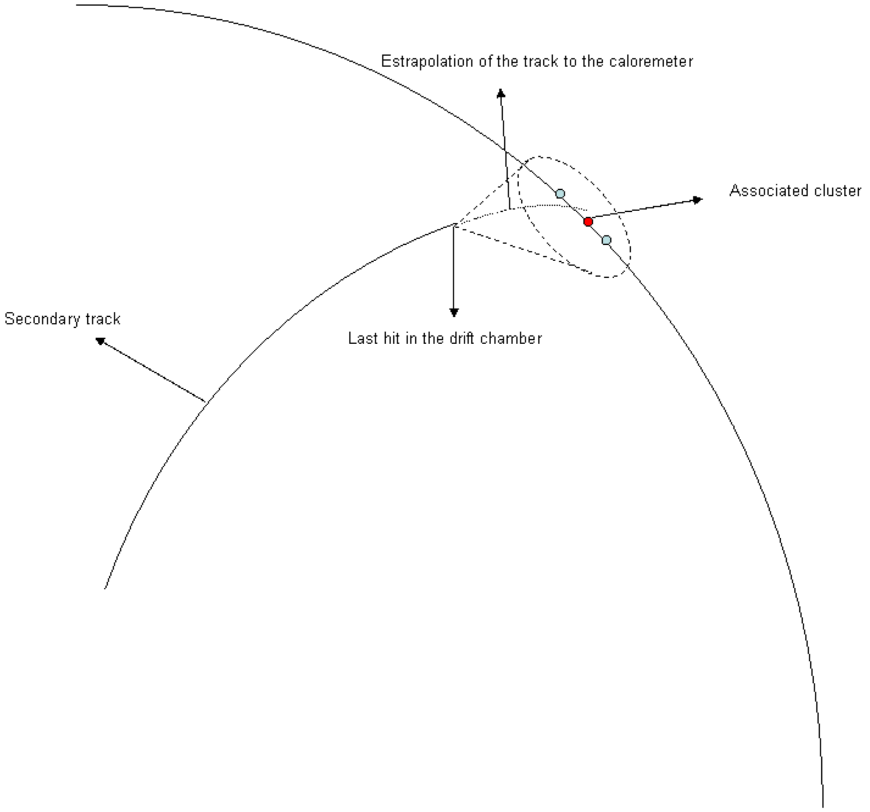

Figure 4.9: Schematization of the track-to-cluster association method.

$$m^2_{sec} = p^2\big\{\big((t^{sec}_{cl} - t_{vtxneu}) \cdot \frac{c}{L_{trk}}\big)^2 - 1\big\} \tag{4.17}$$

t^{sec}_{cl} is the time of the cluster associated to the secondary charged track, p the secondary momentum measured in the drift chamber, t_{vtxneu} represent the time of the neutral vertex and L_{trk} is the track length between the charged decay vertex and the impact point on the calorimeter.

In figure (4.10) is shown the m^2 distribution for the secondary track, the peak around ~ 20000 MeV^2 is the one corresponding to the squared mass of a charged pion while the peak around zero is due to electron. It is possible to note a widening of the the curve for negative value of the squared mass, it is due to $K^{00}\pi 3$ background (we refer to section [**?**] for background in-depth study).

The TCA technique allows to construct a lot of kinematic interesting variables, used to reject backgrouds events (for details on background composition and characteristics we refer to section [**?**]).
Indeed once the culster associated to the secondary charged particle is known it is possible use all the chamber and calorimetric informations to calculate kinematic quantity that reflect the differences between signal and background topology and consequently turn out to be very useful to reject non signal events.

Signal	$K^{00}\pi 3$	K_{e3}	S/B
2902	$0.10895 \cdot 10^7$	75167	0.0025

Table 4.3: In table are reported the number of events for the signal, for the two backgrounds decay and the signal-to-background ratio, after the track-to-cluster association.

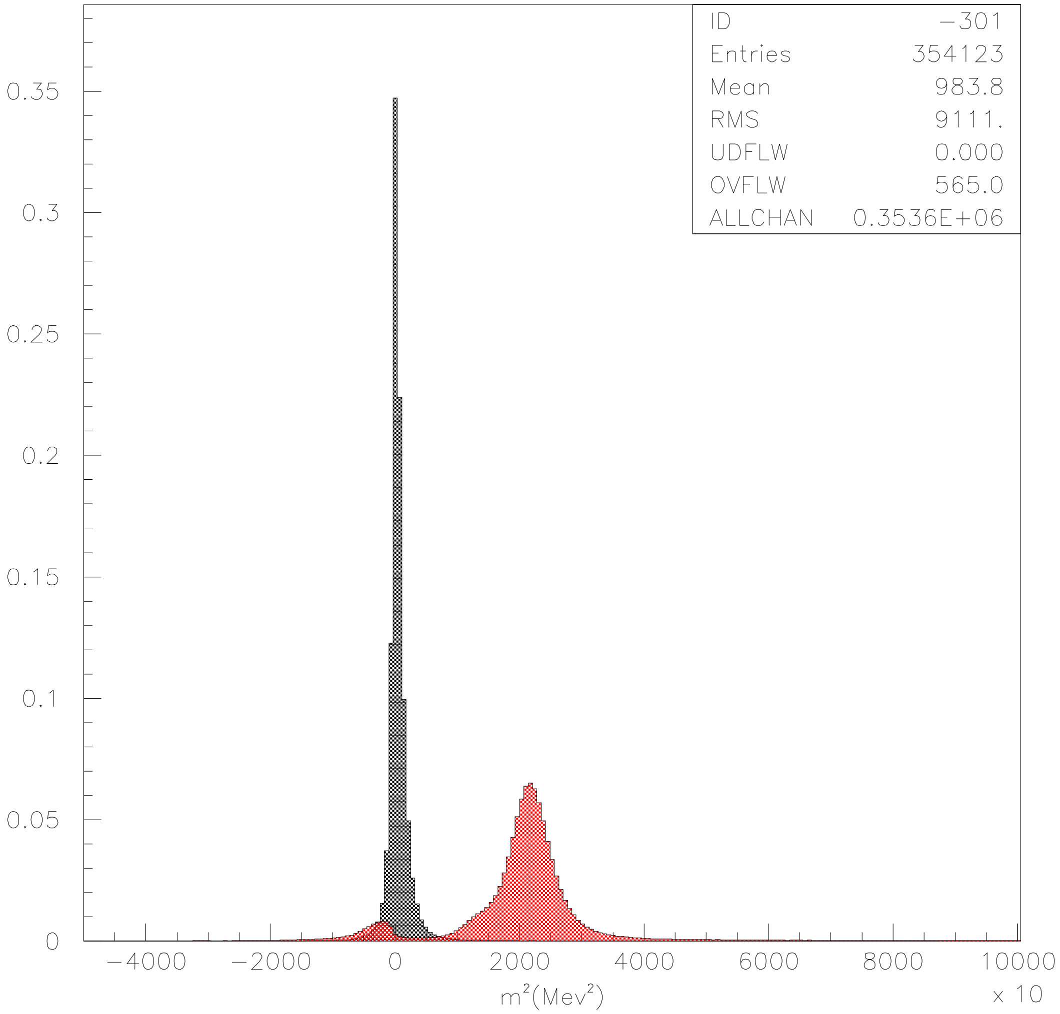

Figure 4.10: The m^2 distribution for the secondary charged track, obtained by formula (4.17). In black is represented the signal, which distribute around zero, while in red the normalization events ($K^{00}\pi3$) that shows a peak around the m^2 value of a charged pion with a widenig in the signal region, due to bad reconstructed $K^{00}\pi3$ decay (see next section for detail).

4.6 Background rejection

In the following we describe the nature of the contributions to background and the kinematical variables used to reject it. In order to obtain the maximum signal purity, the actual background rejection is performed by means of a Likelihood Ratio method. For a detailed treatement of hypothesis test based on Likelihood Ratio technique we

refer to section [**?**].
So in what follow we perform a background analysis illustrating the variables suitable to reduce contamination by non-signal events. We remark that besides the variables discussed in what follows, peculiar for each kind of background, we use the $P(\chi^2_{K^{00}_{\pi3}}) - P(\chi^2_{K^{00}_{e4}})$ distribution to do rejection of both $K^{00}\pi3$ and K_{e3} background (see figure [**?**]). Indeed such variable distribute differently for signal, $K^{00}\pi3$ and K_{e3} (which constitute the two contribution to background) and it turns out useful to reject both backgrounds.
The background is constituted by:

- $K^{00}_{\pi3}$ events with the charged pion wrongly associated to a photon cluster in the calorimeter, the rejection method is based on $\pi - e$ discrimination in the electromagnetic calorimeter.
- K_{e3} radiative events with at least one splitted cluster in the EMC, the rejection is based on the difference in the missing 4-momentum distibution and on the distribution of the minimum angle between the secondary charged track and the photon.

$K^{00}_{\pi3}$ background

The main background is constituted by the normalization sample events, which have a topology very similar to signal becouse of the presence of two π^0 in the final state. Actually all the technique adopted until now select both signal and $K^{00}_{\pi3}$ with essentially same efficiency, so that te signal to $K^{00}_{\pi3}$ background ratio is still the same at the natural branching ratio level.
Let us now focus on the squared mass distribution, subsequently used to do $\pi - e$ discrimination into the electromagnetic calorimeter using the Likelihood Ratio method as discussed in the next section, in order to understand which kind of backgorund we have to fight.
For what concern the $K^{00}_{\pi3}$ background, a MC study has shown that around 0 Mev^2 (signal region, the one that will be selected by the Likelihood Ratio routine) the widening of the curve observed in the m^2 distribution (fig 4.10) for negative values of the secondary squared mass is due to charged pion track wrongly associated to photon clusters in the calorimeter (see figure 4.11). Suppose a charged pion track has been wrongly associated to a photon cluster, if we look at the β of the particle,

$$\beta = \frac{L_{trk}}{(t^{sec}_{cl} - t_{vtxneu}) \cdot c} \tag{4.18}$$

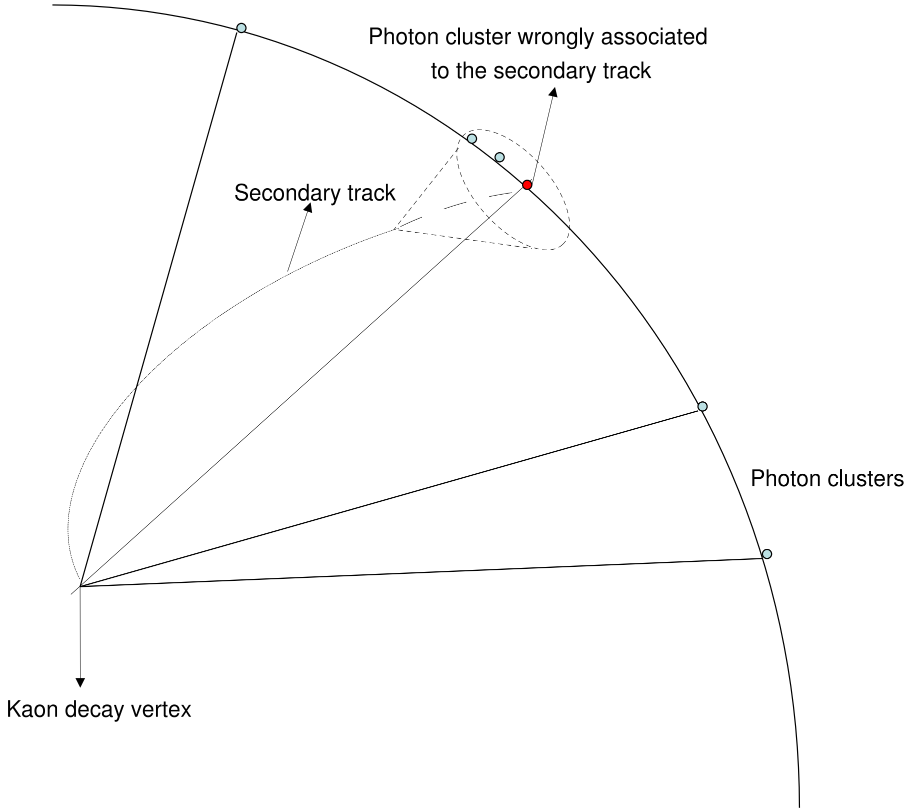

Figure 4.11: A $K^{00}_{\pi 3}$ event in which the secondary track has been wrongly associated to a photon cluster in the elettromagnetic calorimeter.

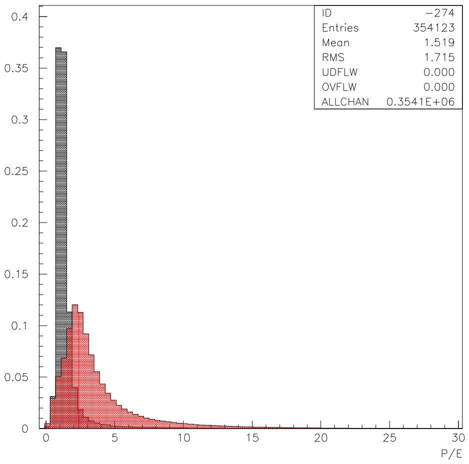

Figure 4.12: The distribution of P/E ratio for signal (black) and $K^{00}\pi3$ background (red).

we realize that t_{cl}^{sec} is underestimated, being the one of a photon, while L_{trk} is overestimated, being the length of a charged particle, so equation (4.18) gives $\beta > 1$. In fact we are requiring a massive particle to cover in the time interval $(t_{cl}^{sec} - t_{vtxneu})$ a distance greater than the one that a photon would cover in the same time interval.
Now let us rewrite equation (4.17) as follows:

$$m_{sec}^2 = p^2 \left(\frac{1-\beta^2}{\beta^2} \right) \tag{4.19}$$

which gives $m^2 < 0$ for $\beta > 1$.
We can conclude that the widening in the m^2 distribution for negative values of the squared mass (see figure 4.10) is due to $K^{00}\pi3$ events with the secondary track wrongly associated to a photon cluster, as a MC study has confirmed.

In order to reject the $K^{00}\pi3$ background, two more kinematic quantity are considered: the secondary charged 3-momentum distribution P_{sec} and the ratio between the 3-momentum reconstructed into the chamber and the energy released into the electromagnetic calorimeter P/E (see figures [**?**] and [**?**]). Signal and $K^{00}\pi3$ background have different shapes in this distribution, so that them can be used to reject this kind of background.

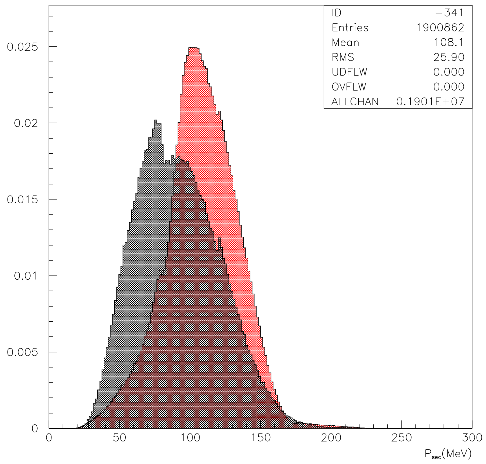

Figure 4.13: The 3-momentum of the secondary charged track for signal (black) and $K^{00}\pi 3$ background (red).

K_{e3} background

The K_{e3} background is essentially due to radiative $K^{\pm} \rightarrow \pi^0 e^{\pm} \nu_e(\overline{\nu_e})\gamma$ events with at least one splitted cluster in the EMC. Even if both signal and K_{e3} background have a neutrino in the final state, that goes away undetected, there are still differences in the missing 4-momentum distibution due to different K_{e3} 3-body decay topology with respect to the 4-body signal decay.
In order to reject this background we considered the $E_{miss} = E_K - E_{sec} - E_{\pi^0_1} - E_{\pi^0_2}$ variable (the neutrino energy, see figure **??**), the minimum angle $\theta^{Trk-\gamma}_{min}$ between the 4 photons and the secondary track (figure **??**) and $E^2_{miss} - P^2_{miss}$ distrubution (figure **??**).
The missing neutrino energy is defined in signal hypothesis, so we have:

$$E_{miss} = E_K - E_{sec} - E_{\pi^0_1} - E_{\pi^0_2} \tag{4.20}$$

where E_K is the kaon energy, E_{sec} the energy of the secondary charged track and E_{π^0} stands for two π^0 energies.
The missing neutrino 3-momentum is defined as:

$$P_{miss} = P_K - P_{sec} - P_{\pi^0_1} - P_{\pi^0_2} \tag{4.21}$$

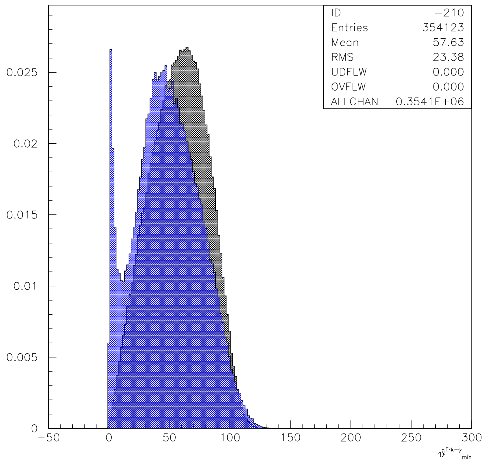

Figure 4.14: The distrubution of the minimum angle $\theta_{min}^{Trk-\gamma}$ between secondary track and photon for signal (black) and K_{e3} background (blue).

with obvious symbols meaning.
The two π^0 energies used to compute the neutrino missing 4-momentum, are costrained by means of a kinematic fit procedure, in order to tighten the resolutions. The way it works is the same as discussed in section [**?**], but this time only parameters regarding the two π^0 are considered. So we have 4 entry parameters, the four energies correspondig to four photons of the two π^0 with two constraints regarding the two invariant π^0 mass requirements:

- $m_{\gamma_1\gamma_2} = m_{\pi^0}$.

- $m_{\gamma_3\gamma_4} = m_{\pi^0}$.

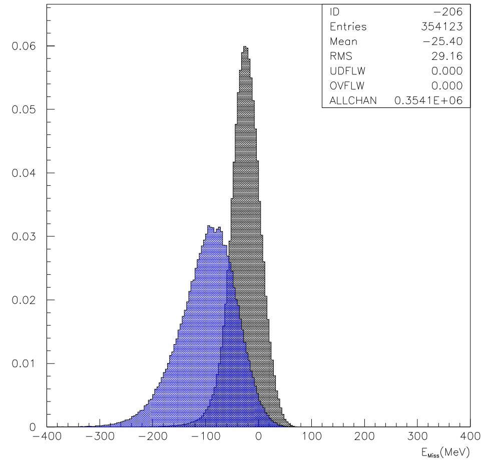

Figure 4.15: The neutrino energy distribution E_{miss} distribution for signal (black) and K_{e3} background (blue).

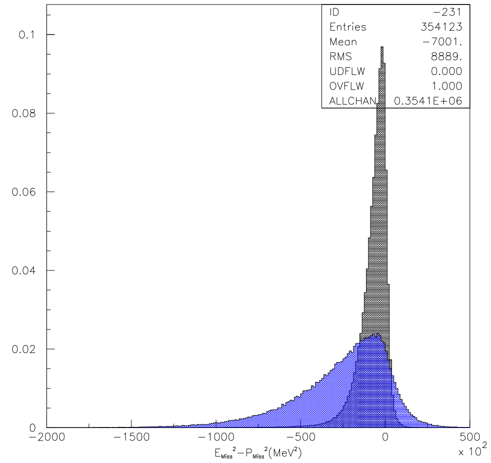

Figure 4.16: The $E^2_{miss} - P^2_{miss}$ distribution for signal (black) and K_{e3} background (blue).

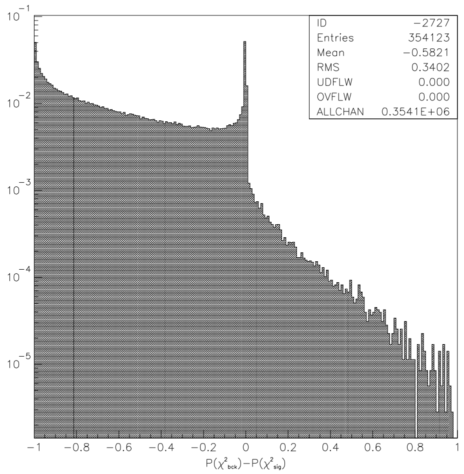

Figure 4.17: The $P(\chi^2_{K^{00}_{\pi3}}) - P(\chi^2_{K^{00}_{e4}})$ distribution for signal after the track-to-cluster association level.

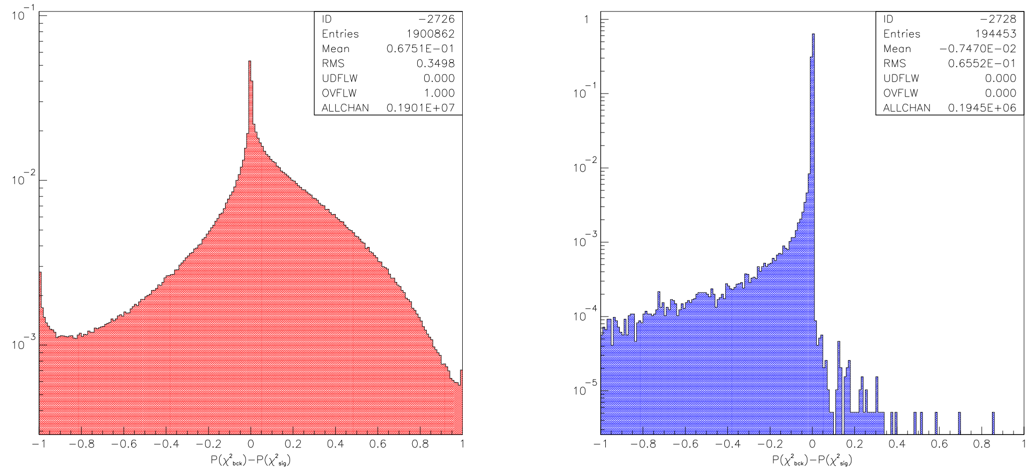

Figure 4.18: The $P(\chi^2_{K^{00}_{\pi3}}) - P(\chi^2_{K^{00}_{e4}})$ distribution for $K^{00}_{\pi3}$ (red) and K_{e3} (blue) background after the track-to-cluster association level.

4.6.1 Working of the Likelihood Ratio Algorithm

A Likelihood Ratio procedure, based on the Neyman-Pearson Lemma ([**?**]), has been developed to reduce contamination by $K^{00}_{\pi3}$ and K_{e3} events. A Likelihood Ratio procedure allows to obtain the maximum signal purity for a given efficiency cut. So the problem on the choice of the cut is left open, but can be simply solved as we will discuss later.

The Likelihood Ratio technique works in the following way: for each single event, probability to be signal, $K^{00}_{\pi 3}$ background and K_{e3} background is calculated, looking at the Monte Carlo distributions for signal and background showed in the previous section. Once we assigned to each events such probabilities (assumed independent), the following ratio are considered:

$$R_1 = \frac{P_{Sig}(Prob_{\chi^2_{Fit}}) \cdot P_{Sig}(P/E) \cdot P_{Sig}(m^2) \cdot P_{Sig}(P_{sec})}{P_{K^{00}_{\pi 3}}(Prob_{\chi^2_{Fit}}) \cdot P_{K^{00}_{\pi 3}}(P/E) \cdot P_{K^{00}_{\pi 3}}(m^2) \cdot P_{K^{00}_{\pi 3}}(P_{sec})}$$

$$R_2 = \frac{P_{Sig}(Prob_{\chi^2_{Fit}}) \cdot P_{Sig}(E^2_{miss} - P^2_{miss}) \cdot P_{Sig}(\theta^{Trk-\gamma}_{min}) \cdot P_{Sig}(E_{miss})}{P_{K_{e3}}(Prob_{\chi^2_{Fit}}) \cdot P_{K_{e3}}(E^2_{miss} - P^2_{miss}) \cdot P_{K_{e3}}(\theta^{Trk-\gamma}_{min}) \cdot P_{K_{e3}}(E_{miss})}$$

where (i stands for: signal, $K^{00}_{\pi 3}$ or K_{e3}; j stands for: signal, $K^{00}_{\pi 3}$; k stands for signal, K_{e3})

- $P_i(Prob_{\chi^2_{Fit}})$ is the probability for an event to be signal, $K^{00}_{\pi 3}$ or K_{e3} calculated on the $P(\chi^2_{K^{00}_{\pi 3}}) - P(\chi^2_{K^{00}_{e4}})$ Monte Carlo distribution.

- $P_j(P/E)$ is the probability for an event to be signal or $K^{00}_{\pi 3}$ calculated on the P/E Monte Carlo distribution.

- $P_j((m^2)$ is the probability for an event to be signal or $K^{00}_{\pi 3}$ calculated on the m^2 Monte Carlo distribution.

- $P_j(P_{sec})$ is the probability for an event to be signal or $K^{00}_{\pi 3}$ calculated on the P_{sec} Monte Carlo distribution.

- $P_k(E^2_{miss} - P^2_{miss})$ is the probability for an event to be signal or K_{e3} calculated on the $E^2_{miss} - P^2_{miss}$ Monte Carlo distribution.

- $P_k(\theta^{Trk-\gamma}_{min})$ is the probability for an event to be signal or K_{e3} calculated on the $\theta^{Trk-\gamma}_{min}$ Monte Carlo distribution.

- $P_k(E_{miss})$ is the probability for an event to be signal or K_{e3} calculated on the E_{miss} Monte Carlo distribution.

The entire kinematic informations on signal and background has been condensed into the two quantity returned by the Likelihood ratio routine, so that it is possible to do background rejection simply imposing a cut on R_1 in order to reject $K^{00}_{\pi 3}$ background and on R_2 to reject K_{e3} background, with the guarantee of obtaining the maximum signal purity sample, assured by the Neyman-Pearson Lemma ([**?**]).

As we said, the problem on the choice of the cut (*i.e.* the efficiency of the cut) on the variables returned by the Likelihood Ratio technique has to be solved. It can be shown that in order to minimize the statistical error after formal background subtraction, the cut on a given distribution should be chosen in order to maximize the significance given by the ratio

$$C = \frac{S}{\sqrt{S+B}}$$

Indeed if we consider the total number $N = S + B$ of observed events on data, signal plus background, so that we have $S = N - B$, the error on S will be given by:

$$\delta_S = \sqrt{N} = \sqrt{S+B}$$

or

$$\frac{\delta_S}{S} = \frac{1}{C} \tag{4.22}$$

so that minimizing C is equivalent to minimize the relative error on the events number obtained after formal background subtraction.
Let us generalize the argument above to the case in which the Monte Carlo simulation statistics is greater than the data sample by a costant factor k. Suppose the MC total number of events is

$$N_S^{MC} = k \cdot B$$

where k is a costant, the error on N_S^{MC} will be given by

$$\sigma_{N_S^{MC}} = \sqrt{k \cdot B} \tag{4.23}$$

The Monte Carlo number of events scaled in order to be equal to that in data and its error is given by

$$B = \frac{N_B^{MC}}{k} \tag{4.24}$$

$$\sigma_B = \frac{\sigma_{N_S^{MC}}}{k} = \sqrt{\frac{B}{k}} \tag{4.25}$$

Now the total error will be given by the squared sum of [?] and [?]:

$$\sigma^2 = \sigma^2_{Data} + \sigma^2_B = S + B + \frac{B}{k}$$

that gives

$$\sigma = \sqrt{S + (\frac{k+1}{k}) \cdot B} \tag{4.26}$$

So if we want to minimize the relative statistical error when the Monte Carlo simulation statistics is greater than the data sample by a costant factor k we have to maximize the ratio obtained generalizing equation [?]:

$$C_k = \frac{S}{\sqrt{S + (\frac{k+1}{k}) \cdot B}} \tag{4.27}$$

The above shows a possible criterion, suitable for this analysis and indeed adopted, for chosing the cuts on the quantity returned by the Likelihood Ratio method.
The cuts on R_1 and R_2 that maximize equation [?] are:

$$R_1 > 75 \tag{4.28}$$

$$R_2 > 100 \tag{4.29}$$

Cutting this way we observed 1448 signal events on Monte Carlo with a signal to background ratio $S/B \sim 1.15$.

It is possible to further improve the S/B ratio considering the secondary charged β distribution, shown in figure [?]. It is possible to note a population for negative β value constituted only by residual normalization events. The reason why, after the background rejection, we still have residual normalization events which a such peculiar kinematic can be explained looking at the equation [?], that we report here:

$$m_{sec}^2 = p^2 \left(\frac{1-\beta^2}{\beta^2} \right) \tag{4.30}$$

the secondary charged β is expressed like

$$\beta = \frac{L_{Trk}}{(t_{sec}^{cl} - t_{vtx}) \cdot c} \tag{4.31}$$

with L_{Trk} the total lenght of the secondary charged track in the chamber (from the decay vertex to the electromagnetic calorimeter), t_{sec}^{cl} the time of the cluster into the electromagnetic calorimeter associated to the secondary charged track extrapolated to the calorimeter, t_{vtx} the time of the charged kaon decay vertex reconstructed into the chamber and c the speed of light.
Now, when the charged pion, coming from a $K_{\pi 3}^{00}$ decay, is wrongly associated to a photon cluster coming from the IP (so that $t_{sec}^{cl} < t_{Vtx}$) or to an accidental photon cluster with $t_{sec}^{cl} < t_{Vtx}$, this produce a negative β value. The reason why we observe a residual $K_{\pi 3}^{00}$ background with negative β value distributing around -1 is that cutting on the probabilities ratio returned by the Likelihood Ratio method R_1, we select region in m_{sec}^2 around zero (signal region) in which enters $K_{\pi 3}^{00}$ decays with the secondary charged pion wrongly associated producing a negative β value distibuting around -1. This is evident if we replace $\beta = -1$ in equation [**?**], obtaining $m_{sec}^2 = 0$.

It is importan to underline that the such peculiar $K_{\pi 3}^{00}$ structure in the secondary charged β distribution will be crucial for the systematic effects cross check, providing a way to evaluate the residual normalization events contamination directly on data, as we will dicuss in the following chapter.

So, after the cuts on R_1 and R_2, we decided to further reject the $K_{\pi 3}^{00}$ background by imposing a cut on β, instead of including such distribution into the Likelihood ratio procedure, asking for:

$$0.8 < \beta < 1.3 \tag{4.32}$$

Cutting this way we observed 1441 signal events (so the efficiency on the β cut is essentially $\simeq 99.5\,\%$ for the signal) on Monte Carlo with a signal to background ratio now improved to $S/B \sim 1.58$ (see table [**?**]).

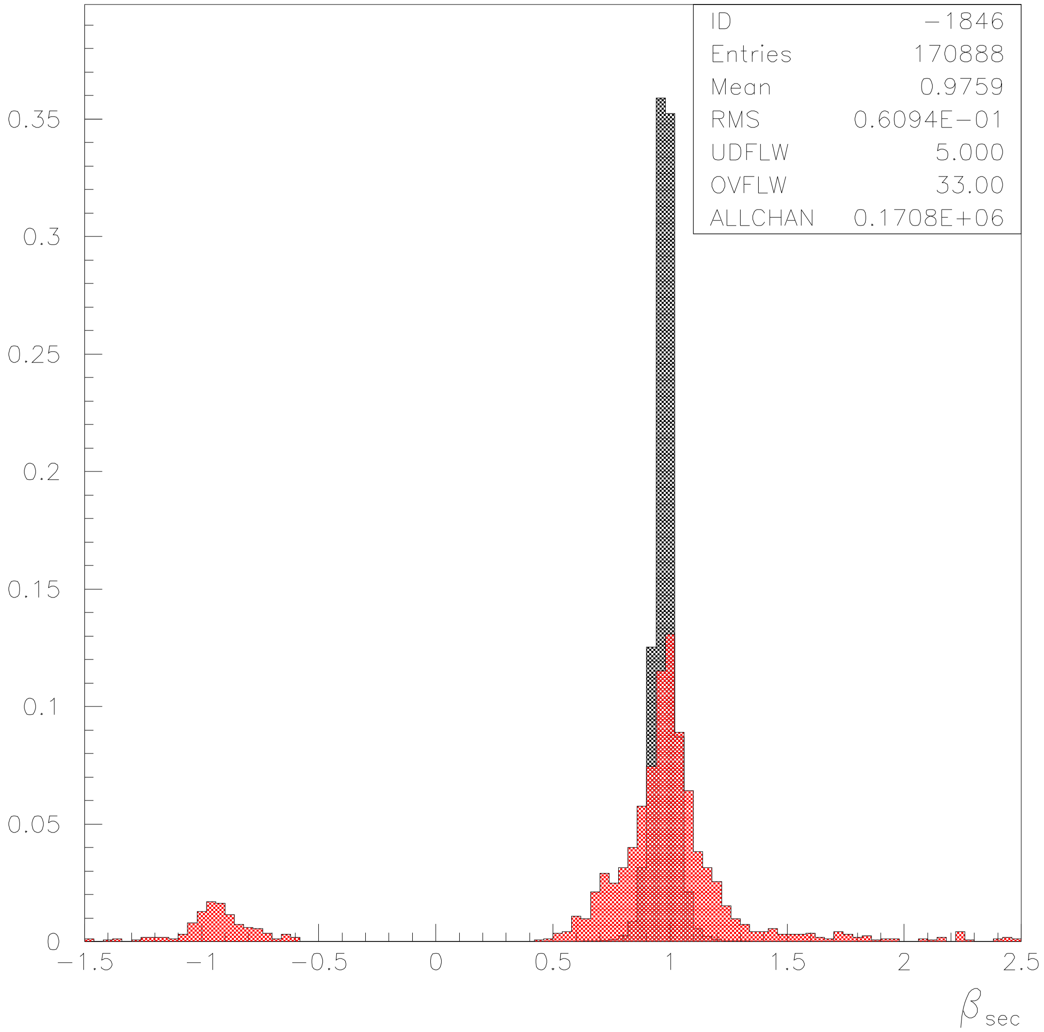

Figure 4.19: The secondary charged β distribution for signal (black) and normalization events (red) after the cuts on R_1 and R_2. It is possible to note a population for negative β value constituted only by residual normalization events in which the secondary charged pion track has been wrongly associated to a accidental photon cluster or to a photon coming from the IP, thus giving a negative $\beta \approx -1$ value and consequently a $m^2_{sec} \approx 0$ value in the signal region.

Signal	$K^{00}\pi 3$	K_{e3}	S/B
1448	636	281	1.58

Table 4.4: In table are reported the number of events for the signal, for the two backgrounds decay and the signal-to-background ratio, after the background rejection and the cut on the secondary charged β distribution. Before background rejection (*i.e* track-to-cluster association level) was 0.0025, see table [**?**]

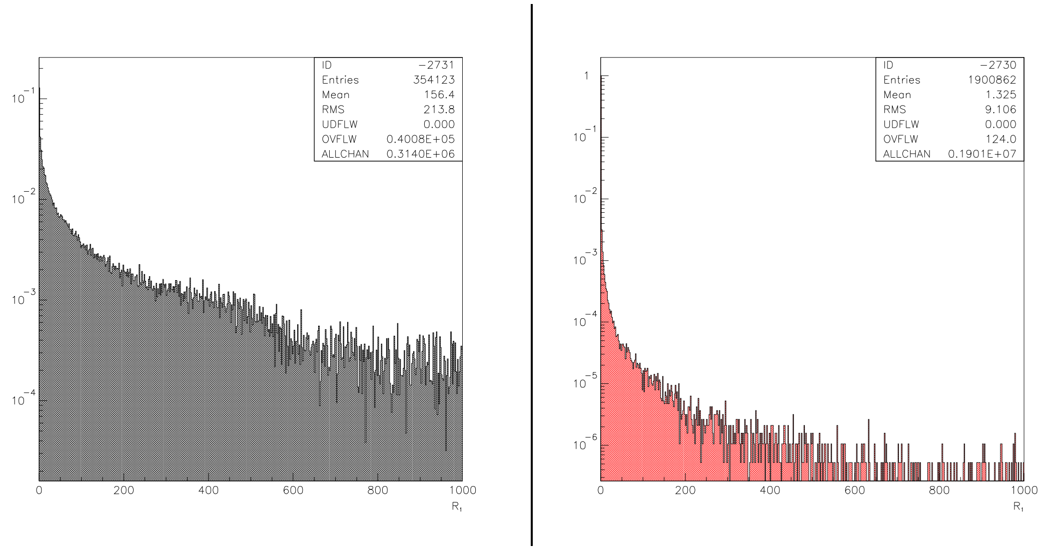

Figure 4.20: The R_1 distribution for signal (black) and $K^{00}_{\pi 3}$ (red).

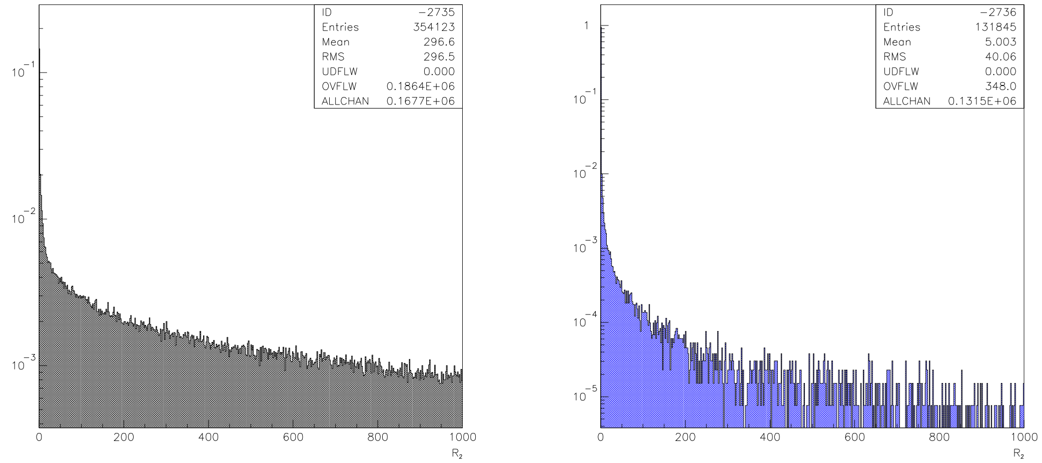

Figure 4.21: The R_2 distribution for signal (black) and K_{e3} (blue).

Chapter 5

Branching Ratio measurement

5.1 Introduction

In the present chapter we describe the method adopted to perform the Branching Ratio measurement of K_{e4}^{00} decay, which stands for $K^{\pm} \rightarrow \pi^0 \pi^0 e^{\pm} \nu_e (\overline{\nu_e})$.

In the following chapter we will discuss in details the techique used to estimate on data the amount of residual background, the latter being still a non negligible fraction of the total events selected. Then we proceed illustrating the fit procedure employed to estimate signal and residual background fractions on data and the measurement method adopted, based on a least-square estimator, to evaluate the Branching Ratio. We will describe how the normalization sample is selected and the way systematic effects due to signal efficiency and background subtraction technique are taking into account.

In order to cross check the systematic effects study, we developed a method that allows to estimate the contamination by $K_{\pi 3}^{00}$ (which represent the main contribution to total background) on data and used the result obtained to correct the Monte Carlo prediction for the BR.

5.2 Data sample

We used the whole statistic collected by KLOE during 2001, 2002, 2004 and 2005 about $2054\,pb^{-1}$, processed and filtered with the KLOE standard reconstruction software and the events classification procedure. We require the most recent reconstruction version available and in particular we require version reconstruction 15 for 2001 data ($\sim 90\ pb^{-1}$), version 16 for 2002 data sample ($\sim 236\ pb^{-1}$), version 26 for 2004 ($\sim 445\ pb^{-1}$) and 2005 data sample ($\sim 1045\ pb^{-1}$).
As far as the Monte Carlo is concerned, we use $1817\,pb^{-1}$ of integrated luminosity of the most recent Monte Carlo version available.
Considering the Data-MontCarlo ratio for the luminosity, evaluated using bhabha scattering, we have:

$$L^{Bhabha}_{MC}/L^{Bhabha}_{Data} = 0.8847$$

so that the Branching Ratio measurement obtained by formal MC background subtraction has to be corrected with this Data-MC ratio luminosity factor.

5.3 The measurement method

The residual background is a non negligible fraction of the total number of selected events (see table [?]), so it would be highly preferable to make use of a method which allows to evaluate the actual residual background fraction, as well as signal fraction, directly on data.
The first step consists into characterize some variables that distribute differently for signal and the two remaining backgrounds: residual events of the normalization sample ($K^{00}_{\pi 3}$, $\sim 69\,\%$ of the total), and K_{e3} events.
After the very hard selection made in order to reject the non signal events, almost all the relevant kinematic variables come out quite similar, nevertheless we found three suitable variables useful to our purpose.

- The charged secondary 3-momentum P_{sec}.
- The error on the secondary charged squared mass propagated from the reconstruction matrix $\sigma^{Reco}_{m^2}$.
- The kinematical variable $s_0^{CM} = \frac{1}{3}[m_K^2 + 2m_{\pi^0}^2 + (2E^{CM}_{sec}E^{CM}_{\nu} - \overrightarrow{P}^{CM}_{sec}\overrightarrow{P}^{CM}_{\nu})]$.

where the superscript CM indicates that the quantity is evaluated in the Kaon rest frame.
In figures [?], [?] and [?] are shown the distrubution for P_{sec}, $\sigma^{Reco}_{m^2}$ and s_0 respectively

at the level of the track-to-cluster association (before the cuts on the variable returned by the Likelihood Ratio procedure R_1 and R_2).

For what concerns the charged secondary 3-momentum P_{sec} it comes out that, after the hard selection done in order to reject the background, this variable distribute differently for signal and background (*i.e* we have selected different 3-momentum region for background and signal in the end of the analysis).

The second variable is the sigma we expect on the secondary charged m^2 computed by propagating the errors on charged track reconstruction quantity, which are the secondary charged curvature k and the cotangent of the angle θ_{Reco} between the direction of the secondary charged 3-momentum and the direction af the magnetic filed in the chamber (see figure [**?**]). Now, the error on the secondary charged squared mass $\sigma_{m^2}^{Reco}$ can be computed by propagating the errors on k and $\cot\theta_{Reco}$. Let us write m^2 as (cfr. section [**?**]):

$$m_{sec}^2 = p^2\left(\frac{1-\beta^2}{\beta^2}\right)$$

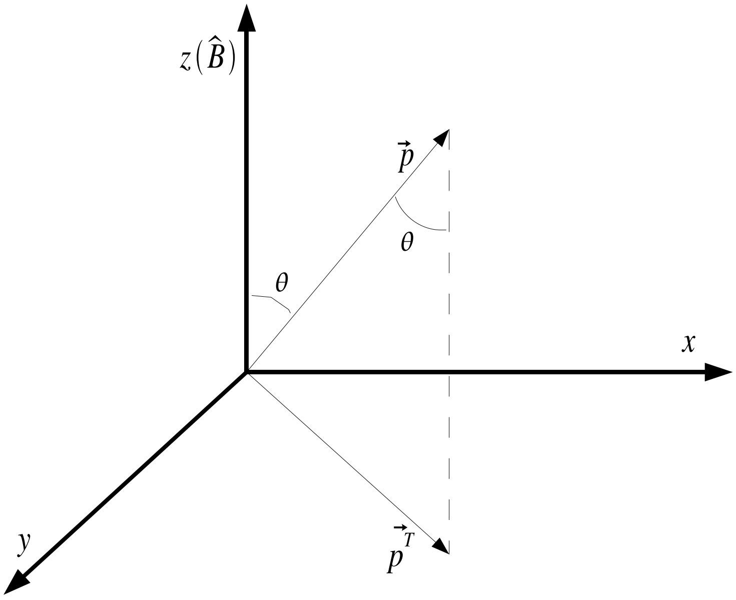

Figure 5.1: Reconstruction quantity scheme.

so that we have:

$$\sigma_{m^2}^{Reco} = [\frac{\partial m^2}{\partial p} \cdot \sigma_p]^2 + [\frac{\partial m^2}{\partial \beta} \cdot \sigma_\beta]^2 \tag{5.1}$$

In order to compute the error given by the formula above, we need to know σ_β and σ_p. A good approximation of the first is simply evaluated considering the half difference on secondary charged β between the track first hit and the track last hit in the drift chamber, in formula:

$$\sigma_\beta = \frac{\beta_{FirstHit} - \beta_{LastHit}}{2} \tag{5.2}$$

while σ_p has to be propagated by the errors on k and $\cot\theta$ (from now on let us indicate $\cot\theta_{Reco}$ by simply writing $\cot\theta$), contained in the reconstruction error matrix, by the following formulas:

$$\overrightarrow{P}^2 = \overrightarrow{P}_T^2 + \overrightarrow{P}_z^2 = (\overrightarrow{P} \cdot \sin\theta)^2 + (\overrightarrow{P} \cdot \cos\theta)^2 \tag{5.3}$$

$$R_{Reco} = \frac{1}{k} = \frac{P_T}{q \cdot B} = \frac{P \cdot \sin\theta}{q \cdot B} \tag{5.4}$$

where $\overrightarrow{P}^2$ is the secondary charged 3-momentum, $\overrightarrow{P}_T = \overrightarrow{P}^2 \sin\theta$ is the transverse secondary charged 3-momentum, $\overrightarrow{P}_z$ is the z-component of the secondary charged 3-momentum, R_{Reco} is the radius of curvature, q the secondary charge and B the magnetic field modulus.
So we have for the secondary charged 3-momentum:

$$P = \frac{qBR_{Reco}}{\sin\theta} \tag{5.5}$$

Substituting the last expression into the right-hand-side of equation [**?**], we can express the secondary charged 3-momentum in terms of the curvature k and the $\cot\theta$:

$$P^2 = \frac{B}{k} \cdot [1 + (\cot\theta)^2]^{1/2}$$

Now, the error on σ_P will be given by:

$$\sigma_P^2 = (\frac{\partial P}{\partial k} \cdot \sigma_k)^2 + (\frac{\partial P}{\partial \cot\theta} \cdot \sigma_{\cot\theta})^2 + 2\frac{\partial P}{\partial k}\frac{\partial P}{\partial \cot\theta} \cdot \sigma_{k\ \cot\theta} \tag{5.6}$$

where

$$\begin{aligned} \frac{\partial P}{\partial k} \cdot \sigma_k &= -\frac{B}{k^2} \cdot [1 + (\cot\theta)^2]^{1/2} \\ \frac{\partial P}{\partial \cot\theta} \cdot \sigma_{\cot\theta} &= \frac{B}{k} \cdot \frac{\cot\theta}{\sqrt{1 + (\cot\theta)^2}} \end{aligned}$$

and $\sigma_{k\ \cot\theta}$ is the covariance between k and $\cot\theta$.
Equation [**?**], together with equations [**?**] and [**?**], allows to calculate the error on the secondary charged squared mass propagated from the reconstruction matrix $\sigma_{m^2}^{Reco}$.

The last variable (s_0^{CM}) is constructed starting from the Lorentz-invariant quantities:

$$s_i = (P_K - P_i)^2 = (m_K - m_i)^2 - 2m_K T_i \tag{5.7}$$

being P_K the charged kaon 4-momentum and P_i (where $i = 1, 2, 3, 4$) is the i^{th} secondary particle 4-momentum. So that

$$s_0 = \frac{1}{3}\sum s_i = \frac{1}{3}[m_K^2 + 2m_{\pi^0}^2 + (P_e - P_\nu)^2] \tag{5.8}$$

which by the substitution $(P_e - P_\nu)^2 \simeq 2(E_e E\nu - \overrightarrow{P}_{sec}\overrightarrow{P}_\nu)$ gives:

$$s_0 = \frac{1}{3}[m_K^2 + 2m_{\pi^0}^2 + (2E_{sec}E_\nu - \overrightarrow{P}_{sec}\overrightarrow{P}_\nu)]$$

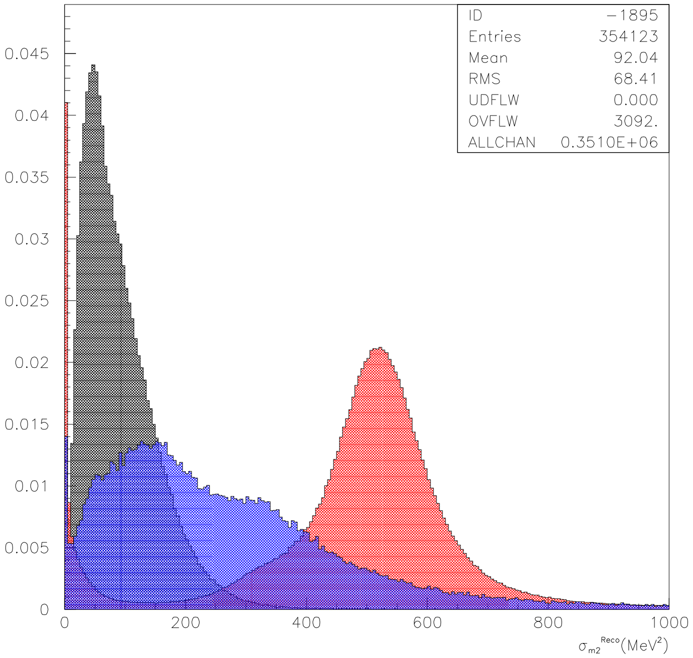

Figure 5.2: The $\sigma_{m^2}^{Reco}$ distribution for signal (black), $K_{\pi 3}^{00}$ (red) and K_{e3} background (blue) after the track-to-cluster association.

In the end of the previous section we shown how the background is rejected and a final sample is selected. Now it is possible to fit (making use of a ROOT fitting routine) the three variables discussed above in order to evaluate the remaining background on data and measure the Branching Ratio. However the signal efficiency is quite small, so it would be better to perform the Branching Ratio measurement at different value of the signal efficiency (and thus at different signal purity percentage too).

With this purpose in mind, we construct different sample with different selection efficiency for the signal varying the cuts on R_1. The measurement method then consist into measure the K_{e4}^{00} Branching Ratio at each signal efficiency level fitting the number of events for signal and backgrounds on data looking at $\sigma_{m^2}^{Reco}$, P_{sec} and the s_0^{CM} distributions.

The results obtained at each signal efficiency level by the three indipendent fits are combined by using a least-square estimator.

So we considered seven different couple of cuts on R_1 and R_2 corresponding to seven different sample with different signal efficiency and purity (see table [**?**] for details) and fitted the three distribution discussed in the beginning of the present section.

In the following figure are shown the P_{sec}, $\sigma_{m^2}^{Reco}$ and s_0 distribution for signal and backgrounds on Monte Carlo for each signal efficiency and purity sample. After the

cuts to reject background, it comes out that it's not always possible to fit the three shapes (signal, K_{e4}^{00} background and K_{e3} background) separately, so the fit procedure has been tuned in order to take into account similarities between signal and background shapes.
Thus for P_{sec} and s_0 distributions we fit Signal $+ K_{e3}$ and $K_{\pi3}^{00}$ shape in order to estimate Signal $+ K_{e3}$ and $K_{\pi3}^{00}$ fractions, while for the $\sigma_{m^2}^{Reco}$ distribution we fit Signal and

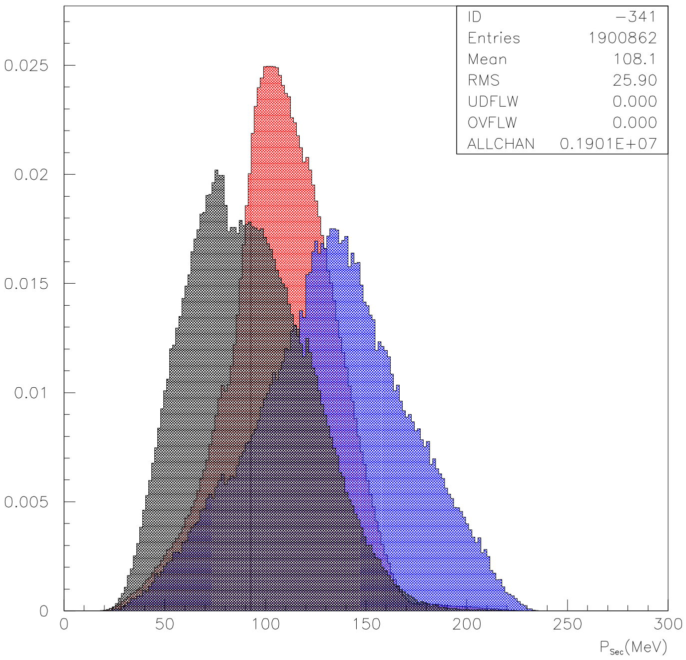

Figure 5.3: The P_{sec} distribution for signal (black), $K_{\pi3}^{00}$ (red) and K_{e3} background (blue) after the track-to-cluster association.

Purity (MC)	Signal Efficiency (MC)	R_1 cut	R_2 cut	$K_{\pi3}^{00}$ % (MC)	K_{e3} % (MC)
36 %	3.35 %	1	100	53 %	11 %
47 %	3.1 %	6	100	40 %	13 %
63 %	2.1 %	100	100	26 %	11 %
69 %	1.6 %	200	100	21 %	10 %
70 %	1.4 %	250	100	20 %	10 %
73 %	1.2 %	350	100	18 %	9 %
61 %	2.3 %	75	100	27 %	12 %

Table 5.1: Signal and background fractions at each signal efficiency and purity point, selected by varyng the cuts on R_1. The last point is the reference sample obtained by imposing the optimized cut on R_1 and R_2 discussed in the previous section.

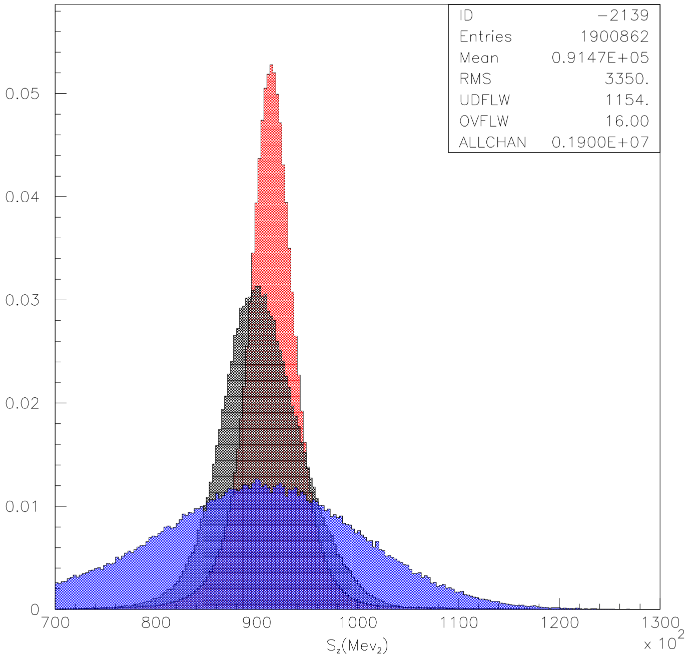

Figure 5.4: The s_0^{CM} distribution for signal (black), $K_{\pi 3}^{00}$ (red) and K_{e3} background (blue) after the track-to-cluster association.

$K_{\pi 3}^{00} + K_{e3}$ shape.

As we said, the three fit results of each signal efficiency and purity point are combined by means of a least-square estimator (see appendix [**?**]). When the dependence on parameters is linear, such in this case, the minimum χ^2 can be analytically solved and is given by, in matrix form:

$$\chi^2 = (y^{mis} - A\theta)^T V^{-1} (y^{mis} - A\theta)$$

where y^{mis} is the vector of measured values, θ is the array of the fit parameters and A is the matrix of differential derivatives, defined as

$$A_{ij} = \frac{\partial \lambda(x_i; \theta_j)}{\partial \theta_j}$$

where

$$\lambda(x_i; \theta_j) = \sum_{j=1}^{m} a_j(x)\theta_j$$

with $a_j(x)$ linearly independent functions of the variable x.
The parameters corresponding to the minimum χ^2 are given by the following array

$$\hat{\theta} = (A^T W A)^{-1} A^T W y^{mis}$$

where W is the inverse covariace matrix. The errors array on parameters corresponding to the minimum χ^2 is given by:

$$U = (A^T W A)^{-1}$$

Once the signal and background fractions are known, the relative Branching Ratio of $K^{00}e4$ events normalised to $K^{00}\pi 3$ can be computed by the following formula:

$$\frac{BR(K^{\pm} \rightarrow \pi^0\pi^0 e^{\pm}\nu_e(\overline{\nu}_e))}{BR(K^{\pm} \rightarrow \pi^0\pi^0\pi^{\pm})} = \frac{N^{Obs}_{K^{00}_{e4}}}{N^{Obs}_{K^{00}_{\pi 3}}} \cdot \frac{\epsilon_{K^{00}_{\pi 3}}}{\epsilon_{K^{00}_{e4}}} \tag{5.9}$$

where $N^{Obs}_{K^{00}_{e4}}$ e $N^{Obs}_{K^{00}_{\pi 3}}$ are the number of events observed on data respectively for the signal and for $K^{00}\pi 3$ decay (for details on the normalization sample selection see next section), $\epsilon_{K^{00}_{\pi 3}}$ and $\epsilon_{K^{00}_{e4}}$ represent the total selection efficiency, estimated on Monte Carlo. For each signal efficiency and purity sample selected as described above, the appropriate number of events (given by the least-squares estimator) and Monte Carlo efficiency is considered and the Branching Ratio measuremet for that point is obtained (see table [**?**]).

Signal Eff.	Signal %	$K^{00}_{\pi 3}$ %	K_{e3} %	Tot. events (Data)	BR	Rel. error
3.35 %	37 %	53 %	10 %	7371	2.92±0.19	7 %
3.1 %	48 %	44 %	8 %	5336	2.91±0.16	6 %
2.1 %	62 %	32 %	6 %	2510	2.68±0.14	5 %
1.6 %	62 %	28 %	10 %	1796	2.42±0.17	7 %
1.4 %	63 %	26 %	11 %	1571	2.36±0.17	7 %
1.2 %	67 %	24 %	9 %	1259	2.54±0.18	7 %
2.3 %	59 %	35 %	5 %	2775	2.61±0.14	5 %

Table 5.2: Signal and background fractions, as returned by the least-squares estimator, together with Branching Ratio measuremet at each signal efficiency and purity point are listed. The last point is the reference sample obtained by imposing the optimized cut on R_1 and R_2 discussed in the previous section.

5.3.1 The choice of the normalization sample

The normalization sample has been selected asking:

$$R_1 > 1 \cdot 10^{-14} \tag{5.10}$$

$$R_2 > 100 \tag{5.11}$$

that allows to obtain a normalization sample of $K^{00}_{\pi 3}$ events with a purity of 99.4 %. The number of $K^{00}\pi 3$ events to which we normalize, obtained on data, is thus:

$$N^{Obs}_{K^{00}\pi 3} = 875959 \tag{5.12}$$

the Monte Carlo efficiency is:

$$\epsilon^{MC}_{K^{00}\pi 3} = 0.015528 \tag{5.13}$$

while the Branching Ratio value used for the normalization sample is the one quoted by PDG (2008):

$$BR^{PDG}_{K^{00}\pi 3} = 0.01761 \tag{5.14}$$

5.4 Systematic checks

Now it is possible to estimate the systematic effect due to sample efficiency and purity by considering the standard deviation of all statistical significant Branching Ratio measurements listed in table [**?**], with the significance defined as:

$$\frac{\Delta^i_{BR}}{\sqrt{|\sigma^2_{Ref} - \sigma^2_i|}} \tag{5.15}$$

where Δ^i_{BR} is the difference between the reference Branching Ratio and the i^{th} obtained by varying the cut on R_1:

$$\Delta^i_{BR} = BR_{Ref} - BR_i. \tag{5.16}$$

Conventionally, a significance greater than 1.5 between two measurements indicates a non negligible systematic effect to be considered.

Nevertheless there is one more source of systematic effect that has to be taken into account, the one due to background subtraction techinque.
Indeed we shown in the previuos section how the actual signal and background fractions can be estimated by fitting some siutable variables on data, but it is possible to perform the Branching Ratio measurement simply subtracting to the number of events observed on data the amount of background predicted by the Monte Carlo simulation. So this Branching Ratio measuremnt has to be actually considered and, if statistically significant in the sense described above, included into the standard deviation evaluation of all statistical significant Branching Ratio measurements.

In order to evaluate the systematic effect due to the background subtraction technique, let us compute the Branching Ratio given by Monte Carlo formal background subtraction:

$$N^{Signal} = N^{Obs} - N^{K^{00}\pi3}_{Bck} - N^{Ke3}_{Bck}$$

where $N^{K^{00}\pi3}_{Bck}$ represent the number of $K^{00}\pi3$ events on Monte Carlo, N^{Ke3}_{Bck} represent the number of K_{e3} events in the Monte Carlo simulation, both scaled by the luminosity factor

$$L^{Bhabha}_{MC}/L^{Bhabha}_{Data} = 0.8847$$

Besides, it is possible that the Monte Carlo simulation does not correctly reconstructs the $K^{00}\pi3$ events surviving the rejection criteria of the Likelihood Ratio procedure, being (as discussed in the end of the previous section) a particular population of

$K^{00}\pi3$: the ones in which the secondary charged particle has been wrongly associated to a photon cluster into the electromagnetic calorimeter.
So would be higly preferable to have a way to correct the Monte Carlo prediction for the background normalization events. As anticipated in the end of the previous section, it is possible to utilize the peculiar structure shown by the secondary charged β distribution for $K^{00}\pi3$ events in order to estimate the number of such events directly on data.
Thus the actual number of remaining $K^{00}\pi3$ events is given by:

$$N^{K^{00}\pi3}_{Bck-Corr} = (N^{K^{00}\pi3}_{\beta(-1)} \cdot K^{K^{00}\pi3}_{MC} \cdot K^{Corr}_{Data-MC}) - N^{K^{00}\pi3}_{\beta(-1)} \tag{5.17}$$

where $N^{K^{00}\pi3}_{\beta(-1)}$ is the $K^{00}\pi3$ events number of the $\beta \approx -1$ population on Monte Carlo, $K^{K^{00}\pi3}_{MC}$ is the proportionality factor between $K^{00}\pi3$ population at $\beta \approx -1$ and the $K^{00}\pi3$ population at $\beta \approx 1$ on Monte Carlo and $K^{Corr}_{Data-MC}$ is the Data-MC correction factor (refer to figure [**?**]).
We get:

$$\begin{aligned} N^{K^{00}\pi3}_{\beta(-1)} &= 86 \\ K^{K^{00}\pi3}_{MC} &= 8.61 \\ K^{Corr}_{Data-MC} &= 1.23 \end{aligned}$$

which gives

$$N^{K^{00}\pi3}_{Bck-Corr} = 932 \tag{5.18}$$

so that

$$N^{Signal} = N^{Obs} - N^{K^{00}\pi3}_{Bck} - N^{Ke3}_{Bck} = 2775 - 932 - 269 = 1574 \pm 53$$

From equation (5.9) we can calculate the Branching Ratio given by Monte Carlo formal background subtraction with the $K^{00}\pi3$ contribution corrected as discussed above:

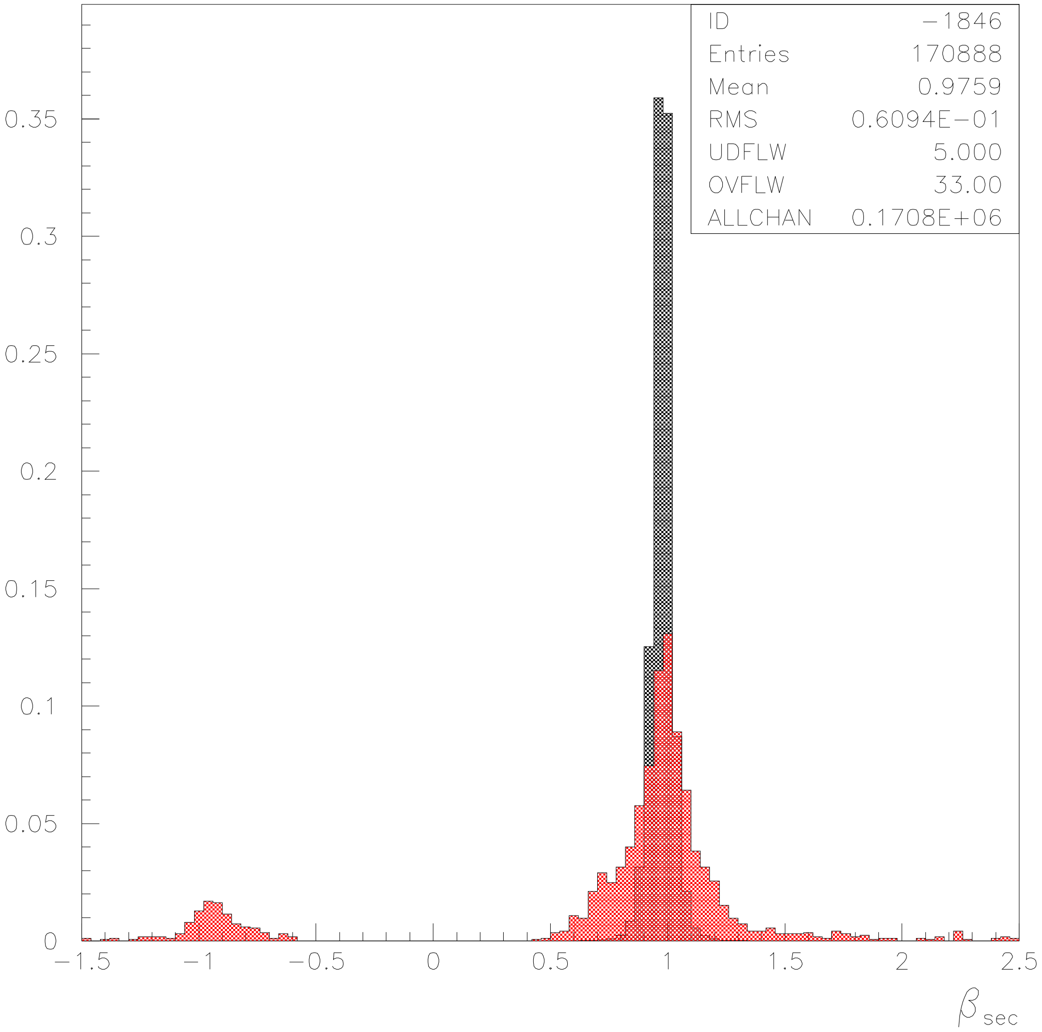

Figure 5.5: The secondary charged β distribution for signal (black) and normalization events (red) after the cuts on R_1 and R_2. It is possible to note a population for negative β value constituted only by residual normalization events at $\beta \approx -1$ and indicated by $N^{K^{00}\pi3}_{\beta(-1)}$. The proportionality factor between the $K^{00}\pi3$ events in the $\beta \approx 1$ region and $N^{K^{00}\pi3}_{\beta(-1)}$ is indicated by $K^{K^{00}\pi3}_{MC}$.

$$BR_{MC}(K^{\pm} \rightarrow \pi^0\pi^0 e^{\pm}\nu_e(\overline{\nu}_e)) = 2.72 \pm 0.08 \cdot 10^{-5}$$

Now we can update the measuremets table by including, in the second-last line of table [**?**], the Branching Ratio just obtained. The systematic error is computed by calculating the standard deviation of all the significant measurements:

$$\sigma_{Syst.} = 2.4 \cdot 10^{-6}$$

The total error will bi given by

$$\sigma_{Tot} = \sqrt{\sigma^2_{Stat.} + \sigma^2_{Syst.}} = 2.8 \cdot 10^{-6}$$

where $\sigma_{Stat.}$ is the one of the reference Branching Ratio measurement, reported in the last point of table [**?**].

So the final result for the $K^{\pm} \rightarrow \pi^0\pi^0 e^{\pm}\nu_e(\overline{\nu_e})$ (K^{00}_{e4}) Branching Ratio measurement obtained is:

$$BR(K^{\pm} \rightarrow \pi^0\pi^0 e^{\pm}\nu_e(\overline{\nu}_e)) = 2.61 \pm 0.28 \cdot 10^{-5}$$

with a relative error of $\sim 10.6\,\%$.

Purity (MC)	Signal Efficiency (MC)	BR	Significance
36 %	3.35 %	2.92±0.19	2.31
47 %	3.1 %	2.91±0.16	3.84
63 %	2.1 %	2.68±0.14	5.03
69 %	1.6 %	2.42±0.17	2.26
70 %	1.4 %	2.36±0.17	2.65
73 %	1.2 %	2.54±0.18	0.6
61 %	2.3 %	2.72±0.08	0.89
61 %	2.3 %	2.61±0.14	-

Table 5.3: Branching Ratio measurement at each signal efficiency and purity point, selected by varyng the cuts on R_1. In the second-last point Branching Ratio measurement obtained by formal Monte Carlo background subtraction, with the $K^{00}\pi 3$ contribution corrected, is reported. The last point is the reference measuremet obtained by imposing the optimized cut on R_1 and R_2 discussed in the previous section.

5.5 Efficiency evaluation

The total selection efficiency for the signal and for the normalization sample can be write as follow:

$$\epsilon_{K^{00}_{e4}} = \epsilon_{Trig.} \cdot \epsilon_{Evcl} \cdot \epsilon_{Ric} \cdot \epsilon_{4\gamma} \cdot \epsilon_{TCA} \cdot \epsilon_{R_1R_2}$$
$$\epsilon_{K^{00}_{\pi 3}} = \epsilon^{'}_{Trig.} \cdot \epsilon^{'}_{Evcl} \cdot \epsilon^{'}_{Ric} \cdot \epsilon^{'}_{4\gamma} \cdot \epsilon^{'}_{TCA} \cdot \epsilon^{'}_{R_1R_2}$$

where:

- $\epsilon_{Trig.}$ and $\epsilon^{'}_{Trig.}$ are the trigger efficiency for signal and normalization sample respectively.

- ϵ_{Evcl} and $\epsilon^{'}_{Evcl}$ are the efficiencies of the event classification algorithm for signal and normalization sample respectively.

- ϵ_{Ric} and $\epsilon^{'}_{Ric}$ are the charged vertex reconstruction efficiencies for signal and normalization sample respectively.

- $\epsilon_{4\gamma}$ and $\epsilon^{'}_{4\gamma}$ are the neutral vertex efficiency for signal and normalization sample respectively.

- ϵ_{TCA} and $\epsilon^{'}_{TCA}$ are the track-to-cluster association efficiency for signal and normalization sample respectively.

- $\epsilon_{R_1R_2}$ and $\epsilon^{'}_{R_1R_2}$ are the efficiency of the cuts on the variables R_1 and R_2 returned by the Lielihood Ratio procedure for signal and normalization sample respectively.

The first four contributions to the total selection efficiency are expected to be equal for signal and normalization sample. Indeed the choice of measure a relative Branching Ratio normalized to $K^{00}\pi3$ guarantees a cancellation of most os sytematic effects due to reconstruction, given the similarities among the signal and the normalization channels (as shown by the secondary charged 3-momentum distribution for signal and nromalization, see figures [**?**]).

In figures [**?**] is shown the product of the firts four contributions to the total selection efficiency as a function of the secondary charged transverse 3-momentum $p_T = \sqrt{p_x^2 + p_y^2}$ for signal (blue) and normalization sample (red), in figure [**?**] is shown the MC ratio for signal and normalization sample efficiency and in figure [**?**] Data-MC ratio.

The track-to-cluster (TCA) efficiency is defined as

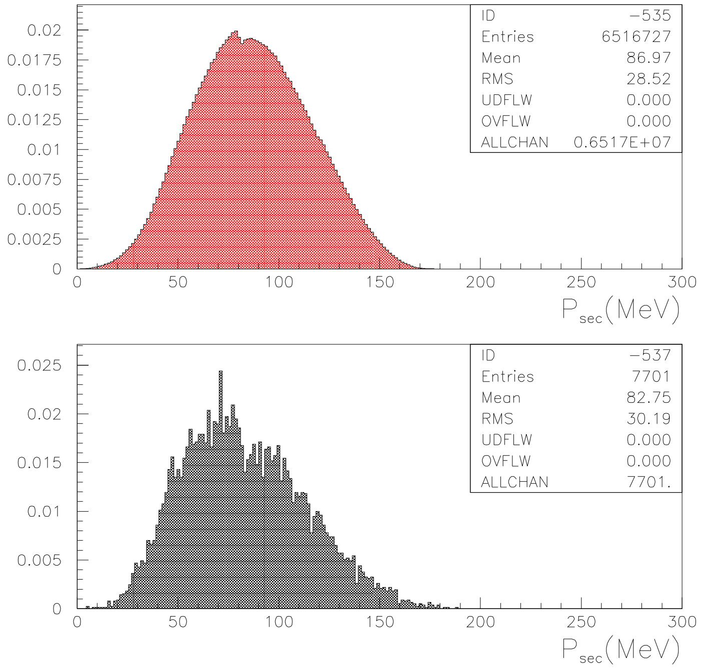

Figure 5.6: Secondary charged 3-momentum distribution for $K^{00}\pi3$ events (red) and signal (black).

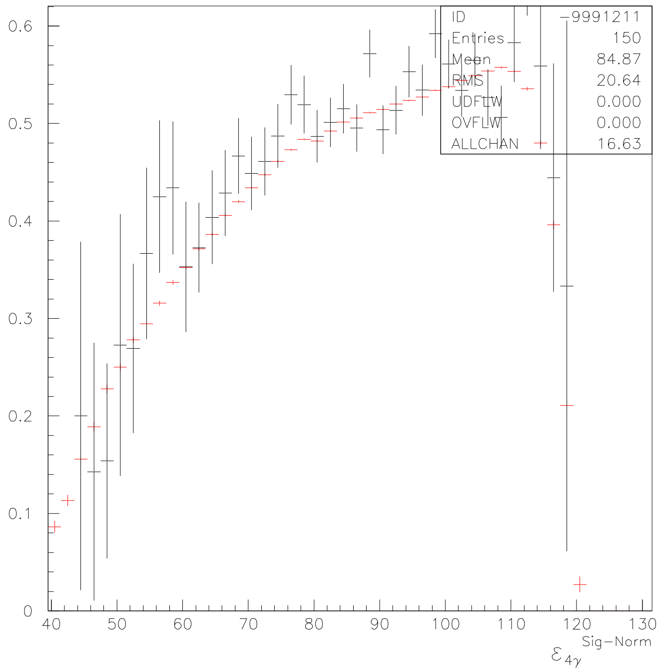

Figure 5.7: Product of the four contributions to the total selection efficiency as a function of the secondary charged transverse 3-momentum for signal events (black) and normalization sample events (red).

$$\epsilon_{TCA} = \frac{N_{TCA}}{N_{Vtx-4\gamma}}$$

where $N_{Vtx-4\gamma}$ are the events in which a neutral vertex with four photons (two neutral pions) has been reconstructed and N_{TCA} are events for which the secondary charged particle has been associated to a cluster into the electromagnetic calorimeter.

The efficiency ϵ_{TCA} and $\epsilon^{'}_{TCA}$, for signal and normalization sample respectively, are expected to be different for the two channels, becouse of the different nature of the secondary charged particle for signal and normalization.

In order estimate possibly Data-MC corrections for such efficiencies we have to select a pure sample of pions coming from $K^{00}\pi3$ events and of electrons for the signal on data and compare the Data TCA efficiency as a function of the secondary charged 3-momentum with the one predicted by the Monte Carlo simulation.

The signal selection strategy already provide a pure sample of $K^{00}\pi3$ events, indeed after a neutral vertex has been found $\sim 94\,\%$ of the events observed are constituted by $K^{00}\pi3$ events. So that it is possible to use such sample to estimate on data the TCA efficiency for the normalization sample as a function of the charged secondary

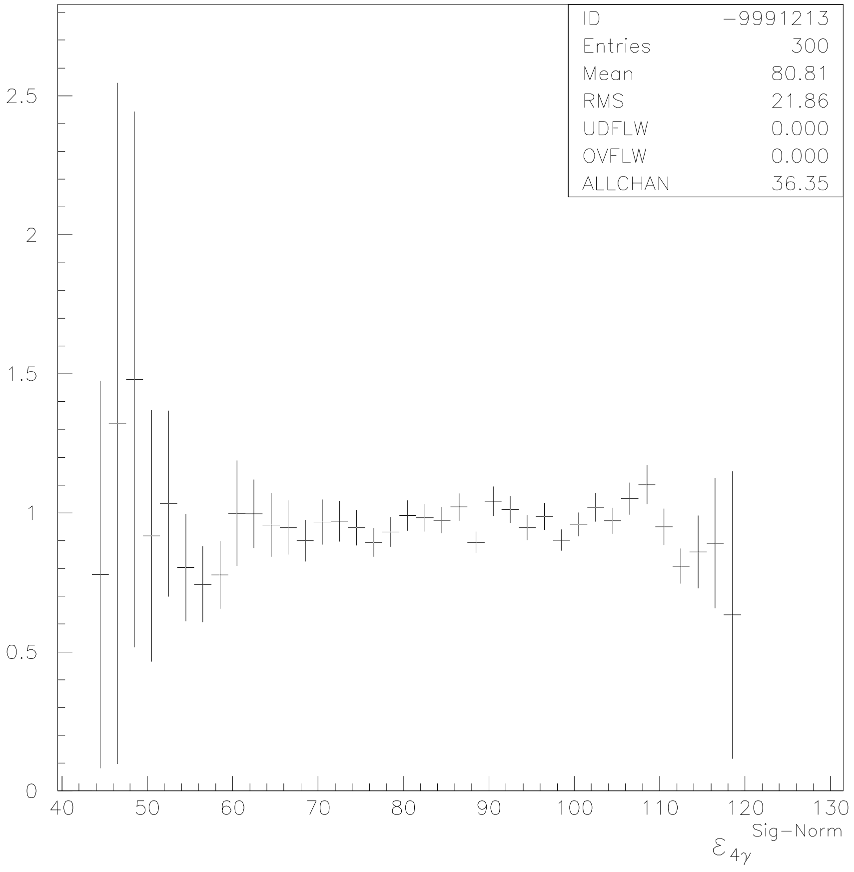

Figure 5.8: Signal and normalization sample efficiency ratio on MC for the product of the first four contributions to the total selection efficiency as a function of the secondary charged transverse 3-momentum.

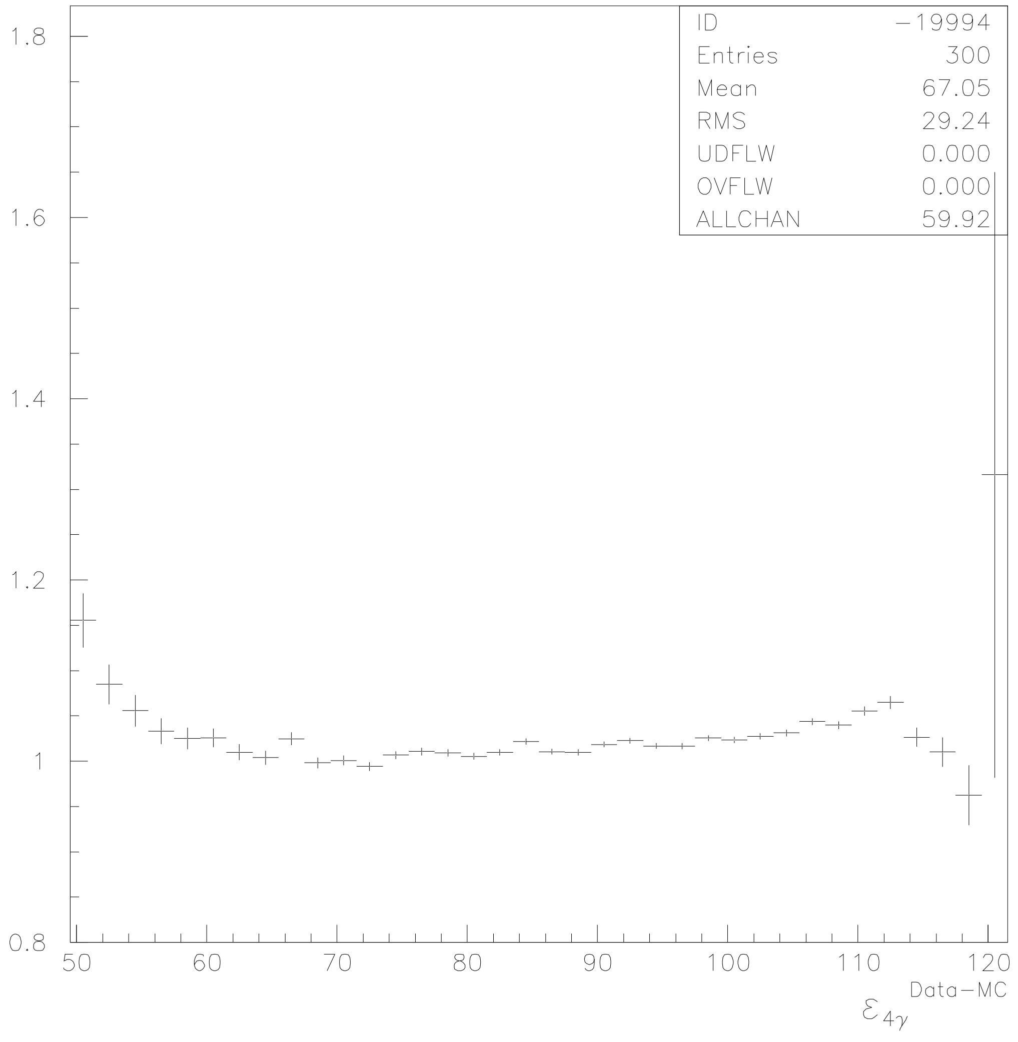

Figure 5.9: Efficiency Data-MC ratio for the product of the first four contributions to the total selection efficiency as a function of the secondary charged transverse 3-momentum.

3-momentum, see figures [**?**].

For what concerns signal events, which are too rare to be selected without using the calorimeter informations provided by the TCA procedures, the evaluation of the track-to-cluster efficiency for Data and MC can be performed considering K_{e3} events, which represent a large electrons source similar to that of the signal, for secondary charged electrons from K_{e3} have 3-momentum comparable with the signal ones.

So a $\sim 86\,\%$ pure sample of K_{e3} events has been selected in the following way:

1. Starting from the events classification algorithm informations, we require a $\phi \to K^+K^-$ identificated by KPM stream algorithm.
2. Then we search for a $K^\pm$ track plus vertex in the drift chamber.
3. Events with one π^0 in the final state are selected using the neutral vertex tecnique.
4. Kinematic background rejection.

In figure [**?**] TCA efficiency for the K_{e3} sample as a function of the charged secondary 3-momentum is shown.

From figures [**?**] and [**?**] it is evident that the TCA contributions for electrons ϵ_{TCA} and pions $\epsilon^{'}_{TCA}$ to total efficiency has to be corrected. The Data-MC correction to apply has been evaluated taking into account the complete efficiency shape. We obtained:

$$\frac{\epsilon^{'}_{TCA}}{\epsilon_{TCA}} = 0.1511 \tag{5.19}$$

All the Branching Ratio measurements performed in the previous section, obtained using formula [**?**], have been corrected by this factor.

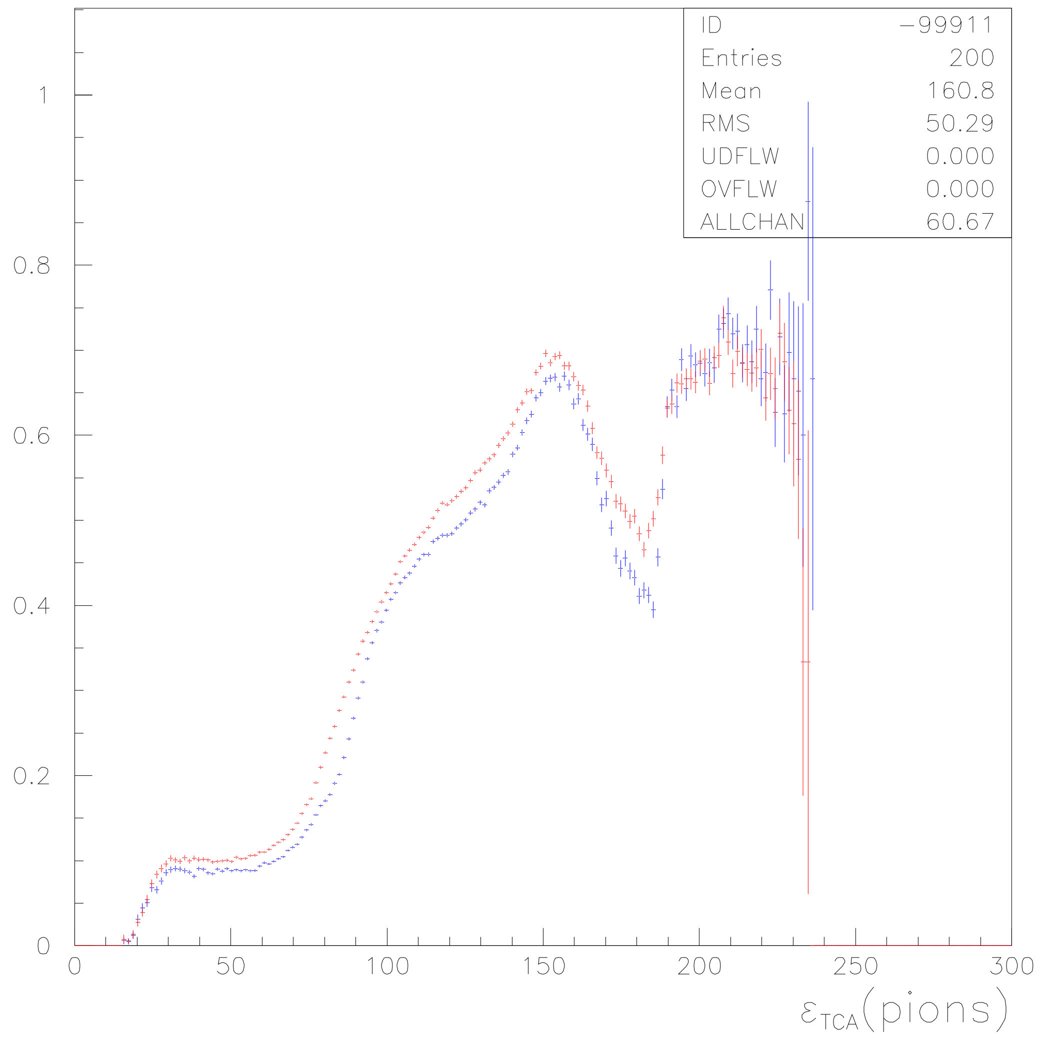

Figure 5.10: TCA Data-Mc efficiency comparison for $K^{00}\pi3$ events of the normalization sample as a function of the charged secondary 3-momentum for Data (red) and MC (blue).

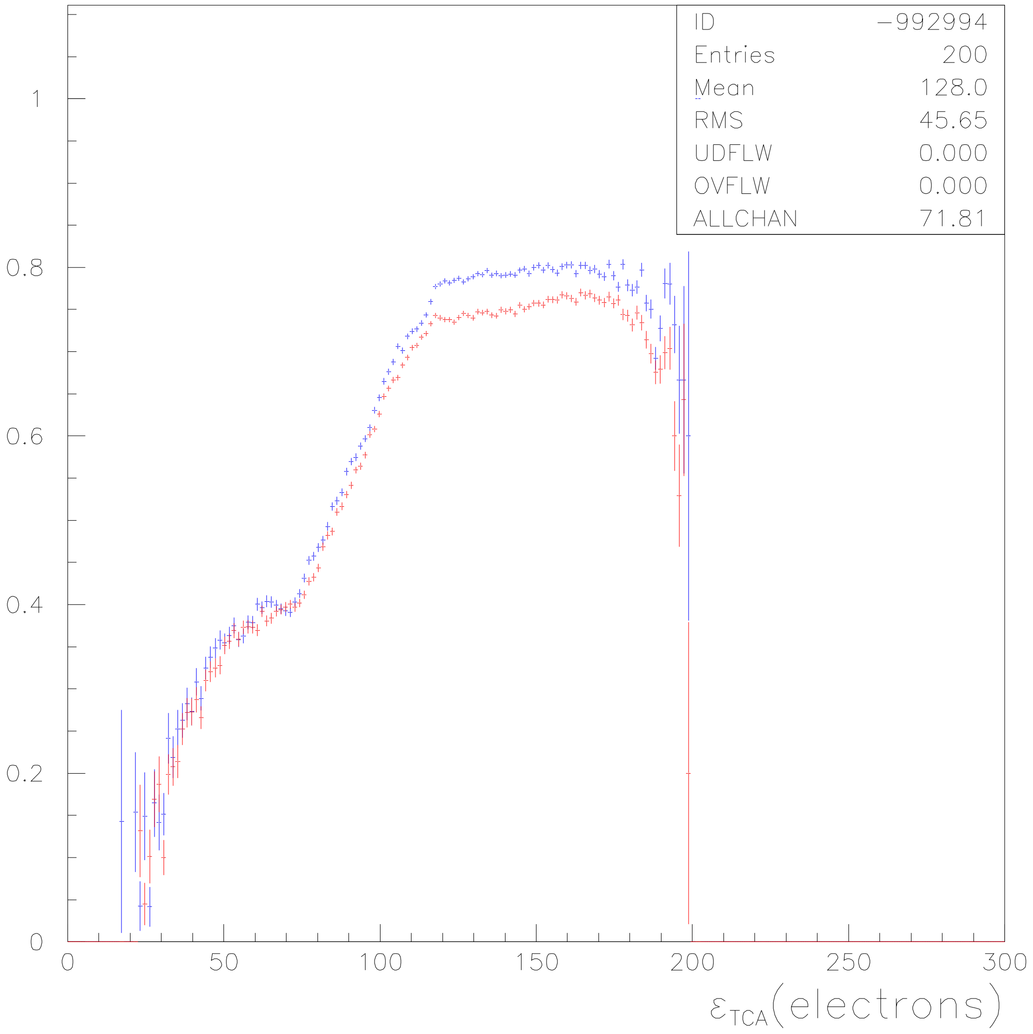

Figure 5.11: TCA Data- MC efficiency comparison for $Ke3$ events as a function of the charged secondary 3-momentum for Data (red) and MC (blue).

5.6 Form factor estimation

By using equation [**?**], reported here:

$$\Gamma((K^{00}l4)) = 0.8 \cdot |V_{us}|^2 |F|^2 \cdot 10^3 sec^{-1} \tag{5.20}$$

the form factor can be evaluated, we get:

$$F = 8.0 \pm 0.4$$

where we used $V_{us} = 0.2255$. The result obtained for the form factor is in agreement with the one quoted at by Barmin [11] (1988) 7.3 ± 1.3.

Conclusions

We have done a measurement of the $K^{\pm} \rightarrow \pi^0\pi^0 e^{\pm}\nu_e(\overline{\nu_e})$ BR normalised to $K^{\pm} \rightarrow \pi^0\pi^0\pi^{\pm}$ ($\tau`$) events using the whole data sample collected by KLOE $\sim 1212\, pb^{-1}$. We obtained

$$BR(K^{\pm} \rightarrow \pi^0\pi^0 e^{\pm}\nu_e(\overline{\nu_e})) = 2.61 \pm 0.28 \cdot 10^{-5}$$

with a relative error of $\sim 10.6\,\%$.
This result has to be compared with the one quoted by PDG (2008) ($2.2 \pm 0.4 \cdot 10^{-5}$), affected by a relative error of $\sim 18\,\%$, so that the result obtained comes out with a relative error almost cut by half.
The form factor evaluated

$$F = 8.0 \pm 0.4$$

(using $V_{us} = 0.2255$) is in agreement with the one quoted at by Barmin [11] (1988) 7.3 ± 1.3.

Appendix A

The kinematic fit procedure

Suppose we have N experimental independent measurement $\underline{y} = (y_1, y_2, ..., y_N)$ e un insieme di J variabili non misurate $\underline{\xi} = (\xi_1, \xi_2, ..., \xi_J)$.
Let us indicate with $\underline{\eta} = (\eta_1, \eta_2, ..., \eta_N)$ the true measurements value $\underline{y}$, not known, and with V their variance-covariace matrix that, in the case of independent measurements, will be diagonal.
All the variables are correlated by K constraint equations:

$$f_k(\eta_1, \eta_2, ..., \eta_N, \xi_1, \xi_2, ..., \xi_J) = 0, \qquad k = 1, 2, ..., K \tag{5.21}$$

It is clear that the measurements $\underline{y}$ can not strictly satisfy the constraints, being affected by experimental uncertainty, while the final true value estimations $\underline{\hat{\eta}}$, named fitted variables, have to necessarily satisfy the constraints.
The Lagrange multipliers method allows to solve the minimization problem where the variables are related by algebraic constraints by adding for each constraint a parameter, named Lagrange multiplier, with respect to which perform the minimization. In such a way the problem of searching the fitted variables is brought to a χ^2 minimization procedure.

Let us introduce an additional set of not known parameters $\underline{\lambda} = (\lambda_1, \lambda_2, ..., \lambda_N)$ for the K constraint equation and minimize the following χ^2:

$$\chi^2(\underline{\eta}, \underline{\xi}, \underline{\lambda}) = (\underline{y} - \underline{\eta})^T V^{-1} (\underline{y} - \underline{\eta}) + 2\underline{\lambda}^T \underline{f}(\underline{\eta},)\underline{\xi}$$

where the total parameters number will be now $N + J + K$.
Let us now put to zero the derivatives respect to the parameters and find the minimum χ^2:

$$\begin{array}{lll} \nabla_\eta \chi^2 = -2V^{-1}(\underline{y} - \underline{\eta}) + 2F_\eta^T \underline{\lambda} & = 0 & \text{(N equations)} \\ \nabla_\xi \chi^2 = 2F_\xi^T \underline{\lambda} & = 0 & \text{(J equations)} \\ \nabla_\lambda \chi^2 = 2\underline{f}(\underline{\eta}, \underline{\xi}) & = 0 & \text{(K equations)} \end{array} \tag{5.22}$$

the matrix F_η (dimension $K \times N$) and F_ξ (dimension $K \times J$) are defined as:

$$(F_\eta)_{ki} \equiv \frac{\partial f_k}{\partial \eta_i}, \qquad (F_\xi)_{kj} \equiv \frac{\partial f_k}{\partial \xi_j} \tag{5.23}$$

When the constraint equation are not linear in the parameters, to get the system (5.22) solution it is necessary to resort to recursive approximations method.
Suppose we have performed ν iterations, the $\nu - th$ iteration will have an approximate solution given by $\underline{\eta}^\nu, \underline{\xi}^\nu, \underline{\lambda}^\nu$.
It is possible to make a Taylor first order approxiamtion of the constraint equation in the point $(\underline{\eta}^\nu, \underline{\xi}^\nu)$:

$$f^\nu + F_\eta^\nu(\underline{\eta}^{\nu+1} - \underline{\eta}^\nu) + F_\xi^\nu(\underline{\xi}^{\nu+1} - \underline{\xi}^\nu) = 0 \tag{5.24}$$

where f, F_η^ν and F_ξ^ν are the finctions defined by equations (5.21) and (5.23) respectively and are evaluated in the point $(\underline{\eta}^\nu, \underline{\xi}^\nu)$.
The equation (5.24), together with the firts two in (5.22), allows to obtain the variables value for $\underline{\xi}^{\nu+1}$,the Lagrange multipliers $\underline{\lambda}^{\nu+1}$ and the fitted variables $\underline{\eta}^{\nu+1}$, indeed we have:

$$\begin{aligned} \underline{\xi}^{\nu+1} &= \underline{\xi}^\nu - (F_\xi^T s^{-1} F_\xi)^{-1} F_\xi^T s^{-1} \underline{r} \\ \underline{\lambda}^{\nu+1} &= s^{-1}[\underline{r} + F_\xi(\underline{\xi}^{\nu+1} - \underline{\xi}^\nu)] \\ \underline{\eta}^{\nu+1} &= \underline{y} - V F_\eta^T \underline{\lambda}^{\nu+1} \end{aligned}$$

where the following notations have been introduced:

$$\underline{r} \equiv f^\nu + F_\eta^\nu(\underline{y} - \underline{\eta}^\nu)$$

$$\underline{\mathrm{s}} \equiv F_\eta^\nu V (F_\eta^\nu)^T$$

Making use of the values $\underline{\eta}^{\nu+1}, \underline{\xi}^{\nu+1}, \underline{\lambda}^{\nu+1}$ it is possible to calculate the $\chi^2_{\nu+1}$ value for the $(\nu+1)-th$ iteration and compare it with the previous iteration χ^2_ν value.
This procedure is repeated until the χ^2 variation become lower than a parameter which represent the final solution accuracy.

Appendix B

Hypothesis test: The Likelihood Ratio Method

Let us consider the case we need to make a statement about how well the observed data stand in agreement with given predicted probabilities, i.e. hypothesis.
The hypothesis under consideration is usually called the null hypothesis, H_0, which specify a $f(x)$ probability density finction (p.d.f.) for a random variable x and we want to make a statement about the validity of H_0 when compared with some alternative hypotheses $H_1, H_2, ...$ etc.
So suppose we have a set of n measured values $\mathbf{x} = (\mathbf{x_1}, ..., \mathbf{x_n})$ (for examples n repeated observations af the same random variable) and a set of hypotheses $H_0, H_1, ...$ each of which specifies a given joint p.d.f. $f(x|H_0), f(x|H_1), ...$, we want to investigate the measure of agreement between the observed data and a given hypothesis. This can be done by constructing a test statistic t so that each of the hypotheses will imply a fived p.d.f. for the statistic t, let us call such statistics for the hypotheses $H_1, H_2, ...$ as $g(t|H_0), g(t|H_1), ...$
Let us suppose that we have chosen a scalar function $t(x)$ which has the p.d.f. $g(t|H_0)$ if H_0 is true and $g(t|H_1)$ if H_1 is true. The compatibility statement between the data and the various hypotheses is formulated in terms af a decision to accept or reject a given null hypothesis H_0. This can be done by defining a critical region (whose complement is named acceptance region) for t, if the valueof t actually observed is in the critical region, one reject the hypothesis H_0, otherwise H_0 is accepted.

The critical region is defined such that the probability for t to be observed there, under assumption of the hypothesis H_0, is some value α called the significance level of the test. So the critical region could consist of values of t greater then a certain value t_{cut} and the significance level is then

$$\alpha = \int_{t_{cut}}^{\infty} g(t|H_0)dt \tag{5.25}$$

The hypothesis H_0 then is accepted if the value of t observed is less than t_{cut}. Obiously there is a probability of α to reject H_0 true, this is called an error of first kind. An error of second kind occur if the hypothesis H_0 is accepted, so that t is observed less than t_{cut}, but the true hypothesis but rather some alternative hypothesis H_1. The probability for this to happen is

$$\beta = \int_{\infty}^{t_{cut}} g(t|H_1)dt \tag{5.26}$$

with $1-\beta$ called the power of the test to discriminate against the alternative hypothesis H_1.

The critical region can be chosen by means of the Neyman-Pearson Lemma. Indeed up to now the exact choice of the critical region, *i.e* the value of the cut t_{cut}, was left open. This will be chosen depending on the efficiency and purity af the selected particles (or events) desired on the further analysis. One way of defining an optimal placement of the cuts is to require that they give a maximum purity for a given efficiency.
There exists only a single cut value t_{cut} that determine both the efficiency and purity.

The Neyman-Pearson Lemma states that the region giving the highest power (and hence the highest signal purity) for a given significance level α (or selection efficiency $\epsilon = 1 - \alpha$) is the region such that:

$$\frac{g(t|H_0)}{g(t|H_1} > c \tag{5.27}$$

where c is a constant which is determined by the desired efficiency (the desired value of the efficiency is still left open and will be chosen depending ...).
Note that a test based on the Neyman-Pearson Lemma acceptance region is actually equivalent to a test using a one-dimensional statistic given by the ratio on the left-hand side of equation ([**?**]):

$$R = \frac{g(t|H_0)}{g(t|H_1} \tag{5.28}$$

This is called the Likelihood Ratio for hypotheses H_0 and H_1, the correspondig acceptance region is given by

$$R > c \tag{5.29}$$

Appendix C

Parameters estimation: The method of least squares

In many situations a mesured value y con be regarded as a gaussian random variable centered about the quantity's true value λ.

Suppose that the true value is given as a function of x, $\lambda = \lambda(x, \theta)$, which depends on unknown parameters $\theta = (\theta_1, ..., \theta_n)$. The aim of the method of the least squares is to estimate the parameters θ. In addition, the methods allows for a simple evaluation of the godness of fit of the hypothesized function $\lambda(x, \theta)$.
Although one can carry out the least squares procedure for aby funcion $\lambda(x, \theta)$, the resulting χ^2 value and least squares estimantor have particularly desiderable properties for the case where $\lambda(x, \theta)$ is a linear function of the parameters θ

$$\lambda(x, \theta) = \sum_{j=1}^{m} a_j(x)\theta_j$$

where $a_j(x)$ are any linearly independent functions of x. Note that what ios required is just that λ is linear in the parameters θ_j, then $a_j(x)$ are not in general linear in x, but are just linearly independent from each other.
For this case the estimators and their variances can be found analytically maximizing a χ^2 numerically, furthermore they have zero bias and minimum variance.
The value af the function $\lambda(x, \theta)$ at x_i can be written

$$\lambda(x_i, \theta) = \sum_{j=1}^{m} a_j(x_i)\theta_j = \sum_{j=1}^{m} A_{ij}$$

where

$$A_{ij} = a_j(x_i) = \frac{\partial \lambda(x_i, \theta)}{\partial \theta_j}$$

The general expression for the χ^2 can then be written in matri notaion as

$$\chi^2 = (y^{mis} - A\theta)^T V^{-1} (y^{mis} - A\theta)$$

where y^{mis} is the vector of measured values and is understood (together with θ) to be column vector with the superscript T indicating a transposed vector (*i.e.* a row).
To find the minimum χ^2 we set its derivatives with respect to the parameters θ_i equal to zero:

$$\chi^2 = -2(A^T V^{-1} y - A^T V^{-1} A\theta) = 0$$

providing the matrix $A^T V^{-1}$ is not singolar, this can be solved for the estimators $\hat{\theta}$

$$\hat{\theta} = (A^T W A)^{-1} A^T W y^{mis}$$

that is, the solutions $\hat{\theta}$ are linear functions of the original measurements y.
Using error propagation to find the covariance matrix for the estimators we get:

$$U = (A^T W A)^{-1}$$

Bibliography

[1] L.Maiani G.Pancheri N.Paver, *The DAΦNE physics handbook*, LNF, 1 (1995).

[2] L. B. Okun, *Lepton and Quarks*, North-Holland Publishing Company 1982.

[3] Nguyen Van Hieu, *Sov. Phys.*, JEPT 17 (1963) 113.

[4] N.Cabibbo and Masksymowicz, *Phys. Rev.*, 137 (1965) B438.

[5] A.Pais e S.B.Treiman; *Phys. Rev.*, 168 (1968) 1858.

[6] J.L. Basdevant, C.D. Froggat and J.L. Petersen, *Nucl. Phys.* B72 (1974) 413.

[7] J. Gasser and H.Leutwyler, *Phys. Lett.* B125 (1983) 321.

[8] F. Romano, P. Renton, B. Aubert and A. M. Burban-Lutz,*Phys. Lett.* B36 (1971) 525.

[9] D. Ljung and D. Cline, *Phys. Lett.* B125 (1973) 1307.

[10] V. N. Bolotov et al., *Sov. J. Nucl. Phys.* 44 (1986) 68.

[11] V. V. Barmin et al., *Sov. J. Nucl. Phys.* 48 (1988) 1032.

[12] F.A. Berends et al., *Phys. Lett.* B26 (1967) 109.

[13] K. Hagiwara et al., *Phys Rev.* D66, 010001 (2002).

[14] L. Rosselet et al., *Phys Rev.* D15, (1977) 574.

[15] S. Pislak et al., *Phys Rev.* D67, (2003) 095004.

[16] L. Rosselet et al., *Phys. Rev.* D15 (1977) 574.

[17] J. Bijnens, G. Colangelo, G. Ecker and J. Gasser, *The second DAΦNE handbook*, LNF, 1 (1995) 315.

[18] S. Eidelman *et al.* [Particle Data Group Collaboration], Phys. Lett. B **592** (2004) 1.

[19] S. Bertolucci et al., "The LADON test beam of EMCAL: a full report on the data analysis" KLOE note (62) (1993).

[20] A. Antonelli *et al.*, KLOE *note* (157) (1996).

[21] M. Incagli *et al.*, KLOE *memo* (147) (1996).

[22] K. W. Edwards *et al.*, Nucl. Instrum. Meth. A **252** (1986) 384.

[23] P. De Simone *et al.*, Ph.D. Thesis, Universitá degli studi di Roma "La Sapienza",(1994).

[24] W.-M. Yao *et al.* (Particle Data Group Collaboration) *Journal of Physics* **G 33, 1** 2006 W. M. Yao *et al.*, J. Phys. G. 33,1 (2006).

[25] M. Kobayashi and T. Maskawa, Prog. Theor. Phys. **49** (1973) 652.

[26] N. Cabibbo, Phys. Rev. Lett. **10** (1963) 531.

[27] L. L. Chau and W. Y. Keung, Phys. Rev. Lett. **53** (1984) 1802.

[28] L. Wolfenstein, Phys. Rev. Lett. **51** (1983) 1945.

[29] R. Kowalewski and T. Mannel [Particle Data Group Collaboration], Phys. Lett. B **867** (2006) 1.

[30] E. Blucher and W.J. Marciano [Particle Data Group Collaboration], Phys. Lett. B **677** (2006) 1.

[31] H. Leutwyler and M. Roos, Z. Phys. C **25** (1984) 91.

[32] A. Czarnecki, W.J. Marciano, Alberto Sirlin Phys. Rev. **D70:093006** 2004. [arXiv:hep-ph/0406324]

[33] A. Sirlin, Nucl. Phys. B **196** (1982) 83.

[34] V. Cirigliano, M. Knecht, H. Neufeld, H. Rupertsberger and P. Talavera, Eur. Phys. J. C **23** (2002) 121 [arXiv:hep-ph0110153].

[35] V. Cirigliano, H. Neufeld and H. Pichl, Eur. Phys. J. C **35** (2004) 53 [arXiv:hep-ph0401173].

[36] D. Becirevic *et al.*, [arXiv:hep-ph0403217].

[37] N. Cabibbo, E. C. Swallow and R. Winston, Ann. Rev. Nucl. Part. Sci. **53** (2003) 39 [arXiv:hep-ph/0307298].

[38] F. Mescia, for the KLOE collaboration, ICHEP 2004 presentation http://www.ihep.ac.cn/data/ichep04/ppt/8_cp/8-0811-antnoelli-m.pdf

[39] M. Palutan, for the KLOE collaboration, Kaon 2007 presentation http://www.lnf.infn.it/conference/kaon07/

[40] C. T. H. Davies *et al.* [HPQCD Collaboration], Phys. Rev. Lett. **92** (2004) 022001 [arXiv:hep-lat/0304004].

[41] W. J. Marciano and A. Sirlin, Phys. Rev. Lett. **71** (1993) 3629.

[42] W. J. Marciano and A. Sirlin, Phys. Rev. Lett. **56** (1986) 22.

[43] A. Sirlin, Rev. Mod. Phys. **50** (1978) 573 [Erratum-ibid. **50** (1978) 905].

[44] T. Kinoshita, Phys. Rev. Lett. **2** (1959) 477.

[45] M. Finkemeier, Phys. Lett. B **387** (1996) 391 [arXiv:hep-ph/9505434].

[46] K. Hagiwara *et al.* [Particle Data Group Collaboration], Phys. Rev. D **66** (2002) 010001.

[47] C. Aubin *et al.* [MILC Collaboration], arXiv:hep-lat/0409041.

[48] A. Czarnecki, W. J. Marciano and A. Sirlin, arXiv:hep-ph/0406324.

[49] I. H. Chiang, J. L. Rosen, S. Shapiro, R. Handler, S. Olsen and L. Pondrom, Phys. Rev. D **6** (1972) 1254.

[50] W.-M. Yao *et al.* (Particle Data Group Collaboration) *Journal of Physics* **G 33, 1** 2006 W. M. Yao *et al.*, J. Phys. G. 33,1 (2006).

[51] F. Lobkowicz *et al.* 1970. Phys.Rev.185:1676-1687,1969.

[52] R.J. Ott *et al.*. 1971. Phys.Rev. D3:52-56,1971.

[53] V. L. Fitch *et al.* Phys. Rev. 140, B1088 - B1091 1965

[54] V.P. Koptev *et al.* 1995. JETP Lett.62:877-881,1995, Pisma Zh.Eksp.Teor.Fiz.61:865-868,1995.

[55] F. Ambrosino et al. “The tracking detector of the KLOE experiment”, Nucl. Inst. Meth. A 488, 1-23 2002.

[56] M. Adinolfi et al. “The KLOE electromagnetic calorimeter”, Nucl. Inst. Meth. A **482** (2002) 363-385.

[57] S. Eidelman *et al.* [Particle Data Group Collaboration], Phys. Lett. B **592** (2004) 1.

[58] S. Bertolucci *et al.*, KLOE *note* (62) (1993).

[59] A. Aloisio et al. “The KLOE Data Acquisition system, addendum to the KLOE technical proposal”, LNF-95/014(IR) (1995).

[60] R. Brun et al. GEANT3, CERN-DD/EE/84-1 (1984).

[61] R. Brun et al. GEANT: Simulation for particle physics experiments, user guide and reference manual, CERN-DD-78-2-REV (1978).

[62] C. M. Carloni Calame et al. The BABAYAGA event generator, hep-ph/0312014 (2003).

[63] W. Kim *et al.*, KLOE *memo* (6) (1996).

[64] A. Antonelli *et al.*, KLOE *note* (157) (1996).

[65] M. Incagli *et al.*, KLOE *memo* (147) (1996).

[66] K. W. Edwards *et al.*, Nucl. Instrum. Meth. A **252** (1986) 384.

[67] P. De Simone *et al.*, Ph.D. Thesis, Universitá degli studi di Roma “La Sapienza”,(1994).

[68] V. S. Demidov, V. A. Dobrokhotov, E. A. Lyublev and A. N. Nikitenko, Sov. J. Nucl. Phys. **52** (1990) 1006 [Yad. Fiz. **52** (1990) 1595].

[69] F. Ambrosino *et al.* [KLOE Collaboration], Nucl. Instrum. Meth. A **534** (2004) 403.

[70] M. Adinolfi *et al.* [KLOE Collaboration], Nucl. Instrum. Meth. A **492** (2002) 134.

[71] F. Ambrosino, E. De Lucia, P. de Simone, P. Massarotti and V. Patera *Measurement of the reconstruction efficiency of the charged kaon decays.*, KLOE Memo **320** (2005).